Characterisation of a Laser Wakefield Accelerator with Ultra-Short Probe Pulses

Dissertation

zur Erlangung des akademischen Grades
doctor rerum naturalium (Dr. rer. nat.)

vorgelegt dem Rat der Physikalisch-Astronomischen Fakultät der
Friedrich-Schiller-Universität Jena

eingereicht von Dipl.-Phys. Maria Reuter
geboren am 17. Dezember 1985 in Jena

Gutachter:

1. **Prof. Dr. Malte C. Kaluza**
   Institut für Optik und Quantenelektronik Jena
   Friedrich-Schiller-Universität Jena, Deutschland

2. **Prof. Dr. Stefan Karsch**
   Fakultät für Physik Ludwigs-Maximilians-Universität München &
   Max-Planck-Institut für Quantenoptik, Deutschland

3. **Prof. Dr. Georg Pretzler**
   Institut für Laser- und Plasmaphysik
   Heinrich-Heine-Universität Düsseldorf

Tag der öffentlichen Verteidigung:
20.09.2018

Zusammenfassung

Im Rahmen dieser Arbeit wurden Aspekte der Elektronenbeschleunigung mithilfe eines Hochintensitätslasers in einem unterdichten Plasma untersucht. Der zugrundeliegende Beschleunigungsmechanismus bei dem durch den Laserpuls eine Plasmawelle erzeugt wird, die zusammen mit dem Laserpuls durch das Medium propagiert, nennt sich Laser Wakefield Acceleration. Aufgrund der gemeinsamen Propagation des Laserpuses und der Plasmawelle bewegt sich das longitudinale alternierende elektrische Feld der Plasmawelle mit nahezu Lichtgeschwindigkeit, sodass Elektronen, die im Feld dieser Plasmawelle eingefangen werden, auf relativistische Energien beschleunigt werden können. Während grundlegende Prinzipen, wie die Entstehung der Plasmawelle, die Injektion von Elektronen in die beschleunigende Phase der Welle und Grenzen des Beschleunigungsprozesses bereits bekannt sind, ist der genaue Ablauf der nichtlinearen Wechselwirkungsprozesse zwischen Laserpuls und Plasmawelle noch nicht ausreichend erforscht. Die nichtlineare Wechselwirkung hat zur Folge, dass kleinste Änderungen der Anfangsbedingungen zu starken Schwankungen der Elektronenpulsparameter führen können, die sich beispielsweise in Form von Unterschieden in beschleunigter Ladung, der Endenergie oder in Richtungsschwankugnen auswirken. Eine zentrale Rolle spielt dabei die Position im Plasma, an der Elektronen in die Plasmawelle injiziert werden, da diese Position die maximale Energie der Elektronen maßgeblich beeinflusst. Die Injektion der Elektronen in die Plasmawelle an einer definierten Position ist daher eine Möglichkeit Schuss-zu-Schuss-Schwankungen zu reduzieren und die Verwendung der beschleunigten Elektronenpulse, z.B. als stabile Sekundärstrahlungsquelle für zeitlich und räumlich hochauflösende Bildgebungsverfahren, zu ermöglichen. Durch die Untersuchung einer Methode zur kontrollierten Injektion an einem Elektronendichtesprung konnte ein Zusammenhang zwischen den Eigenschaften des Dichtesprungs zu verschiedenen Elektronenpulsparametern wie Elektronenenergie und beschleunigter Ladung rekonstruiert werden, was eine anwendungsspezifische Abstimmung der Elektronenpulse durch eine gezielte Formung des Dichtesprungs in Aussicht stellt. Nichtsdestotrotz konnten Schuss-zu-Schuss-Schwankungen in den Elektronenparametern nicht vollständig beseitigt werden und sind vermutlich auf die nichtlineare Evolution des Laserpusles im Plasma zurückzuführen. Für die Stabilisierung der Wechselwirkungsprozesse sind Kenntnisse über deren Abläufe zwingend notwendig, was eine Methode zur Beobachtung der Plasmawelle und des Laserpusles erfordert. Mithilfe eines ultrakurzen Probepulses in Kombination mit einem hochauflösenden Abbildungssystem, welche am Institut für Optik und Quantenelektronik in Jena entwickelt wurden, können die in räumlichen und zeitlichen Skalen von Mikrometern und Femtose-

kunden stattfindenenden Prozesse genauer untersucht werden. Mit diesem System konnten Charakteristika der untrennbar mit dem Beschleunigungsprozess verbundenen Magnetfelder in noch nie dagewesenem Detail untersucht werden. Die damit einhergehenden tieferen Einblicke ermöglichten eine erstmalige Beobachtung von Signaturen des Magentfelds des treibenden Laserpulses und ebnen damit den Weg zu einer indirekten Beobachtung der Entwicklung des Laserpulses während der Wechselwirkung.

Abstract

Within the frame of this thesis, aspects of the acceleration of electrons with high-intensity laser pulses inside an underdense plasma were investigated. The basic acceleration mechanism, which is referred to as laser wakefield acceleration relies on the generation of a plasma wave by an intense laser pulse. Since the plasma wave co-propagates with the laser pulse, its longitudinally alternating electric field moves with a velocity close to the speed of light and electrons trapped in the accelerating phase of the wave can be accelerated to relativistic energies. While basic principles such as the generation of a plasma wave, the injection of electrons into the accelerating phase of the wave and limits to the acceleration process are known, the exact processes occurring during the nonlinear interaction of laser pulse and plasma wave still need to be explored in more detail. The consequence of those nonlinear processes is a drastic change of the electron parameters – e.g. final electron energy, bandwidth and pointing – through slight changes in the initial conditions. In this context, the position in the plasma at which electrons are injected into the plasma wave plays a key role for the maximum achievable electron energy. Therefore, the injection of electrons at a defined position is a possibility to reduce shot-to-shot fluctuations and might make the electron pulses applicable, e.g. as a stable source of secondary radiation for temporally and spatially highly resolving imaging techniques. The investigation of controlled injection of electrons at an electron density transition demonstrated a correlation of electron pulse parameters such as electron energy gain and accelerated charge to the properties of the transition, and thus, might be a promising method to generate custom designed electron pulses. Nevertheless, shot-to-shot fluctuations in the electron parameters were still observed and are most likely caused by the nonlinear evolution of the laser pulse inside the plasma. To further reduce instabilities, deeper insight into these nonlinear processes is required and hence, a method to observe the plasma wave and the laser pulse. Combining an ultra short probe pulse with a highly resolving imaging system as successfully implemented at the institute of Optics and Quantumelectronics in Jena, more light can be shed on these processes, which take place on femtosecond and micrometer scales. With that system, characteristics of the magnetic fields inextricably connected to the acceleration process could be studied in unprecedented detail. This deeper insight allowed to observe signatures of the magnetic field of the driving laser pulse for the first time, which paves the way for the indirect observation of the main laser pulse during the interaction.

Contents

1. Introduction

Within the last century, particle radiation became a main pillar of modern science and research. The importance of particle radiation became obvious at the latest when Ernest Rutherford developed his atomic theory based on results obtained from the scattering of α-particles inside a gold foil [1]. Digging deeper into the structure of matter requires particle beams with higher energies, which became available due to the development of radio-frequency (rf) accelerators [2]. With such highly energetic particle beams, the standard model of particle physics could be investigated, which includes the experimental discovery of quarks at SLAC in Stanford by the scattering of 7...17 giga-electronvolt (GeV) electrons at protons in the late 1960s [3,4] and more recently, the discovery of the Higgs Boson at CERN by colliding two proton beams with particle energies of ≈ 4 tera-electronvolt (TeV) [5].

Rf accelerators employ alternating electric fields to accelerate charged particles in a circular or linear geometry. Since the maximum achievable electric field of this kind of accelerators is limited to $\mathcal{E} \approx 10...100\,\mathrm{MV/m}$ by material break down of the accelerator cavity, higher particle energies can only be gained when the length of the accelerator is increased, which is connected to higher costs. The world wide largest circular accelerator is the Large Hadron Collider (LHC) with a circumference of 27 km [6] providing 13 TeV protons for collision experiments [7] and the longest linear accelerator with a length of 3 km is situated at the Stanford Linear Accelerator Center (SLAC). While still in operation, electron and positron beams could be accelerated to kinetic energies of 50 GeV.

An alternative accelerator concept is based on the acceleration of charged particles in plasma, which can provide strong electric fields due to local charge separations on micrometer (μm) scales. In 1979, laser wakefield acceleration (LWFA) was proposed [8], which involves a charge separation propagating with a velocity close to the speed of light c, in which charged particles can be accelerated over distances longer than the extent of the quasistatic accelerating field itself. This propagating charge separation is referred to as plasma wave or wakefield, which in longitudinal direction manifests itself as a periodic electron density distribution with a periodically alternating electric field with a wavelength $\lambda_p \propto 1/\sqrt{n_e}$ where n_e is the electron density of the ambient plasma. In this acceleration scheme, the plasma wave is generated by an intense laser pulse, which expels electrons from its regions of highest intensity. Due to the generated charge separation, the electrons return to their origin and start to oscillate with the plasma frequency $\omega_p \propto \sqrt{n_e}$ and with a fixed phase relation given by the correlated excitement by the driving laser pulse. Since the phase of

the plasma wave propagates with the group velocity of the laser pulse, electrons can be accelerated inside one plasma wave period over centimetre (cm) distances without leaving the accelerating structure, which has a longitudinal extent of $\lambda_p = 2\pi c/\omega_p$. Note that the plasma wave is most efficiently generated when the longitudinal extent of laser pulse given by its pulse duration τ_L fits into one half-cycle of the plasma wave period, i.e., $\tau_L \lesssim \lambda_p/(2c)$. In this case, the laser pulse is fully embedded in the plasma wave's electron density peaks leading to quasi-resonant excitement. As a rule of thumb, the maximum electric field provided by a plasma wave can be estimated with $\mathcal{E}_0\,[\mathrm{GV/m}] = 9.6 \times 10^{-8}\sqrt{n_e[\mathrm{cm}^{-3}]}$ [9, 10]. With $n_e = 5 \times 10^{18}\,\mathrm{cm}^{-3}$, fields on the order of 200 GV/m can be generated, which is three orders of magnitude larger than those fields provided by rf accelerators.

Since in the 1980s the requirements for this acceleration concept could not be met by state of the art lasers, an alternative scheme where the plasma wave is driven by a highly energetic electron bunch was suggested in 1985 [11] and in 1988, the acceleration of electrons to relativistic energies – that is kinetic energies larger than the electrons rest energy $E = m_e c^2$ – was demonstrated [12]. However, this acceleration scheme still relies on rf accelerated driver bunches and thus, no improvement in size or cost of the accelerator was yet achieved.

With the development of chirped pulse amplification (CPA) in 1985 [13] higher laser powers became available leading to the first LWFA experiments in the self-modulated regime [14–17] where a laser pulse with pulse durations in the picosecond (ps) regime $\tau_L > \lambda_p/(2c)$ is modulated in the generated plasma wave. However, in this long pulse regime usually broadband electron spectra are generated. In 2002, the nonlinear broken wave regime [18], was investigated theoretically. Here, a highly intense ($I \gg 10^{18}\,\mathrm{W/cm}^2$), resonant laser pulse generates quasi monoenergetic electron bunches. Though not exactly matching the theoretically required laser parameters, quasi monoegergetic electron bunches with kinetic energies between ≈70 MeV and ≈170 MeV were demonstrated independently by three groups in 2004 [19–21]. In the following years, the energy of quasi monoegergetic electron bunches could be boosted into the GeV-regime [22–24]. Moreover, with the injection of accelerated electrons into a second independent but synchronised LWFA stage [25] significantly higher electron energies might be achieved in the near future. Through the acceleration in independent stages, the decrease of laser intensity through natural diffraction and the transfer of laser energy to the plasma can be compensated. In the process of laser wakefield acceleration, coherent secondary electromagnetic radiation can be emitted. While the wavelength of this radiation depends on the energy of the emitting electrons [26, 27], coherence is given when the electron bunch duration is shorter than the emitted wavelength [28]. Simultaneously, the pulse duration of the electron bunch determines the pulse duration of the emitted radiation. As electron pulses as short as a few femtoseconds (fs)

can be generated by LWFA [29, 30], this radiation can potentially be used for high resolution imaging, which is relevant in many disciplines of science such as physics, biology, chemistry and medicine. A development towards application was advanced by e.g. [31, 32], where the application of Betatron radiation for medial imaging was investigated. The reduced size and costs of a high-power laser system with respect to the rf accelerators makes particle accelerators available for research in universities and possible future applications in hospitals.

Nevertheless, the applicability of electron beams generated by LWFA requires stability and controllability of the electron bunch parameters. A possibility to improve the controllability of the acceleration process is controlled injection of electrons into the accelerating phase of the plasma wave. Several injection schemes including ionisation injection [33–37], colliding pulse injection [38–40], density downramp injection [41–43] and density transition injection[1] [44–49] have been investigated already. In the first successful experiments employing density transition injection, tunable quasi monoenergetic electron bunches were generated [47, 48]. Nevertheless, electron energies as high as demonstrated in the self injected regime are not within reach yet. Within the frame of this thesis, controlled injection at an electron density transition is investigated using a variety of diagnostics, which help to understand the injection and subsequent acceleration process. The results obtained might be applied to stabilise the electron pulse parameters and thus, pave the way to generate electron pulses with reproducible parameters in the GeV regime in a controlled manner.

To further reduce instabilities in laser wakefield accelerators, the evolution of the laser pulse and the plasma wave has to be understood in detail. The direct observation of the processes is challenging due to the small temporal and spatial scales of the order of fs and μm, respectively. Nevertheless, optical probing with a synchronised probe beam is a powerful tool to look inside the accelerating structure [29, 50–52]. Here, a fraction of the main laser pulse is used to back-light the interaction; usually in a transverse (probe beam beam propagates under 90° with respect to the main beam) or longitudinal (probe beam co-propagates with the main beam) geometry.

In a longitudinal geometry, a reference and a probe pulse are imaged onto a spectrometer where the detected spectral interference pattern is determined by the relative phase of the two pulses. With one pulse trailing (probe) and one pulse preceding (reference) the main pulse, the phase difference is introduced by the density modulation of the plasma wave, which by varying the delay of the trailing probe pulse could be deduced at different positions behind the main pulse [53, 54]. In a similar setup but with a chirped trailing pulse, the structure of the plasma wave could be visualised in a single shot through Fourier domain

[1] Also referred to as shockfront injection.

holography [50]. Nevertheless, due to the intrinsic time integration of this method – caused by the co-propagation of main and probe pulse leading to a temporal average over the whole interaction time – temporally resolved data of the interaction cannot be detected, i.e., the evolution of the plasma wave cannot be investigated.

With the introduction of an angle $> 0°$ between the probe and the pump pulse's directions of propagation, temporal resolution can be achieved with a sufficiently short probe pulse [55] and can be optimised by probing under 90° with respect to the direction of propagation of the main pulse. The first temporally resolved snapshots of the plasma wave were detected in this geometry with a probe pulse of 8.5 fs duration [29]. Simultaneously, polarimetry measurements allowed for the deduction of the magnetic fields present during the acceleration processes. However, the relatively low laser power of ≈ 16 tera-watts (TW) in this experiment had to be compensated by an increased electron density to achieve optimum acceleration conditions, which in consequence decreases the plasma wavelength. Therefore, the temporal and spatial resolution were not sufficient to resolve sub-plasma wavelength features.

With the JETI-laser system of the Institute of Optics and Quantum Electronics in Jena delivering ≈ 30 TW laser pulses, the acceleration of electrons in lower electron densities and thus, plasma waves with longer wavelengths of the order of 10 μm is possible. Nevertheless, sub-plasma wavelength resolution requires a probe pulse duration of the order of $\tau_{probe} < \lambda_p/(2c)$ and is thus, still not possible with the original pulse duration of ≈ 30 fs. Therefore, an ultrashort probe beam was developed, which relies on spectral broadening and temporal compression of a fraction of the main pulse [51]. With these ultrashort pulses and a technique called shadowgraphy, new insight into the accelerating structure could be obtained [52]. Within the frame of this thesis, polarimetry measurements are combined with high-resolution shadowgraphy to investigate the evolution of the strong magnetic fields present in the process of laser wakefield acceleration in unprecedented detail. While so far, only the magnetic fields of the plasma wave and the accelerated electrons could be measured [29,56–58], in the present study, an influence of the strong magnetic fields of the laser pulse on the probe pulse's state of polarisation was observed, which is an important step towards the indirect observation of the evolution of the main laser pulse.

The present thesis is structured as follows:

Chapter 2 covers the theoretical background needed to understand the presented experiments and results. At the beginning, laser pulses are described mathematically, followed by the principles of laser matter interaction. Here, the interaction of a single electron as well as a plasma with electromagnetic waves is explained. Subsequently, laser wakefield acceleration – the subject of this thesis – is illuminated in detail including 1D and 3D mod-

els describing the limit on the electron energy gain. Moreover, topics investigated in the following chapters – controlled injection of electrons into the plasma wave, wavebreaking, Betatron oscillations and the influence of magnetic fields in a plasma on a probe pulse – are discussed at the end of the chapter.

In **Chapter 3**, the setup and data analysis are described. After a brief overview of the experimental setup, the JETI40-laser parameters and the gas targets are introduced. This is followed by a detailed description of the diagnostics and the corresponding data analysis methods.

In **Chapter 4**, the acceleration of electrons injected at a density transition is investigated. The beginning of the chapter covers the characteristics of the electron density profile around the transition. Subsequently, wavebreaking in the transition region is discussed. The influence of the injection method on the electron energy distributions as well as the transverse beam profile is described in great detail.

Chapter 5 is devoted to high resolution shadowgraphy in combination with polarimetry measurements. In this context, the change of polarisation of the probe pulse under the influence of both the azimuthal magnetic fields of the plasma wave and the accelerated electrons as well as the strong oscillating field of the pump laser pulse is studied.

Chapter 6 provides a brief summary and outlook.

2. Theory of Laser Wakefield Acceleration

In this chapter, the theory necessary to analyse and understand the experimental findings described in this thesis as well as the underlying physical processes are introduced. After a short mathematical description of laser pulses, aspects of their interaction with matter are explained leading to the concept of laser wakefield acceleration. This is followed by selected topics, which go beyond the acceleration process and are related to the following chapters. A short introduction to particle in cell (PIC) simulations, which are commonly used for the numerical description and investigation of laser particle acceleration completes this chapter.

2.1 Gaussian Laser Pulses

The intensity at the position of the focus of a laser pulse – a crucial parameter for the experiments discussed in later sections – can be expressed in terms of the laser's energy, pulse duration and beam radius, which can be determined experimentally.

As a fundament of electromagnetism, the Maxwell equations (Eq. (2.1)) [1] describe the dynamics of electric $\vec{\mathcal{E}}$ and magnetic $\vec{\mathcal{B}}$ fields as well as their interaction with charged particles [59, 60]

$$\begin{aligned} \vec{\nabla}\cdot\vec{\mathcal{E}} &= \tfrac{\rho}{\epsilon_0} & \qquad \vec{\nabla}\cdot\vec{\mathcal{B}} &= 0 \\ \vec{\nabla}\times\vec{\mathcal{E}} &= -\tfrac{\partial\vec{\mathcal{B}}}{\partial t} & \qquad \vec{\nabla}\times\vec{\mathcal{B}} &= \tfrac{1}{c^2}\tfrac{\partial\vec{\mathcal{E}}}{\partial t} + \mu_0\vec{j}. \end{aligned} \tag{2.1}$$

The constants ϵ_0 and μ_0 are the vacuum permittivity and permeability respectively, which are related to each other via the vacuum speed of light $\epsilon_0\mu_0c^2 = 1$. The current density $\vec{j}$ and the charge density ρ vanish in vacuum. Introducing the vector potential $\vec{\mathcal{A}}$ and the scalar electric potential ϕ, the electric and the magnetic fields can be expressed as

$$\begin{aligned} \vec{\mathcal{E}} &= -\frac{\partial\vec{\mathcal{A}}}{\partial t} - \vec{\nabla}\phi, \\ \vec{\mathcal{B}} &= \vec{\nabla}\times\vec{\mathcal{A}}. \end{aligned} \tag{2.2}$$

One possible solution of the Maxwell equations in vacuum is a linearly polarised plane wave (Eq. (2.3)), which – without loss of generality – propagates along x. The corresponding

[1] Note, that $\vec{\nabla}\times$ denotes the curl and $\vec{\nabla}\cdot$ the divergence of a vector field while $\vec{\nabla}$ represents the gradient of a scalar field.

electric and magnetic fields read

$$\begin{aligned}\vec{\mathcal{E}}(x,t) &= \mathcal{E}_{max}\sin(\Phi(x,t))\vec{e}_y,\\ \vec{\mathcal{B}}(x,t) &= \mathcal{B}_{max}\sin(\Phi(x,t))\vec{e}_z,\end{aligned} \tag{2.3}$$

where $\mathcal{E}_{max}$ and $\mathcal{B}_{max}$ are the amplitudes of the electric and the magnetic fields, respectively, which in vacuum are coupled through $\mathcal{B}_{max} = \frac{\mathcal{E}_{max}}{c}$. The phase is given by $\Phi(x,t) = \omega_L t - |\vec{k}_L|x + \Phi_0$ where the carrier frequency ω_L and wave vector $\vec{k}_L$ are related to the wave's wavelength as $\lambda_L = \frac{2\pi c}{\omega_L} = \frac{2\pi}{|\vec{k}_L|}$ and Φ_0 is a constant phase shift. A single plane wave infinitely extends in all directions.

Waist and Rayleigh length. In contrast to plane waves, the energy of a Gaussian beam is confined in transverse direction (cf. Fig. 2.1(a)). A Gaussian beam propagating in x-direction has its strongest $\vec{\mathcal{E}}$- and $\vec{\mathcal{B}}$-fields on the axis of symmetry, i.e., $y = z = 0$ and a 1/e beam radius given by

$$w(x) = w_0\sqrt{1 + \frac{x^2}{x_R^2}} \tag{2.4}$$

where $w_0 = w(0)$ is the beam radius in the focus, which is referred to as waist and

$$x_R = \frac{\pi w_0^2}{\lambda_L}, \tag{2.5}$$

is the Rayleigh length representing the distance from the waist at which the intensity of the laser pulse is halved, which is equivalent to $w(\pm x_R) = \sqrt{2}w_0$.

Pulse duration. Besides the confinement in transverse direction, a laser pulse additionally exhibits a temporal envelope. Therefore, a Gaussian shape with the 1/e pulse duration τ_0 is assumed. Strictly speaking, a Gaussian beam with a Gaussian temporal envelope is not an exact solution of the Maxwell equations anymore. However, it is a good approximation if $\tau_0 \gg \frac{1}{\omega_L}$ and becomes exact in the limit $\tau_0 \to \infty$. In the paraxial approximation, which holds for small diffraction angles $\theta_{diff} \approx \frac{w_0}{x_R} \ll 1$, the electric and magnetic fields of a Gaussian laser pulse can be expressed as [61, 62]

$$\begin{aligned}\vec{\mathcal{E}}(x,y,z,t) &= \overbrace{\mathcal{E}_{max}\frac{w_0}{w(x)}\mathrm{e}^{-(\frac{t-x/c}{\tau_0/2})^2}\mathrm{e}^{-\frac{y^2+z^2}{w(x)^2}}}^{\mathcal{E}_0}\sin\left(\Phi(x,t) - \frac{|\vec{k_L}|(y^2+z^2)}{2R(x)} + \Xi(x)\right)\vec{e}_y,\\ \vec{\mathcal{B}}(x,y,z,t) &= \underbrace{\mathcal{B}_{max}\frac{w_0}{w(x)}\mathrm{e}^{-(\frac{t-x/c}{\tau_0/2})^2}\mathrm{e}^{-\frac{y^2+z^2}{w(x)^2}}}_{\mathcal{B}_0}\sin\left(\Phi(x,t) - \frac{|\vec{k_L}|(y^2+z^2)}{2R(x)} + \Xi(x)\right)\vec{e}_z,\end{aligned} \tag{2.6}$$

where $\mathcal{E}_0$ and $\mathcal{B}_0$ are the envelopes of the electric and magnetic fields, respectively. The

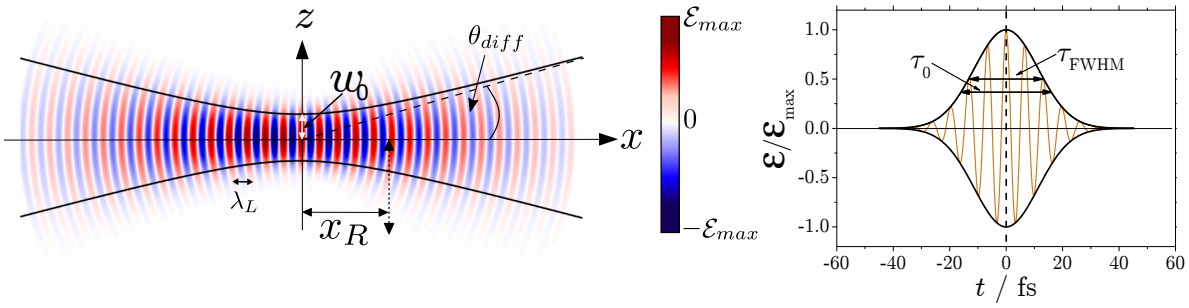

(a) (b)

Figure 2.1 *Laser pulse with a Gaussian temporal envelope represented by its electric field. (a) Two-dimensional profile of a Gaussian laser pulse propagating in x-direction. The direction of polarisation is $\vec{e}_y$. (b) One-dimensional field profile (orange line) and field envelope (black line). The FWHM and the 1/e pulse duration are illustrated as double arrows.*

terms $R(x) = x\big(1 + (\frac{x_R}{x})^2\big)$ and $\Xi = \arctan(\frac{x}{x_R})$ describe the curvature of the wave fronts and the Gouy phase.

Spectrum. As a consequence of the finite pulse duration, the laser pulse exhibits a finite spectral bandwidth in frequency space. Fourier transforming the time dependent terms of Eq. (2.6) using the longitudinal coordinate $\tilde{t} = t - x/c$ gives

$$\int_{-\infty}^{\infty} \mathrm{d}\tilde{t}\, \mathrm{e}^{-(\frac{\tilde{t}}{\tau_0/2})^2} \sin(\omega_L \tilde{t} + \Phi_0) \mathrm{e}^{-i\omega\tilde{t}} = \frac{i\sqrt{\pi}}{4}\, \tau_0\, \mathrm{e}^{-i\,\Phi_0} \left(\mathrm{e}^{-\frac{1}{16}(\tau_0^2(\omega+\omega_L)^2} - \mathrm{e}^{-\frac{1}{16}\tau_0^2(\omega-\omega_L)^2}\right). \quad (2.7)$$

The term $\mathrm{e}^{-\frac{1}{16}(\tau_0^2(\omega+\omega_L)^2)}$ is neglected for the following discussion as only positive frequencies have a physical relevance. With $(\omega - \omega_L) = \Delta\omega_L$, the spectral bandwidth can be extracted from the exponent. From $\mathrm{e}^{-\frac{1}{16}\tau_0^2\Delta\omega^2} \stackrel{!}{=} \frac{1}{e}$ follows the time-bandwidth product $\tau_0\Delta\omega_L = 4$ for 1/e parameters and accordingly, $\tau_{FWHM}\Delta\omega_L = 4\ln 2$ for full width half maximum (FWHM) parameters. The 1/e and the FWHM pulse durations are illustrated in Fig. 2.1(b).

Intensity. The laser intensity is given by the absolute of the temporally averaged Pointing vector $\vec{S} = \frac{1}{\mu_0}\vec{\mathcal{E}}\times\vec{\mathcal{B}}$ and can be expressed in terms of the electric field (Eq. (2.6)) [59]

$$I_L(x,y,z,t) = \epsilon_0 c \langle|\vec{\mathcal{E}}(x,y,z,t)|^2\rangle_T \stackrel{SVEA}{=} \frac{1}{2}\epsilon_0 c \mathcal{E}_0^2, \quad (2.8)$$

with $\langle\ \rangle_T$ denoting averaging over one laser period. The term on the right-hand side is valid in the slowly varying envelope approximation (SVEA), which assumes that the evolution of the laser pulse's envelope is significantly slower than the oscillation of the phase of the field. Experimentally, the laser energy, pulse duration and beam radius are more readily accessible than the electric and magnetic fields of the laser pulse. In terms of these quantities, the

peak intensity in vacuum I_V can be calculated with

$$I_V \left[\frac{\mathrm{W}}{\mathrm{cm}^2}\right] = 2 \times 10^{23} \left(\frac{\ln(2)}{\pi}\right)^{\frac{3}{2}} \frac{E_L[\mathrm{J}]}{r_L^2[\mu\mathrm{m}]\tau_L[\mathrm{fs}]}, \tag{2.9}$$

where E_L is the total laser energy, τ_L the FWHM pulse duration and r_L the FWHM beam radius of the laser pulse's intensity profile, which at the position of the the focus of the laser pulse can be described as

$$I_L(x, y, z, t) = I_V \, \mathrm{e}^{-2(\frac{t-x/c}{\tau_0/2})^2} \mathrm{e}^{-2\frac{y^2+z^2}{w_0^2}}, \tag{2.10}$$

where $\tau_0 = 2\sqrt{2\ln(2)}\tau_L$ and $w_0 = \sqrt{2\ln(2)}r_L$ are the 1/e pulse duration and beam radius of the laser's electric field expressed in terms of the FHWM pulse duration and beam radius regarding the laser's intensity envelope.

With state of the art laser systems, laser intensities in the range of $10^{22}\frac{\mathrm{W}}{\mathrm{cm}^2}$ are feasible [63]. Note that the calculation of the vacuum peak intensity using Eq. (2.9) assumes perfect Gaussian pulses in space and time and is therefore, only an estimate. The intensity of real pulses is usually lower for various reasons; phase distortions acquired in the amplification process can influence the quality of the focal spot as well as the temporal pulse shape. In consequence, the energy within the FHMW pulse duration and spot size is reduced. A measure for the quality of the focal spot is the q-factor $q_L = \frac{E_{FHWM}}{E_L}$, where E_{FWHM} is the laser energy contained within the FWHM focal spot area. For an ideal Gaussian pulse $q_L \approx 0.58$. Note that q_L does not evaluate the temporal profile of the laser pulse.

2.2 Principles of Laser Matter Interaction

In this section, the movement of a single electron in electromagnetic fields is described followed by the more complex topic of the interaction of underdense plasmas with laser pulses.

2.2.1 Interaction of Single Electrons with Electromagnetic Waves

In the relativistic regime, the magnetic field of an electromagnetic wave causes electrons oscillating in the wave's electric field to drift in the direction of propagation of the wave. Moreover, electrons oscillating in the electric field of a focused laser pulse are pushed away from regions of high intensities by the ponderomotive force.

The equation of motion of an electron in an electromagnetic field, is given by

$$m_e \frac{\mathrm{d}}{\mathrm{d}t} \gamma \vec{v}_e = -e \left(\vec{\mathcal{E}} + \vec{v}_e \times \vec{\mathcal{B}}\right), \tag{2.11}$$

where $\gamma = 1/(\sqrt{1 - v_e^2/c^2})$ is the Lorentz factor, m_e is the electron rest mass, e the el-

ementary charge and $\vec{v}_e$ the electron velocity with its absolute v_e. Let us first consider an electron's motion in a **plane wave**. In the non-relativistic regime ($\gamma \approx 1$, $v_e \ll c$), contributions of the magnetic field can be neglected since $\mathcal{B}_{max} = \frac{\mathcal{E}_{max}}{c}$, i.e., the electron harmonically oscillates in the electric field with a maximum velocity $v_{e,max} = \frac{e\mathcal{E}_{max}}{\omega_L m_e}$. As a measure of the electric field amplitude, it is convenient to define the **normalised vector potential**

$$a_0 = \frac{e\mathcal{E}_{max}}{\omega_L m_e c}, \tag{2.12}$$

which expressed in terms of intensity and wavelength reads

$$a_0 = \sqrt{\frac{I_L\ [W/cm^2]}{1.37 \times 10^{18}}} \lambda_L\ [\mu m]\,. \tag{2.13}$$

In the relativistic limit where $\gamma > 1$, $a_0 \gtrsim 1$ and $v_{e,max} = \frac{e\mathcal{E}_{max}}{\omega_L \gamma m_e} \to c$, the contribution of the magnetic field to the electron's motion cannot be neglected anymore. With the initial conditions $x(\tilde{t} = 0) = y(\tilde{t} = 0) = 0$ as well as $v_x(\tilde{t} = 0) = \frac{v_{e,max}^2}{2c}$ and $v_y(\tilde{t} = 0) = v_{e,max}$, where $\tilde{t} = t - x/c$, the solution of Eq. (2.11) is given by [64]

$$x_e = a_0^2 \frac{c}{4\omega_L}\Big(\frac{1}{2}\sin(2\omega_L \tilde{t}) + \omega_L \tilde{t}\Big) \qquad || \ (\vec{v}_{e,y} \times \vec{\mathcal{B}}),\ \propto a_0^2, \tag{2.14}$$

$$y_e = a_0 \frac{c}{\omega_L}\ \sin(\omega_L \tilde{t}) \qquad ||\vec{\mathcal{E}},\ \propto a_0, \tag{2.15}$$

$$z_e = 0. \tag{2.16}$$

In y-direction, the electron still oscillates in the electric field of the wave with a frequency ω_L. Due to the influence of the magnetic field, the oscillation in y-direction is superimposed with a motion in propagation direction $\vec{e}_x$ of the electromagnetic wave. Note that the amplitude of the oscillation in y-direction grows linearly with a_0 whereas the amplitude of the movement in x-direction is proportional to a_0^2. The motion in x-direction can be decomposed in a constant drift velocity $v_d = c\frac{a_0^2}{a_0^2+4}$ and an oscillation with the frequency $2\omega_L$. Fig. 2.2(a) illustrates the electrons trajectory in the $x-y$-plane. In the electron's frame of reference co-moving with v_d, the motion appears as a figure-of-8 (Fig. 2.2(b)), which clearly visualises the oscillations with ω_L in y- and with $2\omega_L$ in x-direction. Note that a transformation to a co-moving frame of reference with a given velocity does not affect distances or time spans and is therefore, not a Lorentz transformation.

Eqs. (2.14)-(2.16) are valid if an electron experiences the electromagnetic field of a single plane wave, which infinitely extends in all directions but they can still be used in a more realistic scenario employing a focused laser beam in the slowly varying envelope approximation. In the intensity gradients due to the finite spot size of a **focused laser beam** an additional force is exerted on the electron. An electron at rest placed on the laser axis

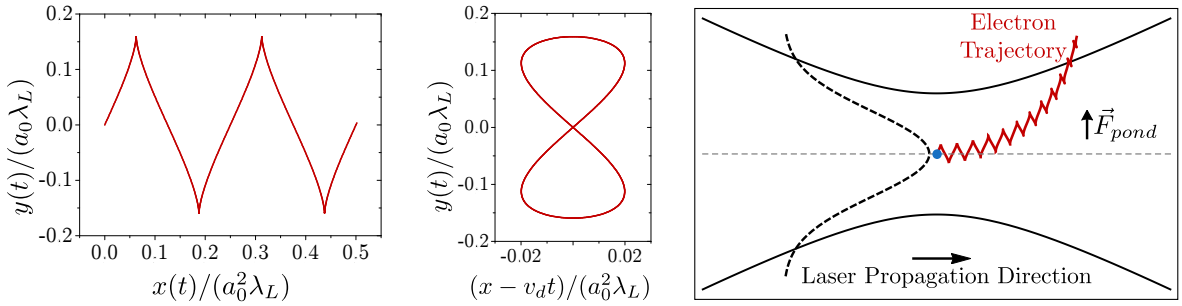

Figure 2.2 *Relativistic motion of an electron. In a plane wave in (a) the laboratory system and (b) the co-moving frame of reference. (c) In a focused laser beam in the laboratory system.*

and hence, on the axis of highest intensities starts to oscillate and drift in the laser field (Eqs. (2.14), (2.15)). The oscillation in y-direction drives the electron into regions of lower intensities where the restoring $\vec{\mathcal{E}}$-field is smaller than on axis. As a consequence, the centre of the oscillation of the electron is continuously shifted towards regions of lower intensities. The superposition of the electron's motion in the electromagnetic fields discussed above with the transverse walk-off due to the intensity gradients results in a trajectory as shown in Fig. 2.2(c). The associated **ponderomotive force**

$$\vec{F}_{pond} = -\frac{e^2}{4\langle\gamma\rangle_T m_e \omega_L^2}\vec{\nabla}\langle|\vec{\mathcal{E}}(x,y,z,t)|^2\rangle_T \propto \vec{\nabla} I(x,y,z,t), \tag{2.17}$$

can be derived by time averaging the equation of motion (Eq. (2.11)) over one laser period including second-order terms, which account for the spatial inhomogeneity due to the laser beam's transverse intensity profile.

2.2.2 Interaction of Underdense Plasmas with Electromagnetic Waves

"A plasma is a quasi neutral [ensemble] of charged and neutral particles, which [is subject to collective] behaviour [due to its long-range electromagnetic forces]." [65] It can be generated from fluids and solids by high-intensity lasers. While electromagnetic radiation is reflected and absorbed by overdense plasmas, it can propagate through underdense plasmas, which will be relevant in this thesis.

Definition of plasma. In this section, which is adopted from [65,66], the terms collective behavior and quasineutrality are explained by means of three criteria (cf. items 1. - 3. below).

1. While the interaction between the particles of a neutral gas is dominated by collisions, i.e., interactions between direct neighbours, the distribution and movement of charged particles induces electric and magnetic fields, which influence the motion of other charged particles

at much greater distances. This effect is referred to as collective behaviour and dominates the motion of the particles if the rate ω_{coll} at which collisions between the particles occur is smaller than the plasma frequency

$$\omega_p = \sqrt{\frac{nq^2}{\epsilon_0 m}}, \tag{2.18}$$

where n is the plasma's particle density, q is the plasma particle's charge and m is the mass of the plasma particles. Since the charge to mass ratio of ions is at least a factor of 1836 smaller than the charge to mass ratio of an electron, the response time of an ion is a factor of at least $\sqrt{1836}$ larger. Therefore, on fs-time scales, which will be relevant in the following chapters, the ion motion can be neglected when compared to the electrons, i.e., n is given by the electron density n_e, $q \to -e$ and $m \to m_e$.

2. Quasineutrality is achieved when the spatial dimensions L of a system are much larger than the Debye length $\lambda_D = \sqrt{\frac{\epsilon_0 k_B T_e}{n_e e^2}}$, where k_B is the Boltzmann constant and T_e the electrons' temperature. In a plasma, the electric potential of a charged particle is decreased by a factor[2] 1/e through the surrounding charges within a distance of λ_D.

3. Effective shielding requires the number of particles N_D inside the Debye-sphere with the radius λ_D to be substantially larger than one, i.e., $N_D = \frac{4}{3}\pi\lambda_D^3 n_{e0} \gg 1$.

Plasma generation. Electromagnetic radiation can ionise a material through the photoelectric effect if $E_{photon} \geq E_{ion}$, where E_{photon} is the energy of a single photon and E_{ion} the ionisation potential of the material. Nevertheless, lasers operating in the near infrared of the electromagnetic spectrum as employed in the experiments described in the following chapters exhibit photon energies in the range of 1 eV, which is significantly smaller than the ionisation energy of helium (cf. Table 2.1) – the target gas in the experiments. In the increased photon density of stronger electromagnetic fields, multi photon ionisation (MPI) becomes possible if $n\,\mathrm{E}_{photon} \geq E_{ion}$, which describes the simultaneous absorption of n photons. Both effects are illustrated in Fig. 2.3(a).

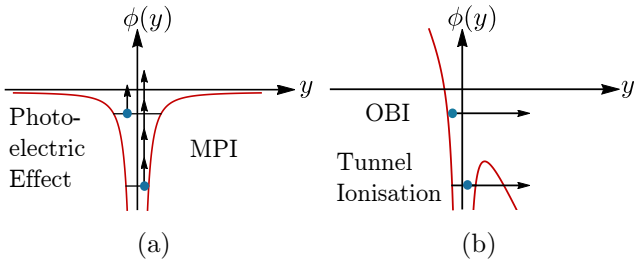

Figure 2.3 *Ionisation processes induced by electromagnetic radiation: (a) photoelectric effect and multi photon ionisation (MPI), (b) over the barrier (OBI) and tunnel ionisation.*

The superposition of the Coulomb and electric potential of the laser can be expressed

[2]Note the difference between the elementary charge e and Euler's number e.

as $\phi(y) = -\frac{1}{4\pi\epsilon_0}\frac{Ze^2}{|y|} - e\mathcal{E}y$ [67], where within the dimensions of the atom, the laser's electric field $\mathcal{E}$ can be regarded as uniform. For sufficiently strong fields, the Coulomb potential is deformed as shown in Fig. 2.3(b) and bound state electrons can tunnel through the barrier. Over the barrier ionisation (OBI) takes place if the laser intensity exceeds the threshold $I_{th}[\mathrm{W/cm^2}] \geq 4 \times 10^9 \left(\mathrm{E}^4_{\mathrm{ion}}\ [\mathrm{eV}]\right) \frac{1}{\mathrm{Z}^2_{\mathrm{eff}}}$ [67], where Z_{eff} is the ionisation state of the atom after ionisation. Since laser wakefield acceleration requires laser intensities of at least $\times 10^{18}\,\mathrm{W/cm^2}$, helium will be fully ionised by the leading edge of the laser pulse. Threshold intensities for hydrogen, helium and nitrogen [68], which will be needed for a discussion in section 2.3.3 are listed in Table 2.1.

Atom	E_{ion} / eV	Z_{eff}	I_{th} (OBI) / W/cm^2
Hydrogen	13.6	1	1.4×10^{14}
Helium	24.6	1	1.4×10^{15}
Helium^{2+}	54.4	2	8.8×10^{16}
Nitrogen^{4+}	77.5	4	9.0×10^{15}
Nitrogen^{7+}	667.0	7	1.6×10^{19}
Nitrogen^{8+}	1159.8 [33]	8	1.1×10^{20}

Table 2.1 *Ionisation energies E_{ion} and threshold intensities I_{th} for full ionisation of hydrogen, helium and nitrogen.*

Optical properties of a plasma in the nonrelativistic limit. The propagation of an electromagnetic wave in a plasma is determined by the plasma's dispersion relation $\omega_L^2 = c^2k_L^2 + \omega_p^2$. Phase and group velocity are therefore, given by [8]

$$v_{\Phi,L} = \partial\omega_L/\partial k_L = c\sqrt{1+\omega_p^2/(c^2k_L^2)} = c/\sqrt{1-\omega_p^2/\omega_L^2} \stackrel{!}{=} \frac{c}{\eta}, \tag{2.19}$$

and

$$v_{g,L} = \frac{\omega_L}{k_L} = c/\sqrt{1+\omega_p^2/(c^2k_L^2)} = c\sqrt{1-\omega_p^2/\omega_L^2} \stackrel{!}{=} \eta c, \tag{2.20}$$

where

$$\eta = \sqrt{1-\omega_p^2/\omega_L^2} = \sqrt{1-n_e/n_{cr}}, \tag{2.21}$$

is the index of refraction of the plasma. If $\omega_p \geq \omega_L$, Eq. (2.21) becomes imaginary implying that electromagnetic radiation cannot propagate inside the plasma but is absorbed and reflected. The critical density

$$n_{cr} = \frac{\omega_L^2\epsilon_0 m_e}{e^2}, \tag{2.22}$$

above which a laser pulse cannot propagate through the plasma anymore is determined by the frequency ω_L of the laser. For Ti:sapphire laser systems which are typically operated at a wavelength of $\approx 800\,\mathrm{nm}$, the critical density $n_{cr} \approx 1.73 \times 10^{21}\mathrm{cm}^{-3}$. Overdense plasma ($n_e > n_{cr}$) can be generated from solids ($n_e \approx 10^{23}\,\mathrm{cm}^{-3}$) while underdense ($n_e < n_{cr}$) and

near critical plasma ($n_e \approx n_{cr}$) can be generated from gases.

2.2.3 Nonlinear Laser Pulse Modulation in Underdense Plasmas

The mutual influence of laser pulse and plasma leads to a modulation of the laser pulse, which manifests in the spatial and temporal compression or decompression of laser energy. Inside a plasma wave, which will be introduced in more detail in later sections, usually, the energy of a sufficiently short laser pulse is compressed leading to the evolution of the laser pulse to higher intensities.

In this section, which is adopted from [69], laser pulse modulation in the relativistic regime where the plasma's index of refraction becomes intensity dependent will be explained. Assuming a relativistically underdense plasma, i.e., $\frac{1}{\gamma}\left(\frac{\omega_p}{\omega_L}\right)^2 \ll 1$, a weakly relativistic regime ($a_0 \approx 1$) and small perturbations of electron density $\delta n_e \ll n_e$ and laser frequency $\delta\omega_L \ll \omega_L$, the index of refraction can be linearly expanded and expressed as

$$\eta = 1 - \frac{\omega_p^2}{2\omega_L^2}\left(1 + \frac{\delta n_e}{n_e} - \frac{2\delta\omega_L}{\omega_L} - \frac{a^2}{4}\right). \tag{2.23}$$

Since group $v_{g,L}$ and phase velocity $v_{\Phi,L}$ are related to η, the perturbations δn_e and $\delta\omega_L$ as well as the laser's own intensity profile given by the profile of the normalised vector potential a influence the propagation and properties of the laser pulse.

Longitudinal gradients - temporal and spectral effects. Longitudinal gradients of η cause longitudinal variations in $v_{g,L}$ which leads to a longitudinal redistribution of laser energy. If the group velocity of a laser pulse continuously increases from its front to its back, the laser pulse is temporally compressed (cf. Fig. 2.4(a)) and vice versa it is stretched. Simultaneously, variations in $v_{\Phi,L}$ cause self-phase modulation, i.e., frequency up- and down-shifts. These two effects are related via Fourier transformation, and generally, do not occur isolated from each other.

Raman forward scattering. The sinusoidal density modulation δn_e of a low amplitude plasma wave (cf. section 2.3.1.1) with the wavelength λ_p generates a sinusoidal gradient of the index of refraction with the same wavelength leading to a modulation of the laser pulse's longitudinal intensity profile with the wavelength λ_p, i.e., a laser pulse with a longitudinal extent of $\tau_L v_{g,L} > \lambda_p$ is split into pulselets separated by λ_p. In frequency space, the bunching of laser energy inside one or more plasma wave periods is equivalent to the generation of frequency sidebands at $\omega_m = \omega_L \pm m\omega_p$ separated from the central frequency by integer multiples $m\omega_p$ of the plasma frequency.

Relativistic self phase modulation is caused by the relativistic mass increase of the electrons oscillating in the laser pulse's electric field. The rising intensity profile at the front of the pulse results in $\nabla\eta > 0$ while the falling intensity profile at the back causes $\nabla\eta < 0$. Therefore, the pulse's phase fronts at the front and the back of the pulse propagate faster

than those at its peak leading to a red-shift at the front and a blue-shift at the back of the pulse (cf. Fig. 2.4(b)). Simultaneously, **relativistic pulse steepening** can be observed in position space. Since the mass increase of the plasma wave's oscillating electrons is maximum at the peak of the laser pulse, the peak propagates faster than front and back which results in an asymmetric laser intensity profile, which is steepened at the front and flattened at the back.

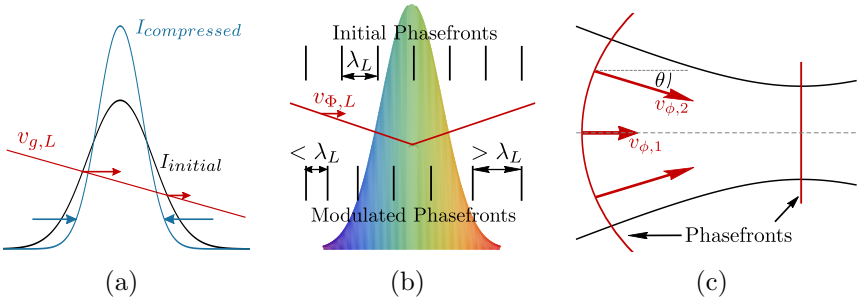

Figure 2.4 *(a) A decreasing group velocity $v_{g,L}$ along the propagation direction of the pulse leads to pulse compression. (b) Blue- (red-) shift of the laser wavelength λ_L occurs when the phase velocity $v_{\Phi,L}$ of the laser pulse decreases (increases) in the direction of propagation. (c) A laser beam is focused when the outer parts of the phase fronts propagate faster than the inner parts.*

Transverse gradients - focusing effects. If two parts of the same phase front travel with different phase velocities $v_{\Phi,1}$ and $v_{\Phi,2}$, the wavefront is bent. Since the energy of a light wave propagates normally to the phase fronts, this causes focusing and defocusing. If the outer parts of the phase front are bent towards the central axis in the direction of propagation of the wave as depicted in Fig. 2.4(c), the beam is focused and vice versa for a bending away from the axis.

Relativistic self-focusing is caused by the transverse intensity profile of the laser pulse with its peak on the laser axis. The relativistic mass increase of the oscillating electrons involves a change in the refractive index which reduces the phase velocity of the laser pulse on axis and therefore, bends the phase fronts towards the axis. Relativistic self focusing becomes relevant if the laser power exceeds the critical power [70–72]

$$P_{cr} = 8\pi\epsilon_0 \frac{m_e^2 c^5}{e^2} \left(\frac{\omega_L}{\omega_p}\right)^2 \approx 17.2 \frac{\omega_L^2}{\omega_p^2}\,\mathrm{GW}. \tag{2.24}$$

However, the critical power can be reduced by **ponderomotive self focusing** [70,73] where electrons are driven away from the laser axis by the ponderomotive force of the laser, which induces a focusing gradient in the index of refraction.

Due to natural diffraction, the focal spot area of a Gaussian beam is increased by a factor of 2 at a distance x_R from the waist (cf. Fig. 2.1(a)). Nevertheless, if the laser pulse is focused to the matched spot size $w_m \propto \lambda_p \sqrt{a_0}$ [74–76], the laser pulse is **self guided** and

natural diffraction can be compensated by self-focusing over several Rayleigh lengths.

Envelope self-modulation. A laser pulse extending over several plasma wave periods experiences periodic focusing and de-focusing gradients in the transverse electron density gradients which change their sign within one plasma wave period. Therefore, the laser pulse develops an intensity profile which is longitudinally modulated with λ_p.

2.3 Electron Acceleration in Plasma Waves

In the longitudinal electric fields of a plasma wave generated by an intense laser pulse, electrons can be accelerated to velocities close to the speed of light. In this section, the acceleration process is explained in detail. After a basic introduction to the laser wakefield acceleration in one dimension, different regimes are introduced in 3D followed by further effects associated with the acceleration process.

2.3.1 Analytic Model in One Dimension

2.3.1.1 Plasma Wave Generation

A plasma wave is a periodic electron density modulation, which can be described with the Poisson equation. Its generation is the consequence of the ponderomotive force exerted by the laser pulse and collective behaviour. It is generated most efficiently if the pulse duration of the exciting laser pulse fits into one half period $\lambda_p/2$ ***of the plasma wave.***

While the plasma electrons are expelled from regions of high intensity by the ponderomotive force, the plasma ions can be assumed to remain stationary due to their lower charge to mass ratio (cf. section 2.2.2). This leads to the modulation of the equilibrium electron density n_{e0} with an electron density perturbation $\delta n_e(x)$ and thus, the local electron density is given by $n_e(x) = n_{e0} + \delta n_e(x)$. The charge separation described by $\delta n_e(x)$ leads to space-charge fields which force the electrons to return to their initial positions where they overshoot due to inertia resulting in electron oscillations with the plasma frequency ω_p. The collective excitation of these oscillations by the laser pulse propagating through the plasma with its group velocity $v_{g,L}$ generates a plasma wave – also referred to as wakefield – with a phase velocity $v_{\Phi,p} = v_{g,L}$. In terms of the electron density, a plasma wave can be described as a periodic electron density modulation with a wavelength $\lambda_p = 2\pi v_{\Phi,p}/\omega_p$. Plasma waves are resonantly driven when the longitudinal extent of the laser pulse given by its pulse duration τ_L fits into one half cycle of the plasma wave [8], i.e.,

$$\tau_L = \lambda_p/(2v_{g,L}), \tag{2.25}$$

with $\lambda_p = 2\pi c/\omega_p = 2\pi c\sqrt{\frac{\epsilon_0 m_e}{n_e e^2}} \propto 1/\sqrt{n_e}$. For a laser pulse with $\tau_L \approx 30\,\mathrm{fs}$, as for example is provided by the JETI40 laser system, the ideal plasma wavelength would be $\lambda_p \approx 18\mu\mathrm{m}$

corresponding to an electron density of $n_e \approx 3.5 \times 10^{18}\text{cm}^{-3}$. However, we will see in section 2.3.2 that this ideal condition is not necessarily fulfilled in experiments.

The periodic electron density modulation of the plasma wave generates an electric field $\mathcal{E}$ which – at least in a 1-dimensional situation – is purely longitudinal and can be described with the Poisson equation

$$-\frac{\partial^2}{\partial\xi^2}\phi(\xi) = \frac{\partial}{\partial\xi}\mathcal{E}(\xi) = \frac{\rho}{\epsilon_0} = \frac{e}{\epsilon_0}\Big(n_i(\xi) - n_e(\xi)\Big) = -\frac{e}{\epsilon_0}\delta n_e(\xi), \tag{2.26}$$

where ϕ is the electro-static potential and the parameter $\xi = x - v_{ph,p}\,t$ represents the longitudinal position in a frame of reference co-moving with the laser pulse and the plasma wave.

2.3.1.2 Linear and Nonlinear Plasma Waves

In the half periods of a plasma wave, which have a negative longitudinal electric field, electrons can be accelerated in propagation direction of the driving laser pulse. Depending on the intensity of the driving laser pulse, a plasma wave can be linear (low intensity) or nonlinear (high intensity). While a linear plasma wave exhibits an approximately sinusoidal electron density modulation and electric field, a nonlinear plasma wave has sharp electron density spikes and a sawtooth-like electric field, which between two adjacent electron density peaks is approximately linear.

In terms of the normalised vector potential profile $a = |\vec{\mathcal{A}}|e/(m_e c)$ of the laser pulse and normalised electric potential profile $\hat{\phi} = \phi e/(m_e c^2)$ of the plasma wave, Eq. 2.26 can be written as [10, 77]

$$\frac{1}{k_p^2}\frac{\partial^2\hat{\phi}}{\partial\xi^2} = \gamma_{\Phi,p}^2\left\{\beta_{\Phi,p}\left[1 - \frac{1+a^2}{\gamma_{\Phi,p}^2(1+\hat{\phi})^2}\right]^{-1/2} - 1\right\}, \tag{2.27}$$

which can be derived by incorporating the equation of motion (Eq. 2.11), the electric and magnetic fields expressed by the potentials (Eq. 2.2) and the continuity equation $\frac{\partial n_e(\xi)}{\partial\tau} + c\frac{\partial(n_e\beta_\xi)}{\partial x}$, where $\tau = t$ and $\beta_\xi = v_\xi/c$ is the normalised velocity in the co-moving frame of reference. For underdense plasmas we can assume $v_{\Phi,p} \approx c$ from which we find $\beta_{\Phi,p} = v_{\Phi,p}/c \approx 1$ as well as $\gamma_{\Phi,p}^2 = 1/(1-\beta_{\Phi,p}^2) = n_{cr}/n_e \gg 1$. Therefore, Eq. (2.27) can be simplified to [10, 77]

$$\frac{1}{k_p^2}\frac{\partial^2\hat{\phi}}{\partial\xi^2} = \frac{1}{2}\left[\frac{1+a_0^2}{(1+\hat{\phi})^2} - 1\right]. \tag{2.28}$$

For a top-hat laser pulse (THP), this expression can be solved analytically and for example, the maximum electric field [10, 77]

$$\mathcal{E}_{max} = \frac{m_e c\omega_p}{e}\frac{a_0^2/2}{\sqrt{1+a_0^2/2}}, \tag{2.29}$$

can be obtained. The relativistic mass increase of electrons oscillating in the field of a highly intense laser pulse ($a_0^2 \gg 1$) reduces the local plasma frequency and thus, causes a lengthening of the plasma wave. For a THP, this relativistically increased, nonlinear plasma wavelength can be written as [10, 77, 78]

$$\lambda_{p,nl} \approx \frac{2}{\pi} \frac{a_0^2/2}{\sqrt{(1 + a_0^2/2)}} \lambda_p. \tag{2.30}$$

For arbitrary pulse shapes, Eq. (2.28) has to be solved numerically. In the following, Gaussian laser pulses described by $a = a_0\, e^{-(\xi/\xi_0)^2} \cos(k_L \xi)$ are considered where the wave number $k_L = 2\pi/\lambda_L$ is determined by the laser wavelength $\lambda_L = 0.8\,\mu$m. Furthermore, the pulse duration is given in terms of the pulse's length in the longitudinal coordinate $\xi_0 = \frac{1}{2\sqrt{\ln 2}}\, \xi_{FWHM}$ where the FWHM pulse duration $\xi_{FWHM} = \frac{1}{2}\lambda_p$ was chosen to match the resonance condition described in section 2.3.1.1.

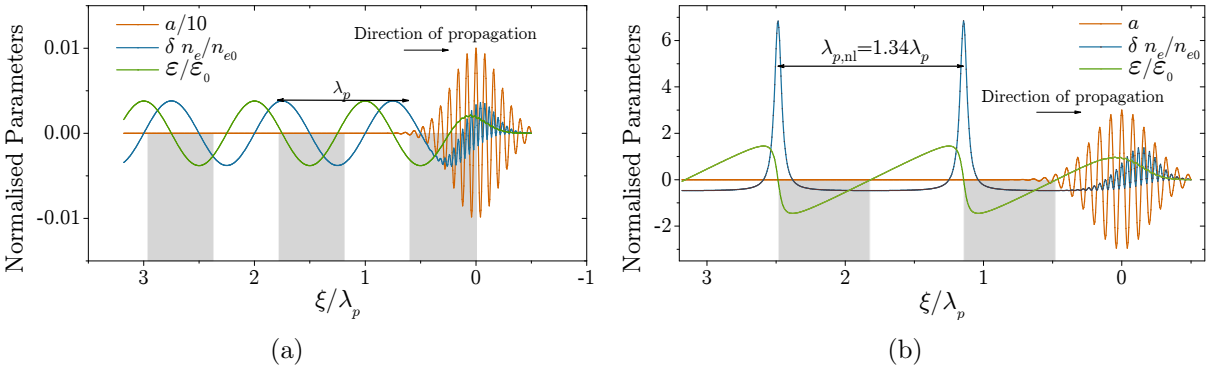

Figure 2.5 *Normalised electron density perturbation $\delta n_e/n_{e0}$ and normalised electric field $\mathcal{E}/\mathcal{E}_0$ of (a) a linear and (b) a nonlinear plasma wave excited with Gaussian laser pulses with (a) $a_0 = 0.1$ and (b) $a_0 = 3$, respectively. Note the different scales of the vertical axis. While the electric field of the linear plasma wave is approximately sinusoidal, the field of the nonlinear plasma wave is quasi-linear between two electron density peaks.*

Fig. 2.5(a) shows the solution of Eq. (2.28) for a linear plasma wave ($\mathcal{E}/\mathcal{E}_0 \ll 1$) excited by a laser pulse with $a_0 = 0.1$. Note that a in Fig. 2.5(a) is downscaled by a factor of 0.1 to improve the visibility of the the normalised electron density perturbation $\delta n_e/n_{e0}$ and the normalised electric field $\mathcal{E}/\mathcal{E}_0$ which behind the laser pulse have an approximately sinusoidal shape. In contrast, the stronger pulse in Fig. 2.5(b) with $a_0 = 3$ generates a nonlinear plasma wave ($\mathcal{E}/\mathcal{E}_0 > 1$) with narrow large amplitude density peaks and a sawtooth-shaped electric field, which between two electron density peaks is approximately linear. Compared to the sinusoidal plasma wave in Fig. 2.5(a), the plasma wave in Fig. 2.5(b) is nonlinearly lengthened by a factor of 1.34 whereas the equation derived for the THP predicts a lengthening by a factor of 1.34 for $a_0 = 3$. In the negative half periods of the plasma wave's longitudinal electric field (grey shaded regions in Figs. 2.5(a) and 2.5(b)),

electrons can be accelerated in the direction of propagation of laser pulse and plasma wave.

2.3.1.3 Maximum Achievable Electric Field and Self-Injection

Through the breaking of a plasma wave, electrons are self-injected into the wave's accelerating field. Longitudinal wavebreaking occurs, when the oscillation velocity of single electrons exceeds the phase velocity of the wave. Therefore, the maximum achievable electric field of a plasma wave is limited. In three dimensions, transverse wavebreaking can already occur in plasma waves with lower electric fields.

The maximum of the electric field amplitude of a plasma wave is limited by **longitudinal wavebreaking**, which takes place when the plasma wave electron's maximum oscillation velocity exceeds the phase velocity of the wave. In this process, the corresponding electrons leave the plasma wave's electron density peak and enter the wave's accelerating field, i.e., they are **self injected** into the plasma wave and can be accelerated to velocities close to the speed of light if they are trapped by the wave (cf. section 2.3.1.4). Assuming that all electrons oscillate with $k_p = \omega_p/c$, the cold nonrelativisitic wave breaking field [9]

$$\mathcal{E}_0 = \frac{m_e c \omega_p}{e} \approx 96\,\mathrm{GV}\sqrt{n_{e0}\,[\mathrm{cm}^{-3}]}, \tag{2.31}$$

can be estimated using the Poisson equation. Nevertheless, with increasing driver pulse intensity, the relativistic mass increase $\gamma_{\Phi,p}$ of the oscillating electrons has to be taken into account. The associated cold relativistic wave breaking limit [79]

$$\mathcal{E}_{wb} = \mathcal{E}_0\sqrt{2(\gamma_{\Phi,p} - 1)}, \tag{2.32}$$

exceeds $\mathcal{E}_0$ if $\gamma_{\Phi,p} > 3/2$.

Transverse wavebreaking. Fig. 2.6(a) shows a flat (grey) and a parabolic (black) plasma wave phase front. Here, ξ is the longitudinal and z the transverse coordinate with the laser axis at $z = 0$. For electron injection to occur in a plasma wave with flat phase fronts, the oscillation amplitude has to exceed the plasma wavelength (longitudinal wavebreaking). However, as a consequence of curved plasma wave phase fronts in higher dimensional systems [80], trajectory crossings can already occur at lower oscillation amplitudes. This phenomenon is referred to as transverse wavebreaking and reduces the wavebreaking limit below $\mathcal{E}_{wb}$. Nevertheless, 2 and 3 dimensional PIC simulations show that plasma waves with electric fields above $\mathcal{E}_0$ can be generated [10].

A curved phase front implies a transverse variation of the plasma wavelength $\lambda_{p,nl} \propto \gamma_{\Phi,p}/\sqrt{n_e}$, which can be realised by a radially increasing electron density profile $n_e(z)$ as e.g. formed by a plasma wave guide. Moreover, the transverse intensity profile of the laser pulse, which has its maximum on the laser axis causes a stronger relativistic mass increase (cf. Eq. (2.30)) of the plasma wave electrons on the laser axis also resulting in a radially

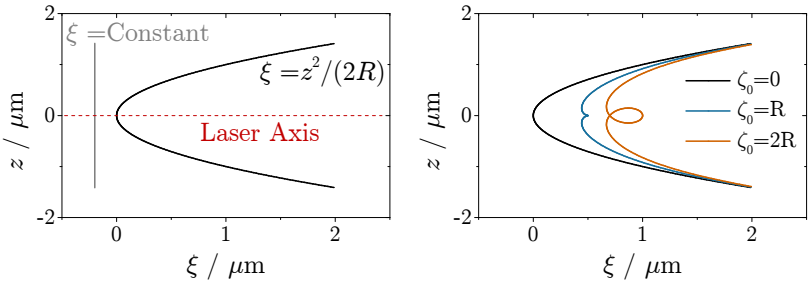

Figure 2.6 *Transverse wave-breaking. (a) Constant and curved wavefront. (b) Deviation from curved wavefront due to the oscillation of the electrons with different amplitudes* $\zeta = \zeta_0 e^{-2z_0^2}$ *transverse to their wavefronts.*

decreasing plasma wavelength.

The black curves in Figs. 2.6(a) and 2.6(b) are a parabolic phase front given by

$$\xi = z^2/(2R), \tag{2.33}$$

with a curvature $1/R$. Parametrised by z_0, which in z-direction represents the distance to the laser axis, the first terms in Eqs. (2.34) and (2.35)

$$\xi = \frac{z_0^2}{2R} + \frac{\zeta(z_0)R}{(R^2 + z_0^2)^{0.5}}, \tag{2.34}$$

$$z = z_0 - \frac{\zeta(z_0)z_0}{(R^2 + z_0^2)^{0.5}}, \tag{2.35}$$

are an alternative representation of Eq. (2.33). Furthermore, the second terms in Eqs. (2.34) and (2.35) describe the shift of the phase fronts resulting from the oscillation of the plasma wave electrons normally to the phase front with the oscillation amplitude $\zeta(z_0) = \zeta_0 e^{-2z_0^2}$. The radial decrease of $\zeta(z_0)$ accounts for the laser pulse's intensity profile, which also decreases with distance to the axis of symmetry. For $\zeta_0 = R$, the phase fronts begin to cross. Moreover, for $\zeta_0 > R$ (orange), trajectory crossing takes place on the inner side of the of the phase front, i.e., electrons are injected into the accelerating phase of the plasma wave.

2.3.1.4 Electron Motions in Phase Space and Trapping

Electron trapping by the plasma wave and the subsequent acceleration process can be described in phase space, which here is spanned by the normalised momentum $p_\xi/(m_e c)$ ***and the normalised longitudinal coordinate*** ξ/λ_p***. In this representation, electrons are tied to a defined trajectory, which determines their maximum achievable momentum or energy, respectively.***

In phase space spanned by the normalised momentum $p_\xi/(m_e c)$ and the normalised longitudinal coordinate ξ/λ_p of a 1-dimensional wakefield in the co-moving frame of reference, electron trajectories are represented by the solution of the Hamiltonian [81]

$$h(\xi, p_\xi) = \sqrt{1 + p_\xi^2 + \hat{a}(\xi)^2} - \hat{\phi}(\xi) - \beta_{\Phi,p} p_\xi = h_0 = constant, \tag{2.36}$$

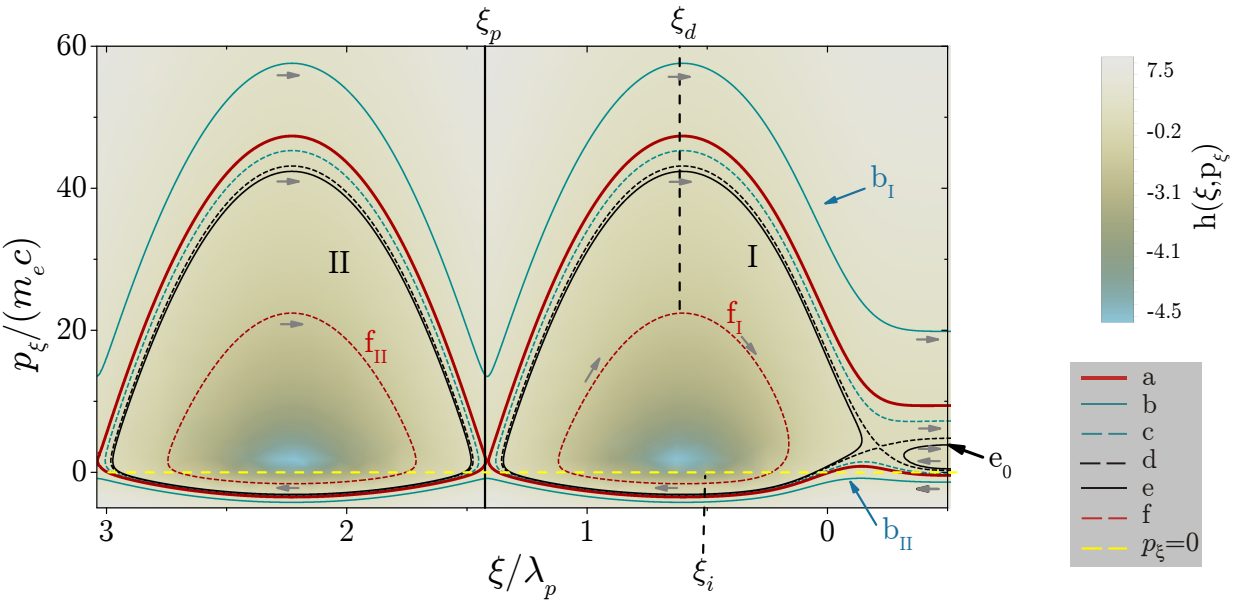

Figure 2.7 *Electron acceleration and deceleration in a plasma wave in phase space* $(p/(m_e c), k_p\xi)$. *The red solid line is the separatrix representing the boundary between different plasma wave periods. Trapped electrons are accelerated and decelerated along the orbits within the separatrix.*

where a given trajectory corresponds to a value $h_0 = constant$. Fig. 2.7 shows a phase space where the peak of the laser pulse is situated at $\xi/\lambda_p = 0$. $a(\xi)$ and $\hat{\phi}(\xi)$ are adopted from the nonlinear plasma wave in section 2.3.1.2 and $\beta_{\Phi,p}$ is determined by $\gamma_{\Phi,p} = (1-\beta_{\Phi,p}^2)^{(-1/2)} = \sqrt{1-a_0^2}$ and is associated to the plasma wave electrons. Electron trajectories (a-e) are shown as lines where all trajectories corresponding to the same h_0 are represented in the same line style. Electrons are tied to a specific trajectory and cannot switch from e.g. trajectory f_I to trajectory f_{II} or e_0. The direction of movement (grey arrows) along an arbitrary trajectory is determined by the sign of $p_\xi/(m_e c)$. Electrons with $p_\xi/(m_e c) < 0$ are slower than the phase of the wakefield and hence, move backwards with respect to the plasma wave and vice versa for $p_\xi/(m_e c) > 0$.

The thick red line (a) is the separatrix, which represents the boundary between background (b) and trapped electron (c-f) trajectories. Electrons on trajectories below the separatrix, here b_{II}, are too slow to be trapped and form the wakefield whereas electrons on b_I are too fast. Note that those background electrons also experience the electric field of the plasma wave and therefore, are periodically accelerated and decelerated.

At the positions, where the separatrix lines cross (e.g. at $\xi = \xi_p$, solid vertical line), the plasma wave has its density peaks. These positions mark the boundaries between the different plasma wave periods. Hence, the phase space inside the separatrix corresponds to the first (I) and the second (II) plasma wave periods. Note, that the trajectories with the same h_0 can behave differently in different plasma wave periods. While in II, c-f are closed

orbits, c is an open trajectory in I and d marks the transition between open and closed trajectories.

While electron injection cannot be described in this representation, electron trapping can be understood. Consider an electron injected onto trajectory f_I at the position ξ_i, which might occur through transverse wavebreaking (cf. section 2.3.1.3) or controlled injection (cf. section 2.3.3). As $p_\xi/(m_e c) < 0$, the electron propagates backwards with respect to the wave. However, it experiences the electric field of the plasma wave and gains a momentum $p_\xi/(m_e c) > 0$ before it has reached the rear of the plasma wave period [3] at $\xi = \xi_p$ and moves up in phase space – i.e., it is accelerated – until the position ξ_d where the electron has gained its maximum achievable momentum. After the electron has passed ξ_d, it experiences the positive electric field of the the wave where the electron's momentum is reduced causing the electron to move down in phase space. This process is called dephasing. In a plasma wave driven by a static laser pulse in an infinitely extended plasma, electrons on the closed orbit f_I are continuously accelerated and decelerated. Nevertheless, laser energy is transferred to the plasma and hence, the plasma wave cannot be driven infinitely long. In fact, LWFA is usually terminated (e.g. by limiting the length of the plasma) when the electrons reach the highest momentum for the first time, i.e., they do not go through a full revolution in such a phase-space plot. When the electron reaches its maximum momentum in phase space, it has been accelerated along the desired maximum acceleration length limited by dephasing. The maximum acceleration length, which can be limited by dephasing as described so far but also by depletion or diffraction is discussed in detail in the following section.

Trajectory c is referred to as "run-away" trajectory on which electrons can overtake the laser pulse as the lower charge separation at the position of the laser pulse does not provide a sufficiently strong electric field to decelerate the electrons below $p_\xi/(m_e c) = 0$. Furthermore, electrons on the trajectory e_0 are reflected by the ponderomotive potential of the laser pulse.

2.3.1.5 Maximum Acceleration Distance

The acceleration distance can be limited by dephasing, which takes place when the electrons outrun the plasma waves accelerating field, by pump depletion, which occurs when the laser pulse has transferred its energy to the plasma and by natural diffraction.

Dephasing. Electrons can be accelerated as long as they experience the negative longitudinal electric field ranging over one half period of the plasma wave. The phase of the plasma wave propagates with $v_{\Phi,p} \approx \eta c < c$, which in the phase space picture introduced

[3] Trapping of electrons injected at $\xi \approx \xi_p$ e.g. through longitudinal wavebreaking requires an initial electron momentum $p_e \geq 0$. Although in the case of longitudinal wavebreaking, the maximum oscillation velocity of the electrons satisfies this condition, they might still not be trapped as their average momentum in the co-moving frame of reference might be $p_\xi < 0$.

above corresponds to $p_\xi = 0$ (cf. Fig. 2.7). Trapped electrons are accelerated to velocities of $v_e > v_{\Phi,p}$, i.e, to $p_\xi > 0$ in the phase space representation in Fig. 2.7. Those electrons move forward inside the plasma wave and are decelerated as soon as the electrons reach the positive $\vec{\mathcal{E}}$-field of the wave, which in Fig. 2.7 occurs at the position ξ_d. Although in section 2.3.1.4, electrons where assumed to be injected at an arbitrary position ξ_i within the first plasma wave period, here we will assume that the electrons are injected at the rear of the plasma wave to allow for a simple estimation of the dephasing length, which is explained in more detail in section 4.4.1 where the nonlinear dephasing length is calculated from data obtained in the experiment. With an electron velocity $v_e \approx c$, the dephasing length is given by [10, 82, 83]

$$l_{dph} = \frac{\lambda_p^3}{\lambda_L^2} \begin{cases} 1 & \text{for} \quad a_0^2 \ll 1, \\ \frac{\sqrt{2}}{\pi} a_0 & \text{for} \quad a_0^2 \gg 1, \end{cases} \tag{2.37}$$

for linear and nonlinear plasma waves, respectively. The increase of the dephasing length for $a_0^2 \gg 1$ can be attributed to the relativistic lengthening of the plasma wave (Eq. (2.30)). In a longitudinally decreasing electron density profile, the dephasing length can be extended.

Laser pulse depletion limits the distance over which the plasma wave can be driven by the laser pulse. When the laser pulse is depleted, i.e, when all of its energy is transferred to the plasma wave or background plasma, the plasma wave is no longer driven and hence, the accelerating electric field vanishes. Assuming that the laser pulse transfers its energy exclusively to the electron oscillations of the plasma wave, the depletion length can be approximated to [10, 82, 83]

$$l_{dpl} = \frac{\lambda_p^3}{\lambda_L^2} \begin{cases} \frac{2}{a_0^2} & \text{for} \quad a_0^2 \ll 1, \\ \frac{\sqrt{2}}{\pi} a_0 & \text{for} \quad a_0^2 \gg 1. \end{cases} \tag{2.38}$$

Acceleration in linear plasma waves is limited by dephasing as $l_{dph} < l_{dpl}$. For nonlinear plasma waves, dephasing and depletion length are identical (cf. Eqs. (2.37) and (2.38)). A decreasing electron density along the laser propagation direction increases the plasma wavelength and thus, the depletion length [84–86]. Pump depletion can be overcome through staged acceleration in subsequent laser wakefield accelerator stages driven by synchronised laser pulses [25]. Both, the dephasing and depletion lengths are calculated for a top-hat laser pulse.

Diffraction. As mentioned above, a focused laser pulse in vacuum is subject to natural diffraction which causes a decrease of laser intensity. However, focusing effects induced by the interaction of the laser pulse with the plasma can significantly extend the length over which the focus is maintained (see section 2.2.3). Those focusing effects can be optimised by a gas-filled capillary discharge waveguide with a radially increasing electron density

profile [87].

2.3.1.6 Maximum Electron Energy Gain

Assuming dephasing as the limit to the acceleration distance, the maximum electron energy gain depends on the electron density in the case of acceleration in a linear plasma wave whereas in the case of a nonlinear plasma wave it depends on both, the electron density and the laser intensity.

The energy gain in the electric field of a plasma wave can be estimated with

$$E_{max} = -e \int_0^{x_{max}} \mathcal{E}_x dx, \tag{2.39}$$

where x_{max} is the maximum acceleration distance. Employing the linearly increasing part of the electric field of a nonlinear plasma wave (cf. Fig. 2.5(b)) of one plasma wave period and assuming dephasing as limit to the acceleration distance, the maximum energy gain is given by

$$E_{max} = \frac{e}{2}\mathcal{E}_{max}\frac{\lambda_p^3}{\lambda_L^2}\begin{cases} 1 & \text{for} \quad a_0^2 \ll, 1 \\ \frac{\sqrt{2}}{\pi}a_0 & \text{for} \quad a_0^2 \gg 1, \end{cases} \tag{2.40}$$

for a linearly polarised flat-top laser pulse where $\mathcal{E}_{max} \propto \sqrt{n_e}$ is the maximum of the accelerating field. Since $\lambda_p \propto 1/\sqrt{n_e}$, the maximum energy gain $E_{max} \propto 1/n_e$ decreases with increasing electron density.

2.3.2 Different Regimes of Laser Wakefield Acceleration

Under ideal conditions, the laser pulse is focused to the matched spot size and its pulse duration fits into one half period of the plasma wave. Nevertheless, electron acceleration in non-ideal plasma waves is possible.

In one dimension, the generation of the wakefield is most efficient if the laser pulse fits into one half cycle of the plasma wave, which has implications for the electron density. More precisely, $\tau_L \simeq \lambda_p/(2v_{g,L})$ with $\lambda_p \propto n_e^{-1/2}$ (cf. section 2.3.1.1). Furthermore, the generation of a strong wakefield in three dimensions over distances significantly longer than the Rayleigh length requires a matched focal spot size $w_m \propto \lambda_p\sqrt{a_0}$ (cf. section 2.2.3). Nevertheless, depending on the available laser energy and the pulse duration of the laser system, optimum plasma wave excitation and electron injection (cf. sections 2.3.1.1 and 2.3.1.3) might not be possible simultaneously. In this section, different acceleration regimes and scaling laws are introduced.

Blow-out regime: $a_0 \gtrsim 2$**.** In the blow-out regime, the first plasma wave period is fully cavitated and is commonly referred to as bubble. Moreover, the matched spot size w_m is given by the blow out radius R_{bo}. This regime was investigated using PIC-simulations in a highly and a moderately nonlinear scenario.

In the **highly nonlinear broken wave regime** [18] where $a_0 \gg 1$, trailing laser periods are destroyed due to wavebreaking and the electron energy spectrum features a sharp peak at high energies with a low energy tail due to continuous injection. The simulation employs a laser pulse with a pulse duration of initially $\tau = 33\,\mathrm{fs}$ and a normalised vector potential $a_0 = 10$ whereas laser wakefield acceleration experiments performed with state of the art laser systems use laser pulses with e.g. $\tau = 40\,\mathrm{fs}$ and $a_0 = 1.6$ [24] or $\tau = 150\,\mathrm{fs}$ and $a_0 < 2$ [23]. The **Pukhov-Gordienko-scaling** [76, 88] allows to predict the maximum electron energy gain in the highly nonlinear broken wave regime and introduces a similarity parameter $S = \frac{n_e}{a_0 n_c}$, where $S = \mathit{constant}$ implies similar laser plasma interactions. In the case of $S \ll 1$, i.e., in a relativistically underdense plasma, highly energetic electrons can be generated. Optimum interaction conditions are given by the matched spot size $w_m \simeq R_{bo} = 1.12\sqrt{a_0}/k_p$ and the pulse duration $\tau_L \leq R_{bo}/c$. The maximum electron energy gain

$$E_{max} = 0.65 m_e c^2 \sqrt{\frac{P}{P_{rel}}} \frac{c\tau}{\lambda_L}, \tag{2.41}$$

with $P_{rel} = 8.5\,\mathrm{GW}$ is limited by pump depletion, where the depletion length is given by $l_{dpl} = 0.7 \frac{c\tau}{\lambda_L} \frac{\pi R^2}{\lambda_L}$.

In contrast, the more **moderate regime** $2 \leq a_0 \leq 4$ can be investigated with state of the art lasers. Here, the maximum electron energy gain can be estimated with the **Lu-Scaling**. Assuming the front of the laser pulse to be continuously pump depleted, the group velocity of the laser pulse $v_{g,L}$ and thus, the phase velocity of the plasma wave $v_{\Phi,p}$ is effectively reduced. The decreased dephasing length is stated as $l_{dph} = \frac{2}{3} \frac{\omega_L^2}{\omega_p^2} R_{bo}$, where the blow out radius R_{bo} is determined by $k_p R_{bo} \simeq k_p w_m = 2\sqrt{a_0}$. Moreover, for acceleration until dephasing, an optimum pulse duration $c\tau_L > 2R_{bo}/3$ was found. The energy gain of the electrons accelerated in a a nonlinear plasma wave and therefore, an approximately linear electric field with a maximum given by $\mathcal{E}_{max} \simeq \sqrt{a_0}\mathcal{E}_0$, scales as [75]

$$E_{max}\,[\mathrm{GeV}] \simeq 1.7 \left(\frac{P\,[\mathrm{TW}]}{100} \right)^{1/3} \left(\frac{10^{18}}{n_{e0}\,[\mathrm{cm}^{-3}]} \right)^{2/3} \left(\frac{0.8}{\lambda_L\,[\mu\mathrm{m}]} \right)^{4/3}. \tag{2.42}$$

Electron distributions peaked at $E_{max} \approx 145\,\mathrm{MeV}$ can be observed frequently with the JETI40-pulses [52]. The corresponding experimental parameters are $n_e \approx 1.65 \times 10^{19}\,\mathrm{cm}^{-3}$, and $a_0 \approx 1.7$ or $P \approx 20\,\mathrm{TW}$, respectively. The Lu-scaling predicts an electron energy gain of 153 MeV, which is in very good agreement with the experimental result. Since the Pukhov-Gordienko scaling was not developed for this experimental parameter range, its prediction – 183 MeV – deviates more strongly from the experimental result.

Self-modulated laser wakefield acceleration: $a_0 \lesssim 1$, $\tau_L v_{g,L} > \lambda_p$**.** For laser

pulses with $a_0 \approx 1$, self-injection of electrons usually requires laser pulse evolution inside high electron densities and thus, the resonance condition is not fulfilled. When the laser pulse longitudinally extends over several plasma wave periods, the envelope of the laser pulse is modulated and splits into pulselets separated by λ_p [89] (cf. section 2.2.3). Those pulselets can drive the plasma wave resonantly in several periods. In experiments in the self-modulated regime, mostly electron spectra with large energy spreads were obtained [14–17]. However, also peaked spectra could be observed [90]. This was attributed to the laser pulse's modulation in the plasma resulting in a short and intense pulse.

Intermediate regime: $1 \lesssim a_0 \lesssim 2$**.** The experiments reported in this thesis were carried out with $a_0 = 1 \ldots 1.6$ and electron densities in a range of $(0.77...1.30) \times 10^{19}\mathrm{cm}^{-3}$, which for resonant plasma wave excitation require pulse durations of (20...15) fs. However, the actual pulse duration was $\approx 30\,\mathrm{fs}$. While an initially long laser pulse $\tau_L > \lambda_p/(2c)$ in a constant density will most likely be self modulated, the same pulse might be compressed through self phase modulation (cf. section 2.2.3) in a rising electron density such that resonant excitation exclusively in the first plasma wave period might be possible. PIC-simulations performed in a comparable parameter range show that the majority of the laser pulse is situated at the first plasma wave period which is nearly cavitated [52, 91].

2.3.3 Controlled Injection of Electrons into Low Amplitude Plasma Waves

Self injection of electrons into the plasma wave for subsequent acceleration is the consequence of the highly nonlinear interaction of laser pulse and plasma wave and hence, the parameters of the self injected and then accelerated electron bunches can differ drastically from shot to shot. Through controlled injection of electrons into the accelerating phase of the plasma wave those large shot-to-shot fluctuations can be reduced.

Ionisation injection. As explained in section 2.2.2, helium is fully ionised below laser intensities of $I_L = 10^{17}\,\mathrm{W/cm}^2$, i.e., in front of the peak of a highly intense laser pulse ($I_0 \geq 10^{18}\,\mathrm{W/cm}^2$). Nevertheless, with increasing ionisation state, gases with a higher atomic number, e.g., nitrogen, have considerably higher ionisation energies (cf. Table 2.1) and therefore, higher threshold intensities I_{th} for full ionisation (cf. section 2.2.2). With the JETI40-laser pulses, the highest ionisation states of nitrogen can only be achieved at the peak of the laser pulse, i.e., electrons can be ionised and immediately be injected into the plasma wave, which can occur at any position (ξ, p_ξ) in the phase space plot representation shown in Fig. 2.7. Therefore, with this injection method only broadband electron energy spectra can be generated [33–37, 92].

Colliding pulse injection. A strong pump pulse generates a wakefield with the wavelength λ_p while a weaker pulse propagates on the same axis but in the opposite direction such

that the two pulses collide. At their collision position, a standing wave with $\lambda_s = \lambda_L/2 \ll \lambda_p$ determined by the wavelength λ_L of the colliding pulses is generated. The large ponderomotive force of the standing wave pre-accelerates electrons, which can be trapped by the plasma wave. The variation of the collision position of the two pulses allows control over the energy of the accelerated bunch [40].

Density transition injection. Fig. 2.8 illustrates the propagation of a laser pulse in

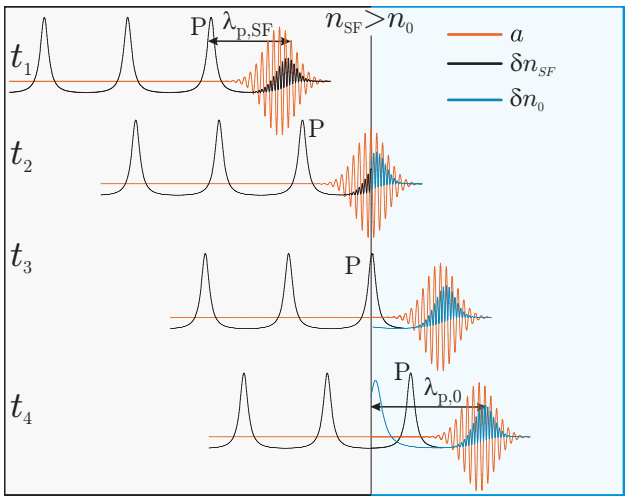

Figure 2.8 *A laser pulse propagates through a sudden density transition with $n_{SF} > n_0$. The plasma wave generated by the laser pulse experiences a sudden lengthening and the electrons from the plasma wave peak P generated in the higher electron density n_{SF} can be injected into the accelerating phase of the plasma wave generated in the lower electron density n_0.*

a plasma with a sudden density transition from n_{SF} (grey shaded area) to n_0 (blue shaded area) with $n_{SF}/n_0 =: r_n > 1$. However, both densities are still sufficiently low to avoid self injection. Equivalently, the plasma wavelengths are related as $\lambda_{p,SF}/\lambda_{p,0} = (r_n)^{(-1/2)}$, i.e., the decrease in electron density results in an increase in plasma wavelength. Since $v_{\Phi,p} = c\sqrt{1 - n_e/n_{cr}}$ and $n_e \ll n_{cr}$ in the relevant electron density regime, the change in phase velocity at the front of the plasma wave is negligible and $v_{\Phi,p} = const.$ will be used in both densities.

At the time $t = t_1$, the laser pulse has generated a weakly nonlinear plasma wave (black line) with a wavelength $\lambda_{p,SF}$ in the density n_{SF}. Laser and plasma wave propagate towards the density transition where they arrive at $t = t_2$. The plasma wave formed in n_0 is shown as a blue line. When the peak P arrives at the transition at $t = t3$, the laser pulse has propagated a distance of $\approx \lambda_{p,SF} < \lambda_{p,0}$ away from the density transition and the first plasma wave period in n_0 is not fully developed yet. However, the electrons forming the electron density peak P still oscillate with the higher plasma frequency determined by n_{SF}, i.e., they are out of phase with the electron oscillations in n_0 and are injected into the newly formed plasma wave. At the time $t = t_4$, the rear of the new plasma wave is formed and the injected electrons experience the accelerating field.

Electron bunches with tunable electron energies were demonstrated [47,48] in dependence on the position of the density transition inside the target and therefore, the remaining ac-

celeration length. The low energy spread of the accelerated electron bunches was attributed to the very isolated position of injection determined by the width of the transition on the order of the plasma wavelength or shorter. The authors emphasise the difference to **density downramp injection** where the transition is longer than the plasma wavelength and the gradual change of the plasma wavelength leads to continuous injection and therefore, broad electron energy distributions [93].

2.3.4 Wavebreaking Radiation

Broadband radiation is emitted when electrons are injected into the plasma wave.

Injection and trapping of electrons by the wakefield – independent of the method of injection – is connected to the emission of electromagnetic radiation [94]. The broadband nature of this radiation which is typically emitted over a length of a few μm only was attributed to the rapid acceleration of the electrons directly after injection. Due to its inextricable correlation to wavebreaking, this broadband radiation was termed wavebreaking radiation. The emission of this radiation occurs primarily transverse to the direction of acceleration and can be described with the wave equation $\left[\nabla^2 - \frac{1}{c^2}\frac{\partial^2}{\partial t^2}\right]\frac{\partial \vec{\mathcal{A}}}{\partial t} = \mu_0 \frac{\partial \vec{j}}{\partial t}$ represented by the vector potential $\vec{\mathcal{A}}$.

2.3.5 Transverse Electron Movement - Betatron Oscillations

Off-axis injection or injection with initial momentum leads to oscillations of the injected electrons in the transverse electric fields of the plasma wave.

In a three-dimensional wakefield, radial electric fields are generated due to charge separations in transverse direction. Thus, an electron injected off-axis or with initial transverse momentum experiences a restoring force $\frac{\mathrm{d}}{\mathrm{d}t^2}\gamma m_e \vec{r} = -m_e \frac{\omega_p^2}{2}\vec{r}$ where $\vec{r}$ denotes the electron's transverse position with respect to the laser axis. Assuming $\gamma = const.$, the solution of this differential equation is a sinusoidal oscillation with the Betatron frequency

$$\omega_\beta = \frac{\omega_p}{\sqrt{2\gamma}}. \tag{2.43}$$

Hence, the movement of an electron inside the wakefield is an acceleration in laser direction possibly superimposed with Betatron oscillations in transverse direction.

2.3.6 Azimuthal Magnetic Fields and Polarisation Effects

In the presence of a magnetic field, the state of polarisation of an electromagnetic beam propagating through a plasma is affected. While magnetic fields oriented parallel to the direction of propagation of the wave cause a rotation of the wave's plane of polarisation (Faraday effect), magnetic fields perpendicular to the direction of propagation of the wave induce a phase shift between the linear electric field components of the wave (Cotton-Mouton-effect).

In one dimension, the oscillating plasma wave electrons as well as the accelerated electrons can be described as an electron current $\vec{j_e} = -n_e e \vec{v_e}$ in laser propagation direction. In the same direction, the temporally varying electric field of the plasma wave induces a displacement current $\epsilon_0 \partial \mathcal{E} / \partial t$. Both types of current are surrounded by an azimuthal magnetic field which is described by Ampere's law $\vec{\nabla} \times \vec{\mathcal{B}} = \mu_0 (\vec{j_e} + \epsilon_0 \partial \mathcal{E} / \partial t)$.

An electromagnetic probe beam propagating through a plasma excites the plasma electrons to oscillate in its electric field, i.e., electromagnetic radiation is absorbed and re-emitted by the electrons. In the presence of an external magnetic field $\vec{\mathcal{B}}_{ext}$, the plasma electrons gyrate with the gyration frequency $\omega_g = \frac{e}{m_e} |\vec{\mathcal{B}}_{ext}|$ and the effective movement is an elliptic orbit around the $\mathcal{B}$-field vector with a sense of rotation given by the sign of $\vec{\mathcal{B}}_{ext}$. The additional electron movement breaks the symmetry of the system and causes phase shifts between equivalent electric field components.

Faraday effect. A linearly polarised wave with an electric field amplitude $\mathcal{E}_0$ and frequency ω_0 can be decomposed in two counter-rotating circular components with the same frequency and amplitudes $1/2\mathcal{E}_0$ however, opposite sense of rotation around its direction of propagation (cf. left hand side pictogram of Fig. 2.9). Together with the wave's electric

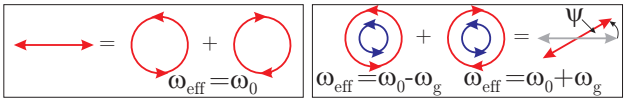

Figure 2.9 *Pictogram of the Faraday effect. Left hand side: Decomposition of the electric field (red) of a linearly polarised electromagnetic wave into its counter-rotating circularly polarised components. Right hand side: An electron gyration (blue) breaks the symmetry of the system and generates a phase difference between the circularly polarised components, which is equivalent to a rotation of the plane of polarisation by the angle ψ in the linear representation of the wave.*

field, a magnetic field $\vec{\mathcal{B}}_{\parallel}$ parallel to the waves direction of propagation excites an elliptic electron motion in the plane of the counter rotating electric field components (cf. right hand side pictogram of Fig. 2.9).

Due to their own rotation, the $\mathcal{E}$-field components experience this electron movement with different effective frequencies $\omega_{eff} = \omega_0 \pm \omega_g$ (cf. right hand side pictogram of Fig. 2.9) and thus, different indices of refraction $\eta_{eff} = \sqrt{1 - \omega_p^2 / \omega_{eff}^2}$. Since $v_{\Phi,probe} = c/\eta_{eff}$, the phase relation of the counter-rotating field components is changed, which for the linearly polarised wave is equivalent to a rotation of the plane of polarisation by the angle ψ. In a plasma, the incremental angle of Faraday rotation is given by [56, 95]

$$\mathrm{d}\psi = \frac{e}{2 m_e c \, n_{cr}} \frac{n_e}{\gamma} \vec{\mathcal{B}}_{\parallel} \mathrm{d}\vec{s}, \tag{2.44}$$

where $\mathrm{d}\vec{s}$ is the path element of the probe beams path through the plasma. The sense of rotation is counter-clockwise if $\vec{\mathcal{B}}_{\parallel}$ and $\mathrm{d}\vec{s}$ are parallel and vice versa if $\vec{\mathcal{B}}_{\parallel}$ and $\mathrm{d}\vec{s}$ are

antiparallel.

Cotton-Mouton effect. In the presence of an external magnetic field $\vec{\mathcal{B}}_\perp$ perpendicular to the propagation direction of the electromagnetic wave, the electrons' elliptic motion around $\vec{\mathcal{B}}_\perp$ affects the phase velocity of the linear field components which can be decomposed in a component parallel $\vec{\mathcal{E}}_\parallel$ and one perpendicular $\vec{\mathcal{E}}_\perp$ to $\vec{\mathcal{B}}_\perp$ (cf. left hand side pictogram of Fig. 2.10). While the elliptic motion is always perpendicular to $\vec{\mathcal{E}}_\parallel$, $\vec{\mathcal{E}}_\perp$ experiences parallel

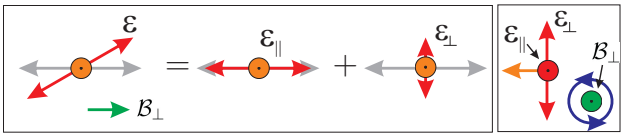

Figure 2.10 *Pictogram of the Cotton-Mouton effect. Left hand side: Decomposition of the electric field (red) of a linearly polarised electromagnetic wave into a parallel $\vec{\mathcal{E}}_\parallel$ and a perpendicular $\vec{\mathcal{E}}_\perp$ component with respect to an external magnetic field $\vec{\mathcal{B}}_\perp$ (green) directed perpendicularly to the propagation direction (orange) of the wave. Right hand side: The different orientation of the electric field components to the electron gyration (blue) around $\vec{\mathcal{B}}_\perp$ causes different indices of refraction and hence, generates a phase difference δ between $\vec{\mathcal{E}}_\parallel$ and $\vec{\mathcal{E}}_\perp$.*

and perpendicular motions (cf. right hand side pictogram of Fig. 2.10). The different relative motions cause different indices of diffraction and thus, a phase shift δ between $\vec{\mathcal{E}}_\parallel$ and $\vec{\mathcal{E}}_\perp$. Therefore, an initially linearly polarised wave becomes elliptically polarised. This effect is also referred to as magnetic birefringence. The incremental phase shift can be expressed as [95]

$$\mathrm{d}\delta = \frac{e^2}{2m_e^2 c\, n_{cr}\omega_0}\frac{n_e}{\gamma}\mathcal{B}_\perp^2 \mathrm{d}s. \tag{2.45}$$

Polarisation ellipse. Fig. 2.11(a) shows an elliptically polarised wave propagating

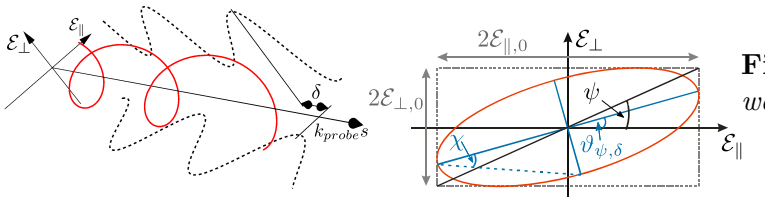

(a) (b)

Figure 2.11 *(a)Elliptically polarised wave and (b) polarisation ellipse.*

along $\vec{s}$ and with the electric field components $\mathcal{E}_\parallel$ and $\mathcal{E}_\perp$. The state of polarisation of such an electromagnetic wave is fully characterised by the amplitudes $\mathcal{E}_{\parallel,0}$ and $\mathcal{E}_{\perp,0}$ of the electric field components, which for a linearly polarised wave determine its plane of polarisation $\psi = \arctan(\mathcal{E}_{\perp,0}/\mathcal{E}_{\parallel,0})$, and the phase shift δ. While δ is clearly visible in this representation, ψ can be visualised in the $\vec{e}_\parallel - \vec{e}_\perp$-plane where the projection of the electric field appears as an ellipse inside a box with the dimensions $2\mathcal{E}_{\parallel,0}$ and $2\mathcal{E}_{\perp,0}$.

Here, δ is encrypted in $\sin(2\chi) = \sin(2\psi)\sin(\delta)$ where χ defines the ellipticity of the wave and in the ellipse's orientation inside the box $\vartheta_{\psi,\delta} = 1/2\arctan[\tan(2\psi)\cos(\delta)]$. In the

case $\delta = 45°$, the ellipse's long axis is oriented in $\vec{e}_{\parallel}$, i.e $\vartheta_{\psi,\delta} = 0°$ whereas for $\delta = 0°$, the ellipse collapses into a line with $\vartheta_{\psi,\delta} = \psi$.

2.4 Particle-In-Cell (PIC) Simulations

Laser plasma interactions are commonly computed with the help of particle in cell simulations. In an iterative algorithm, the nonlinear processes can be calculated in one-, two- or three-dimensional scenarios.

Since LWFA is a many body problem and is subject to nonlinear processes, its mathematical description is very complex. While there are analytic solutions for the 1D linear and nonlinear case, analytic solutions for 3D scenarios are only available for linear interactions. These 1D and 3D estimates are a good basis to plan experiments but the interpretation of concrete results often requires to simulate a scenario as similar to the real experiment as possible. PIC-simulations are a well-established method for the numerical investigation of laser-particle acceleration. Although 1D and 2D simulations are possible, 3D simulations describe the interaction more exactly as e.g. self focusing of the laser pulse in an underdense plasma is a three-dimensional process.

The acceleration process in a three-dimensional PIC simulation is described in a three-dimensional simulation box, which in laser wakefield acceleration simulations usually co-propagates with the laser pulse and the plasma wave and thus, represents only a part of the three-dimensional space to be simulated. The simulation box is subdivided into identical cells, where the size of the cells determines the spatial and temporal resolution of the simulation. Due to the complex nature of the processes, the simulations are computationally intensive. Therefore, each cell contains a defined number of macroparticles which represent a number of physical particles. In LWFA simulations, ionisation processes and ion motions are typically neglected. The algorithm is based on the calculation of

1. the electromagnetic fields generated by the motion of macroparticles,
2. the force on the macroparticles from those fields,
3. the macroparticle's velocity influenced by the force,
4. the macroparticle's position from the beforehand calculated velocity.

Simulations for this thesis where performed with EPOCH [96].

3. Experimental Setup and Data Analysis

This chapter covers the setup of the experiments reported in this thesis. At the beginning, an overview of the entire setup is provided, which is then step by step explained in more detail. In this context, the basic components of a laser wakefield acceleration experiment – the high intensity laser pulse and the gas target – are introduced. The properties of the electrons accelerated during the laser plasma interaction are recorded with an electron beam monitor and an electron spectrometer, which due to their common use in laser-plasma accelerators are only introduced briefly. High resolution shadowgraphy and polarimetry allow for the investigation of the interaction itself and will be discussed in more detail. In combination with the spectral analysis of electromagnetic radiation scattered and emitted from the region of interaction, an extensive set of data is available for the analysis of the laser wakefield acceleration experiments.

3.1 General Setup

A laser pulse focused into a helium gas jet was used to generate a plasma and a plasma wave in which electrons were accelerated to velocities close to the speed of light. The electron energy was measured with an electron spectrometer and the electron beam's transverse profile with an electron beam monitor. Furthermore, the interaction inside the plasma was investigated with two optical diagnostics – an ultrashort probe pulse in combination with a high resolution imaging system in sideview and an imaging spectrometer in top view.

Fig. 3.1 shows the basic setup of the experiments where an off-axis parabolic mirror (yellow) focuses the main pulse (light red) into a supersonic helium gas jet generated by a pulsed gas nozzle (brown). During the interaction of the laser pulse and the underdense

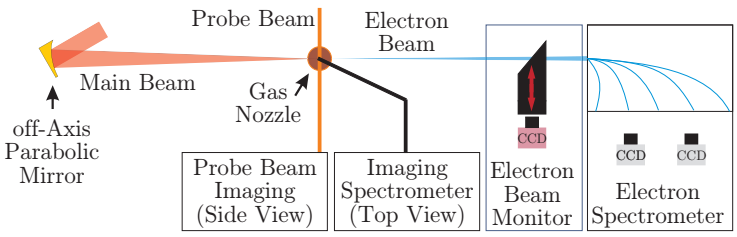

Figure 3.1 *Setup of the laser wakefield acceleration experiments at the* JETI*40-laser system.*

plasma generated from the gas jet through ionisation, electrons (blue) are accelerated to relativistic velocities. Although they are represented by continuous lines in the drawing, the main beam, the probe beam as well as the electron beam are pulsed in the experiment.

An electron beam monitor and a magnetic electron spectrometer were employed to determine the transverse beam profile and the electron density of the accelerated electron

bunch with respect to the electron energy E and the angle of divergence D. As the measurement of the electron energy depends on the electrons' trajectories, which are affected when the electrons pass the beam monitor setup, high-resolution electron density maps of the accelerated electron bunch resolved with respect to the electron energy and the angle of divergence could only be recorded when the beam monitor was removed from the electrons' path, i.e., the electron detectors cannot be used at the same time.

Additionally, the region of interaction in the plasma was observed with two optical diagnostics. The probe beam (orange) propagates through the gas jet from the side – transverse to the direction of main beam propagation. In combination with the high resolution imaging system, shadowgraphy and polarimetry measurements were performed. In top view (cf. Fig. 3.1), the interaction region was imaged onto the entrance slit of an imaging spectrometer, which was used to spectrally analyse radiation emitted along the whole interaction length. Since the electron oscillations excited by the electric and magnetic fields of the laser pulse lie in the plane, which is defined by the propagation axes of main and probe pulse, the radiation emitted by the electrons acting as a dipole antenna is suppressed in their direction of oscillation and has its maximum intensity in the transverse direction, in this case into the direction of the top-view diagnostic. This is advantageous for both diagnostics – probe beam and imaging spectrometer – as scattering of laser light is suppressed in side view while in top view, the majority of the scattered pump light can be detected.

3.2 Experimental Campaigns

Within the frame of this thesis, results of two experimental campaigns are discussed. The campaigns are characterised by different focusing geometries and gas nozzles with different opening diameters.

The measurements discussed in Chapters 4 and 5 were obtained in two experimental campaigns where a combination of different gas nozzles with different opening diameters d_{out} and focusing geometries was used. Here, the focusing geometry is characterised by the $f_{\#}$-number which is given as the ratio of the initial $1/e^2$ beam diameter d_e and the focal length f of the respective parabolic mirror. In both campaigns, which are referred to as Campaign 1 and Campaign 2 in the following chapters, experiments on the controlled injection of electrons were carried out. Furthermore, polarimetry measurements using few-cycle probe pulses for the investigation of the magnetic fields present during laser wakefield acceleration were performed in Campaign 2.

3.2.1 Laser Parameters

While in Campaign 1 vacuum peak laser intensities of $I_V \approx (1.6 \pm 0.4)10^{18}$ ***W/cm***^{2} ***were achieved with an*** $f/20$***-off-axis parabolic mirror, vacuum peak laser intensities of*** $I_V \approx (5.3 \pm$

1.5)10^{18} ***W/cm^2 were reached with an $f/13$-off-axis parabolic mirror in Campaign 2.***

The Laser pulses from the titanium-sapphire JETI40-laser system with a central wavelength of $\lambda_0 \approx 800\,\mathrm{nm}$ were focused to vacuum intensities of $I_V \approx 1.6 \times 10^{18}\,\mathrm{W/cm^2}$ in Campaign 1 and $I_V \approx 4.1 \times 10^{18}\,\mathrm{W/cm^2}$ in Campaign 2. Note that the uncertainties of the underlying quantities – pulse duration τ_L, laser energy E_L, focal spot size A_L and q-factor – differ drastically. While for the pulse duration, which could not be measured online during the experiments, only the typical system parameter $\tau_L \approx (30 \pm 3)\,\mathrm{fs}$ was available, the laser energy was logged for every laser shot and the average could be calculated from more than 1000 single measurements for any given day. Due to a laser maintenance in between the campaigns, E_L was increased and slightly stabilised from $\approx (0.75 \pm 0,03)\,\mathrm{J}$ in Campaign 1 to $\approx (0.80 \pm 0,03)\,\mathrm{J}$ in Campaign 2. Typical focal spots achieved with the different focusing

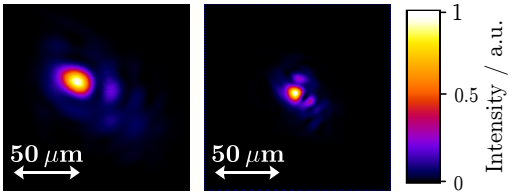

Figure 3.2 *Typical focal spots of the (a) $f/20$ and (b) $f/13$ off-axis parabolic mirrors.*

geometries – $f/20\,(f = 1024\,\mathrm{mm})$ in Campaign 1 and $f/13\,(f = 635\,\mathrm{mm})$ in Campaign 2 – are shown in Fig. 3.2. The spot sizes and q-factors presented in Table 3.1 are determined

	Campaign 1 ($f/20$)	Campaign 2 ($f/13$)
E_L / J	$0.75 \pm 0,03$	$0.80 \pm 0,02$
A_L / μm^2, (q_L)	317 ± 16, $(0.31 \pm 0,01)$	91 ± 12, (0.28 ± 0.01)
I_V / $10^{18}\,\mathrm{W/cm^2}$, (a_0)	1.6 ± 0.4, (0.9 ± 0.4)	5.3 ± 1.5, (1.6 ± 0.9)
Δy_p / μm	16	10

Table 3.1 *Laser parameters in the two experimental campaigns.*

from 10 single images of the focal spot recorded several days before the measurements. Additionally, the fluctuation of laser pointing Δy_p in horizontal direction was determined, which is relevant for the side-view imaging (cf. section 3.4). More detailed information on the JETI40-Laser system can be found in Appendix A.1.

3.2.2 Target

In the experiments, supersonic pulsed helium gas jets were generated with the help of conical gas nozzles with opening diameters d_{out} and Mach numbers M. In Campaign 1, a nozzle with $d_{out} = 3.1\,$mm and $M = 4$ was employed whereas in Campaign 2, a nozzle with $d_{out} = 2.1\,$mm and $M = 3.2$ was used.

An underdense plasma as required in LWFA experiments can be generated from gases in a wide density range. Since the gas target is situated in an evacuated chamber, a solenoid

valve (Parker Hannifin Corporation Series 99) was operated in pulsed mode to keep the gas load on the vacuum pumps low. To generate a stable helium gas jet, the valve opening time was set to 4 ms. Attached to the valve, a gas nozzle was used to shape the density profile of the gas jet. Due to their plateau-like density profile in the centre of the jet (cf. Fig. 3.3) as well as their flow characteristics (cf. section 3.2.2.2), supersonic gas jets were employed in the reported experiments. A supersonic gas jet is characterised by a Mach number $M > 1$ with M being the ratio of the average particle velocity to the fluid's speed of sound. To generate supersonic gas jets, nozzles with a gas inlet diameter $d_{in} = 1\,\text{mm}$, a nozzle shaft length $l = 9.6\,\text{mm}$ and different opening diameters d_{out} were used. The Mach numbers of those nozzles – $M = 4$ for a nozzle with $d_{out} = 3.1\,\text{mm}$ used in Campaign 1 and $M = 3.2$ for a nozzle with $d_{out} = 2.1\,\text{mm}$ used in Campaign 2 – were estimated on the basis of a detailed study [97]. To avoid degradation of the nozzle material (here brass) , e.g., ablation caused by the main laser pulse and the generated plasma, the shot height of the main laser pulse was set to $z_L = 1.25\,\text{mm}$ with respect to the nozzle surface at $z = 0$.

3.2.2.1 Normalised Electron Density Profiles and Target Position

The electron density profiles of the fully ionised gas jets exhibit a plateau electron density n_0. The experiments were performed in a plateau density range of $n_0 \approx (0.77...1.31) \times 10^{19}\,\text{cm}^{-3}$.

The gas jets generated by the nozzles introduced above were interferometrically characterised in a tomographic setup by B. Landgraf from the Institute of Optics and Quantum Electronics in Jena [98]. The gas jet was rotated by 180° in 4° steps and at each projection angle, ten interferograms were recoded to average over shot-to-shot fluctuations, which amount to $1 - 10\,\%$ of the average density. The retrieval of the neutral gas density ρ_{gas} from the interferograms taken at different projection angles does not require symmetry assumptions. Although with this method, the neutral gas density ρ_{gas} is obtained, the result is represented as normalised electron density n_e/n_0 since for a fully ionised gas $n_e \propto \rho_{gas}$. Fig 3.3 shows the normalised electron density profiles $n_e(x)/n_0$ at a height of 1.25 mm above the nozzle as solid lines centred above the supersonic gas nozzle apertures, which are illustrated as grey boxes with dashed lines in the same colour. The structured nature of the averaged plateau is mainly caused by the retrieval algorithm which requires an exact determination of the centre of rotation of the tomography setup. In Fig. 3.3(a), the density distributions from Campaign 1 (Campaign 2) is represented in red (black). The plateau electron density n_0 was investigated during the experiment for a nozzle with $d_{out} = 2.1\,\text{mm}$ and backing pressures p_N between 8 bar and 14 bar (cf. section 4.2.4.2). Since n_0 scales with p_N/d_{out}, those results could be used to determine the plateau densities for a larger nozzle with $d_{out} = 3.1\,\text{mm}$ operated at backing pressures between 20 and 30 bar. All experiments were performed with n_0 in the range of $\approx (0.77...1.30) \times 10^{19}\,\text{cm}^{-3}$.

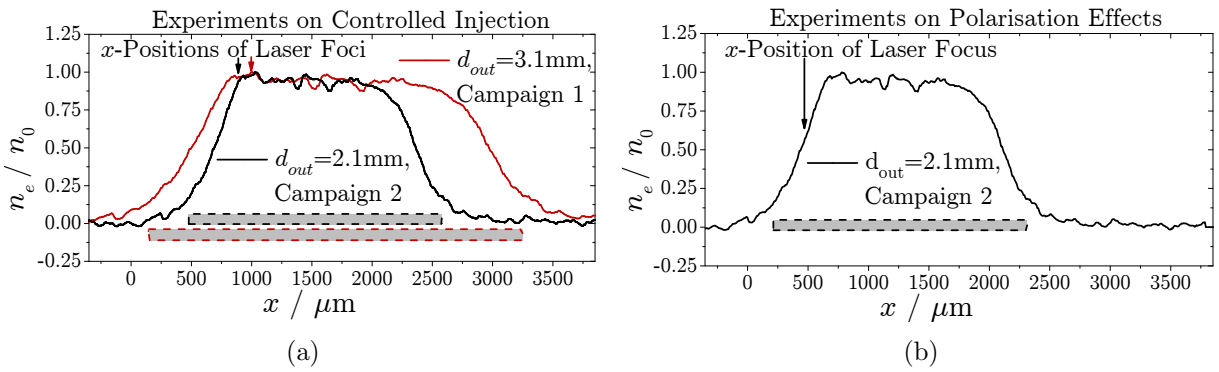

Figure 3.3 *Normalised electron density profiles of the fully ionised supersonic gas jets and relative position of the laser foci.*

The position of the laser focus with respect to each density profile is shown in Fig. 3.3 as arrows in the same colours. Note that in the experiments on controlled injection, the electron density profiles shown in Fig.3.3(a) are manipulated (cf. section 3.2.2.2) and the laser is effectively focused into a rising density profile as in the experiments on polarisation effects.

3.2.2.2 Generation of a Sharp Density Transition

An obstacle brought into the gas flow of a supersonic gas jet generates a shockfront, which at the boundary to the undisturbed part of the gas jet forms an electron density transition. The maximum electron density of the shockfront will be labled as n_{SF}, while the undisturbed density is n_0, i.e., the plateau electron density of the undisturbed gas jet.

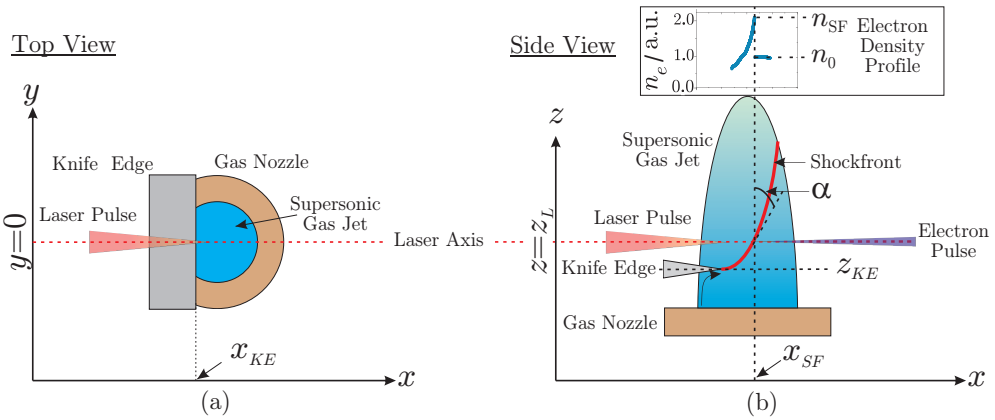

Figure 3.4 *Generation of a density transition by a knife edge brought into a supersonic gas flow in (a) top- and (b) sideview.*

An obstacle positioned inside a supersonic gas jet distorts the initial gas flow. This distortion propagates upstream (here, along the red line in Fig. 3.4(b)) with the fluid's speed of sound and thus, is slower than the individual gas particles. Consider a knife edge at a height z_{KE} above the nozzle blocking a part of the gas jet as shown in Fig. 3.4 in top and in sideview. As indicated by the bent arrow underneath the knife edge in Fig. 3.4(b),

a part of the initial gas stream is redirected and runs into the undisturbed particle flow which causes a wall of increased density – a shockfront penetrating the gas jet starting at the tip of the knife edge with the coordinates (x_{KE}, z_{KE}). The increased density n_{SF} of the shockfront and the undisturbed density after the front n_0 form a density transition with a width w_{SF} depending on the molecular mean free path of the fluid, the Mach number M of the supersonic gas jet and the angle α of the shockfront [47, 99, 100]. The shockfront and its density transition will be characterised in detail in section 4.2. Note that the height of the knife edge is kept at $z_{KE} = 1\,\text{mm}$ in all experiments on controlled injection.

3.3 Electron Beam Characterisation

Scintillating screens sensitive to charged particles are employed to measure the transverse electron beam profile as well as the electron energy for which additionally, a magnet was used.

Electrons impinging on a charge sensitive scintillating screen (here Kodak Biomax MS) trigger the emission of electromagnetic radiation, which when imaged onto a CCD camera reveals the electrons' position of incidence. Since the emitted intensity is proportional to the number of electrons [101], the electron beam's charge and transverse profile can be measured. For electron beam profile measurements, the scintillating screen was brought into the path of the accelerated electron beam at a distance of $\approx 50\,\text{cm}$ from the gas jet. Since the scintillator material is also sensitive to electromagnetic radiation, the laser light was blocked by an aluminium cover with a thickness of $\approx 45\,\mu\text{m}$. Nevertheless, scattering effects of the electrons inside the material are negligible due to the proximity of the screen to the aluminium cover. To protect the camera (Allied Vision Pike F-421) from direct electron irradiation, the scintillating screen was tilted by an angle of 45° with respect to the electron beam path and was imaged onto the camera from the side at an angle of 45° by an $f/1.4,\ f = 25\,\text{mm}$ objective. The deformation of the image caused by the imaging geometry is rectified by locally adapted stretching of the image.

For the measurement of the electron energy, the energy dependent deflection of electrons in a magnetic field is utilised. Electrons entering the magnetic field inside the spectrometer are deflected towards the scintillating screen, which is imaged onto two CCD cameras (Basler A102f) using two $f/1.4,\ f = 25\,\text{mm}$ objectives. Since the emission characteristics of the scintillating screen was investigated by [101], the intensity of the emitted radiation could be calibrated to obtain the electron charge. Therefore, the sensitivity of the imaging system as well as its aberrations were taken into account [52]. Electron energies in the range of 3 to 1050 MeV could be detected with a resolution depending on the width of the 20 mm thick variable copper aperture at the entrance of the spectrometer. In the reported experiment, the entrance slit was set to 1 cm and was positioned 100 cm away from the gas jet

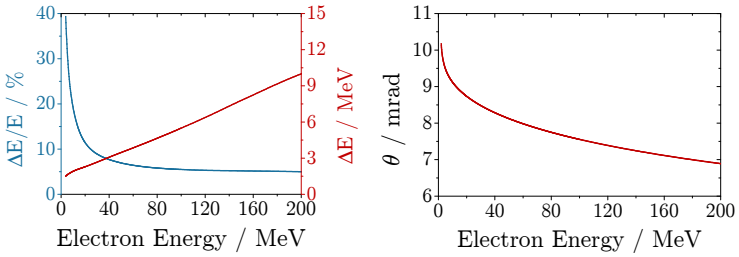

(a) (b)

Figure 3.5 *(a) Absolute and relative resolution of the electron spectrometer and (b) half angle of acceptance θ in divergence direction in the reported setup.*

corresponding to a half opening angle of $\approx 5\,\mathrm{mrad}$. The corresponding absolute (ΔE) and relative ($\Delta E/E$) resolution in the experimentally relevant range of (3...200) MeV are plotted in Fig. 3.5(a). Furthermore, transverse to the direction of dispersion, the scintillating screen extends to $\pm 1\,\mathrm{cm}$ which determines the half angle of acceptance θ (cf. Fig. 3.5(b)) in the vertical direction. Since in vertical direction, the magnetic field strength between the two magnetic poles might vary, the electron pulses might be focused in divergence direction, i.e., a deviation of the assumed path of the electrons through the spectrometer can influence the angularly resolved electron density maps of the accelerated electron bunch and hence, the interpretation of the data.

3.4 Snapshots of the Laser Plasma Interaction

An ultrashort probe pulse is generated from a fraction of the main laser pulse and can be used to observe the interaction inside the plasma with the help of a high resolution imaging system in sideview.

Backlighting the interaction region with a synchronised probe beam, the interaction of the main beam and plasma can be observed. Therefore, a fraction of the main laser pulse is split off at a beam splitter (cf. Fig 3.6). The probe pulse is then temporally

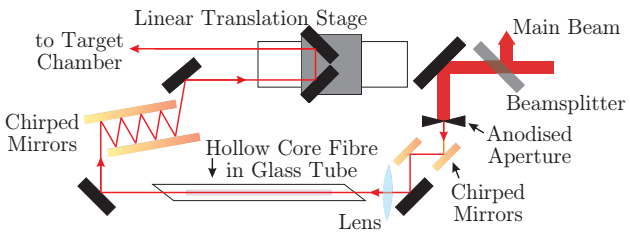

Figure 3.6 *Basic setup of the probe beam. After the spectral broadening of the probe beam in an argon filled hollow core fibre, it is temporally compressed by chirped mirrors. With a linear translation stage, shadowgrams can be taken within a 2-ns time interval with a smallest delay of 33 fs.*

recompressed and focused into a hollow-core fibre filled with argon where its spectrum is broadened through self phase modulation (cf. section 2.2.3). Subsequently, the probe pulse is recompressed again by a further set of chirped mirrors. While pulse durations of $\approx 4\,\mathrm{fs}$ are possible with this setup [102], in the experiments reported here, $\tau_{probe} \leq 10\,\mathrm{fs}$ was achieved. With a linear translation stage, the temporal overlap of the probe and the main pulse inside the target can be varied within a temporal window of $t_w = 2\,\mathrm{ns}$ with a minimum step size

of 33 fs.

After the propagation of the probe pulse through the region of interaction, scattered probe light is imaged with an infinity corrected microscope objective (Mitutoyo M Plan Apo NIR, (10x)) and an achromatic lens ($f = 25\,\text{cm}$, $d \approx 5\,\text{cm}$) onto a CCD camera (Basler piA1900-32gm). The imaging system is depicted in Fig. 3.7. The sharpness of the images can vary from shot to shot because the object plane is fixed by the imaging optics, but the location of the laser-plasma interaction is dependent on the main laser's pointing stability (cf. section 3.2.1).

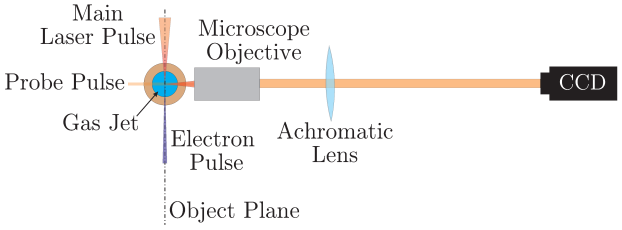

Figure 3.7 *A combination of a microscope objective and an achromatic lens is used to image the region of interaction onto a CCD camera.*

While the optical resolution of the imaging system is defined by the microscope objective (manufacturer's specifications: $1.5\,\mu\text{m}$ [103]), the magnification depends on the focal lengths of both optical elements. Following the sampling theorem independently developed by several scientists, e.g. [104], the sampling frequency must be at least twice the frequency of the object – e.g. the plasma wave – to be sampled correctly. Accordingly, with a resolution of $\approx 0.61\,\mu\text{m/px}$, the effective resolution is $\approx 1.22\,\mu\text{m/px}$ which is comparable to the optical resolution.

3.4.1 Shadowgraphy and Plasma Wave Imaging.

A plasma wave with a wavelength λ_p can be imaged when the probe pulse duration is $\tau_{probe} < \lambda_p/c$ and the resolution of the imaging system is $\Delta x_{res} < \lambda_p$.

Probe light propagating through an inhomogeneous electron density distribution is deflected towards regions of lower densities resulting in a modulated intensity profile, which can be detected by their imaging onto a CCD camera. If deflections are solely acquired in the focal plane of the imaging system, no modulation of the intensity profile would be detected since in this case, the imaging system directs the probe light deflected at a distinct point in the image plane to the corresponding point in the object plane. Nevertheless, due to the transverse extent of the plasma wave of $\approx \lambda_p$, intensity modulations are not exclusively generated in the object plane and the electron density distribution of the plasma wave can be visualised with this technique, which is referred to as **shadowgraphy**.

The imprint of the plasma wave on the probe pulse is affected by the pulse duration τ_{probe} of the probe beam, the longitudinal density modulation of the plasma wave with a period λ_p, the transverse extend of the plasma wave $\approx \lambda_p$ and finally, the simultaneous propagation of

probe pulse and plasma wave under 90°. Let us first consider an infinitely short probe pulse. Its propagation through the moving structure results in a deformed image of the plasma wave. Nevertheless, this image is mainly generated by the centre of the plasma wave [105] as larger density modulations cause stronger brightness modulations. Therefore, a slightly blurred image of the centre of the plasma wave would be obtained. For the discussion of the role of the pulse duration, it is convenient to limit the transverse extent of the plasma wave to its centre. With increasing pulse duration τ_{probe}, the probe beam experiences the movement of the plasma wave's centre resulting in a weakening of the intensity modulation. A probe beam long enough to witness the propagation of the central part of the wave by λ_p will experience the averaging out of the signals imprinted on the probe pulse by the high and low density regions of the plasma wave. Hence, to temporally resolve the plasma wave $\tau_{probe} < \lambda_p/c$ is required. Moreover, to detect the intensity modulation introduced by the plasma wave, an imaging system with a spatial resolution $\Delta x_{res} < \lambda_p$ is also required.

3.4.1.1 Plasma Wavelength Measurements

Intensity inhomogeneities in shadowgrams can be removed with a low order spline fit resulting in a contrast enhanced image. Moreover, an image of the plasma wave can be analysed using continuous wavelet transformation, which yields the plasma wavelength.

An example shadowgram visualising a plasma wave is shown in Fig. 3.8(a). The intensity inhomogeneities in the beam's near-field profile, which are a combination of the initial probe beam profile and intensity modulations acquired in an inhomogeneous plasma, can be estimated and removed (cf. Fig. 3.8(c)) with a low order spline fit [106] when the spatial frequency of those inhomogeneities is significantly smaller than the plasma wavelength. Fig. 3.8(b) exemplarily shows the central lineout of the plasma wave (black line) as well as the corresponding low order spline fit (red line). Removing the fitted curve from the original lineout yields the clear oscillation of the plasma wave (blue line). Applied to the whole image line by line, the visibility of the plasma wave is significantly enhanced (Fig. 3.8(c)). The central lineout of the plasma wave, corrected with the fitted line, can now be analysed using the continuous wavelet transformation (CWT) [107] method which compares the amplitudes at all positions x in the lineout with each other to find the local spatial frequency. Fig. 3.8(d) shows the result for the lineout in Fig. 3.8(b) in terms of the plasma wavelength where the bright region corresponds to the most frequently occurring wavelengths at the corresponding positions x. The average plasma wavelength at each position x is emphasised with a dashed black line. Note that further features, e.g., radiation emitted from the region of interaction or an image of the shockfront are observable in shadowgrams and will be discussed in Chapter 4.

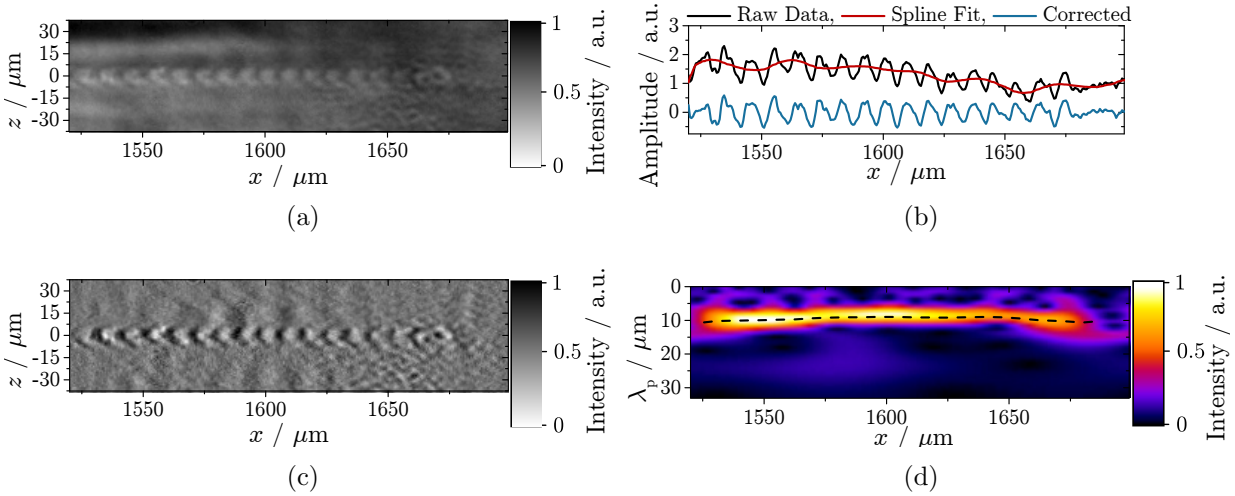

Figure 3.8 *(a) Shadowgram (normalised raw image). (b) Central lineout of the plasma wave (black), low order spline fit to remove brightness inhomogeneities of the probe beam (red) and corrected plasma wave lineout (blue). (c) Contrast enhanced shadowgram. (d) Plasma wavelength analysis with continuous wavelet transformation.*

3.4.2 Polarimetry

For polarimetry measurements, the probe beam imaging system introduced in section 3.4 is modified by adding a non-polarising beam splitter, a second camera and two polarizers.

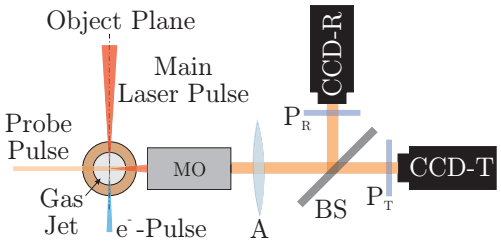

Figure 3.9 *Polarimetry setup. A nonpolarising beam splitter is used to separate the probe beam into a transmitted (T) and a reflected (R) part. The CCD cameras (CCD-T and CCD-R) are equipped with a polarizer (P_T and P_R) each.*

As explained in section 3.4, the region of interaction is imaged with a microscope objective (MO) and an achromatic lens (A) onto a CCD camera (cf. Fig. 3.9). CCD-T is equipped with a polarizer (P_T) to determine the state of polarisation of the probe beam after its propagation through the region of interaction. Those shadowgrams modified by a polarizer will be referred to as polarograms in the following discussion. With only one camera and polarizer set to an angle ψ_T, the analysis of the images requires the assumption of either symmetry of the polarograms with respect to the laser axis or comparability of consecutive shots [108]. Therefore, the probe beam is split by a non-polarising beam splitter (BS) to allow for the observation of the same region inside the plasma with a second camera and polarizer set to an angle $\psi_R \neq \psi_T$. The advantage of using this two camera setup [56] will become more obvious in section 3.4.2.1 where the analysis of the polarograms is explained.

3.4.2.1 Polarograms and Rotation of the Polarisation Ellipse

From the polarograms obtained with the modified probe beam imaging system, the change of polarisation of the probe beam acquired inside the plasma can be retrieved.

The intensity of a fully polarised electromagnetic wave transmitted through a polarizer can be described by means of the Jones calculus (cf. Appendix C.1). Generally, the intensity after the polarizer

$$I_T(x,z) = I_0(x,z)T\left[1-\beta_T\left|1-\left\{e^{i\delta(x,z)}\cos\left[\psi_T\right]\cos\left[\psi(x,z)\right]+\sin\left[\psi_T\right]\sin\left[\psi(x,z)\right]\right\}^2\right|\right], \quad (3.1)$$

depends on the angle of the polarizer ψ_T and the local angle of Faraday rotation $\psi(x,z)$ – both with respect to the probe beams's initial direction of polarisation ($\vec{e}_x$) – as well as the local phase shift $\delta(x,z)$ between the wave's electric field components. Eq. (3.1) is adapted to the transmission arm introduced above. To yield the result for the reflection arm $I_R(x,z)$, the transmittance T is interchanged with the reflectance R of the beamsplitter. The ratio $T/R \approx 1.1$ will be relevant for the analysis of the data and was determined in the experiment. Moreover, the extinction coefficients of the polarizers in the transmission and reflection arm could be determined to $\beta_T \approx \beta_R \approx 0.99$ (cf. Appendix C.2). $I_0(x,z)$ is the local brightness of the probe beam of the polarograms in Fig. 3.10, which is given by

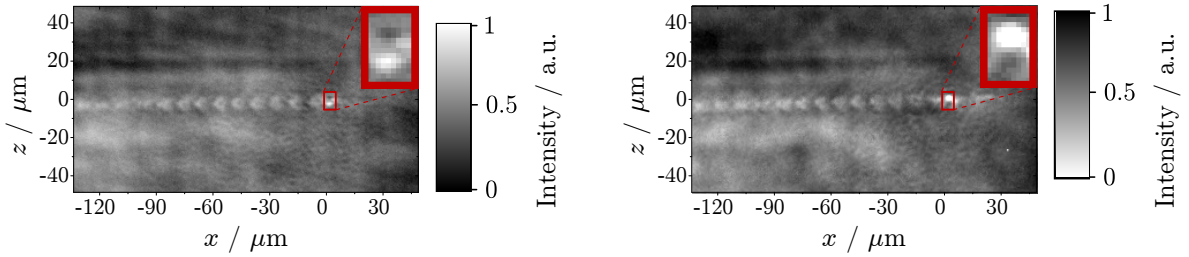

Figure 3.10 *Polarogams of (a) transmission and (b) reflection arm. The bright and dark spots caused by changes of the probe beam's state of polarisation (inside red square) are interchanged whereas the initial brightness modulations are similar.*

the initial probe beam's intensity profile as well as brightness modulations acquired inside the plasma which can for example be induced by the density gradients of the plasma wave (cf. section 3.4.1). $I_0(x,z)$ is not affected by changes of the state of polarisation of the probe beam and is therefore, similar in both images. Assuming $\delta(x) = 0$, Eq. (3.1) can be simplified to $I_T(x,z) = I_0(x,z)T\big(1-\beta_T\sin^2\left[\psi_T-\psi\right]\big)$ and the quotient

$$\frac{I_T(x,z)}{I_R(x,z)} = \frac{T}{R}\,\frac{1-\beta_T\sin^2\left[\psi_T-\psi\right]}{1-\beta_R\sin^2\left[\psi_R-\psi\right]}, \quad (3.2)$$

can be numerically inverted to retrieve ψ, which in this context represents the rotation of the polarisation ellipse (cf. section 2.3.6). Therefore, the retrieved angle will be referred to as $\vartheta_{\psi,\delta}$ in the following sections whereas ψ is still the angle of rotation of the plane of polarisation.

In contrast to $I_0(x, z)$, regions of changed polarisation as present inside the red boxes in Fig. 3.10 are interchanged. Therefore, the division of the images removes the background brightness while the brightness modulation due to changes of polarisation is maintained such that regions of changed polarisation can be identified clearly. The interchange of bright and dark regions in the polarograms is due to the choice of the polarizers' angles $\psi_T \approx 90.0° - 15.0° = 75.0°$ and $\psi_R \approx 90.0° + 18.6° = 108.6°$ where $\psi_T = \psi_R = 90°$ refers to maximum extinction of the probe light with initial polarisation. Since the polarizers are rotated away from maximum extinction by approximately the same angle but in opposite directions, a given angle of rotation ψ results in the opposite change of brightness in the two images.

The sensitivity of the measurement can be optimised by minimising or maximising the intensity ratio, which for $\beta_T = \beta_R \to 1$ is achieved when the polarizers are detuned from maximum extinction by the maximum of ψ. Since the maximum angle of rotation is small ($\approx 2°$), the part of the probe beam with initial state of polarisation would be blocked almost completely, which leads to plasma imaging with poor contrast. Therefore, the chosen angles are a compromise between the sensitivity of the polarisation measurement and the imaging of the plasma wave, which is ideal at full transmission of the initial state of polarisation.

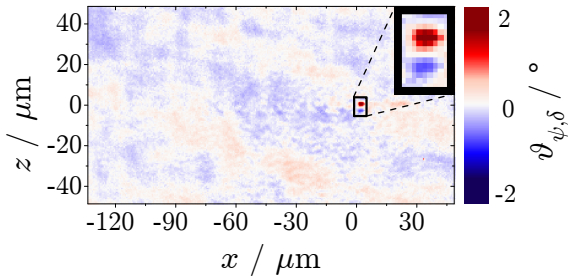

Figure 3.11 *Rotation map retrieved from the polarograms in Fig. 3.10.*

Fig. 3.11 shows the rotation map $\vartheta_{\psi,\delta}(x, z)$ retrieved from the polarograms in Fig. 3.11 which will be referred to as polarisation signal in the following sections. The intense red and blue spots correspond to regions of positive and negative rotation.

3.5 Spectral Analysis of Scattered Radiation

With an imaging spectrometer, electromagnetic radiation scattered and emitted from the region of interaction can be analysed spectrally in top view.

During the interaction of main laser pulse and plasma, electromagnetic radiation is emitted or scattered away from the region of interaction. Different kinds of radiation can

be distinguished by their spectrum and region of origin; therefore, an imaging spectrometer was employed. To generate spatially resolved optical spectra, the channel of interaction was imaged onto the entrance slit of the spectrometer using an achromatic lens ($d \approx 5\,\mathrm{cm}$, $f = 25\,\mathrm{cm}$), which in turn was imaged onto a CCD camera (SXVF-H35) by two spherical mirrors with a magnification of 1. A reflective diffraction grating was positioned in between the two spherical mirrors fixed on a rotational mount in order to switch between the different orders of diffraction, i.e., the region of interaction can be observed in (x, y)-space using the zero-order reflection, or (x, λ)-space using the first-order of diffraction. Due to the large sensor of the CCD camera with 4008×2672 pixels with a pixel size of $(9\,\mu\mathrm{m})^2$, the whole interaction length of 2-3 mm can be observed with a resolution limited by the optics. In the spatial direction, the resolution of $\approx 5\,\mu\mathrm{m/px}$ is determined by the imaging lens. The spectral resolution depends on the width of the slit and the line spacing of the grating and was measured to be $\approx 5\,\mathrm{nm/px}$ using the FWHM width of the spectral lines of a mercury-vapour lamp used for calibration.

4. Controlled Injection of Electrons into Plasma Waves

Self injection of electrons into the plasma wave usually requires the evolution of laser pulse and plasma wave to higher amplitudes. Due to the nonlinear nature of the laser-plasma interaction, slight changes in the initial conditions (fluctuations of laser and target properties) may lead to uncontrollable fluctuations of the accelerator output. Especially, differences in the position of injection result in a variation of the final electron energy. Controlled injection – here at a density transition – is a possibility to stabilise and control the electron energy gain by triggering injection at a defined position.

The density transition is situated between a shockfront and the following undisturbed electron density of an ionised helium gas jet. The shockfront is generated by inserting a horizontally oriented knife edge at variable position into the upward-directed gas flow, which influences the position, angle and the electron density profile of the shockfront. In this chapter, the shockfront or density transition is characterised in detail with the help of an ultrashort probe beam with its imaging system as well as an imaging spectrometer. Using these diagnaostics, information on the manipulated electron density profile of the ionised gas jet could be deduced. Subsequently, the influence of the shockfront on the acceleration process is investigated at different positions in the gas jet and for different nozzle backing pressures. This includes the emission of wavebreaking radiation at the shockfront, the electron energy gain as well as the electrons' spectral bandwidth and shape. Moreover, the influence on the transverse electron beam profile which helps to investigate the charge, divergence and pointing of the accelerated electron beam is presented in Appendix B.3. It was found that all those parameters are influenced by the properties of the shockfront.

4.1 Comparability of the Results

Despite different nozzles and focusing optics used in the different experimental campaigns, the results are expected to be comparable.

In the following sections, results from two experimental campaigns are presented where different combinations of focusing optics and gas nozzles were employed (cf. Table 4.1 and section 3.2). Despite the difference in particular laser and target parameters in the two campaigns, a number of parameters were similar, which had a significant effect on the outcome of the experiment. The comparability of the results of the two campaigns is based

Table 4.1 *Focusing geometry and nozzle diameters of the two experimental campaigns presented in this chapter (cf. section 3.2).*

	Campaign 1	Campaign 2
$f_{\#}$	$f/20$	$f/13$
d_{out} / mm	3.1	2.1

on comparable relations of the shockfront position x_{SF} and angle α to the position of the knife x_{KE}, (cf. section 4.2.2), a negligible influence of the Mach number M (cf. section 4.2.2), and comparable electron densities in the undisturbed region after the shockfront n_0, (cf. section 4.2.4.2).

4.2 Characterisation of the Shockfront

An ideal electron density profile of a shockfront has a rising electron density profile in front of the electron density transition (region I), which is located at x_{SF}***. The electron density profile at*** $x > x_{SF}$ ***(region II) is undisturbed.***

As explained in section 3.2.2.2, an obstacle – here a knife edge – brought into a supersonic gas jet generates a wall of increased density and thus, a density transition towards the following undisturbed region of the gas jet. The position of the knife edge x_{KE} determines the position of the density transition x_{SF}, which in turn affects the electron density profile $n_e(x)$. Fig. 4.1 shows an idealised density profile (cf. section 4.2.4.4) of a gas jet with a shockfront where the density rises for $x < x_{SF}$ in region I and forms a plateau with $n_e = n_0$ in the undisturbed part of the gas jet for $x > x_{SF}$ in region II. The density transition from $n_e = n_{SF}$ to $n_e = n_0$ at $x = x_{SF}$ is a sharp density gradient with a width of few micrometers (cf. section 4.2.2). Strictly speaking, x_{SF} refers to the centre of the density transition between the increased density of the shockfront and the undisturbed density behind the shockfront. Nevertheless, x_{SF} is referred to as position of the shockfront in this chapter.

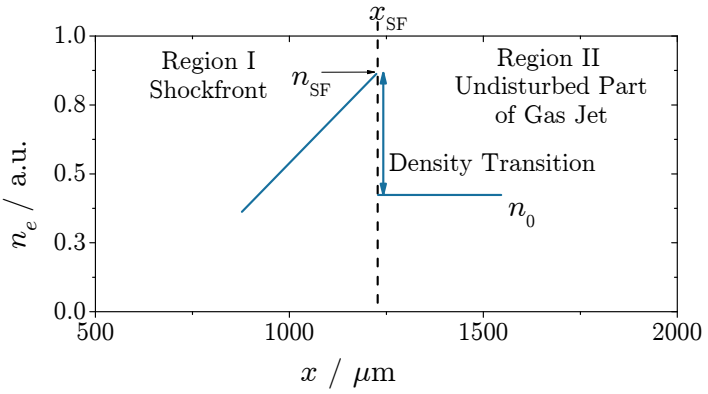

Figure 4.1 *Idealised electron density profile of a shockfront.*

Here, the shockfront is characterised in dependence on x_{KE} and different nozzle backing pressures p_N which could be related to the electron density n_0 of the density plateau in the undisturbed region of the gas jet behind the shockfront. The following section covers the dependence of position x_{SF}, angle α and width w_{SF} of the shockfront on the position of the

knife edge x_{KE}. Subsequently, different aspects of the electron density profile are analysed in detail with respect to the position of the shockfront x_{SF}.

4.2.1 Position Calibrations

Through the observation of the shockfront with both optical diagnostics, a shared point of origin was found.

In the present experiment, two optical diagnostics were available for the observation of the interaction of laser and plasma. With the imaging spectrometer operated in zero-order reflection (imaging mode), the position of the knife edge x_{KE} could be determined (Fig. 4.2(a)) with respect to the gas nozzle and thus, to the undisturbed electron density profiles of the gas jets introduced in section 3.2.2.1.

In side view, shadowgrams as shown in Fig. 4.2(b) were recorded with the ultrashort probe beam. Here, the area ionised by the main laser pulse (inside red line) is intersected by a tilted straight pattern, which is generated at the increased electron density of a shockfront (SF). The angle α of the shockfront is defined with respect to the normal to the laser axis, i.e., the path of the peak of the main laser pulse, which can be identified by the plasma wave (PW) or the channel of scattered radiation. Moreover, the intersection of the shockfront with the laser axis determines the position of the shockfront x_{SF}. It will be shown in section 4.2.3.2 that the position of the shockfront can be detected with the imaging spectrometer operated in first order of diffraction (spectral mode) allowing to define a shared point of origin (cf. section 4.2.2) for both optical diagnostics in laser propagation direction $\vec{e}_x$.

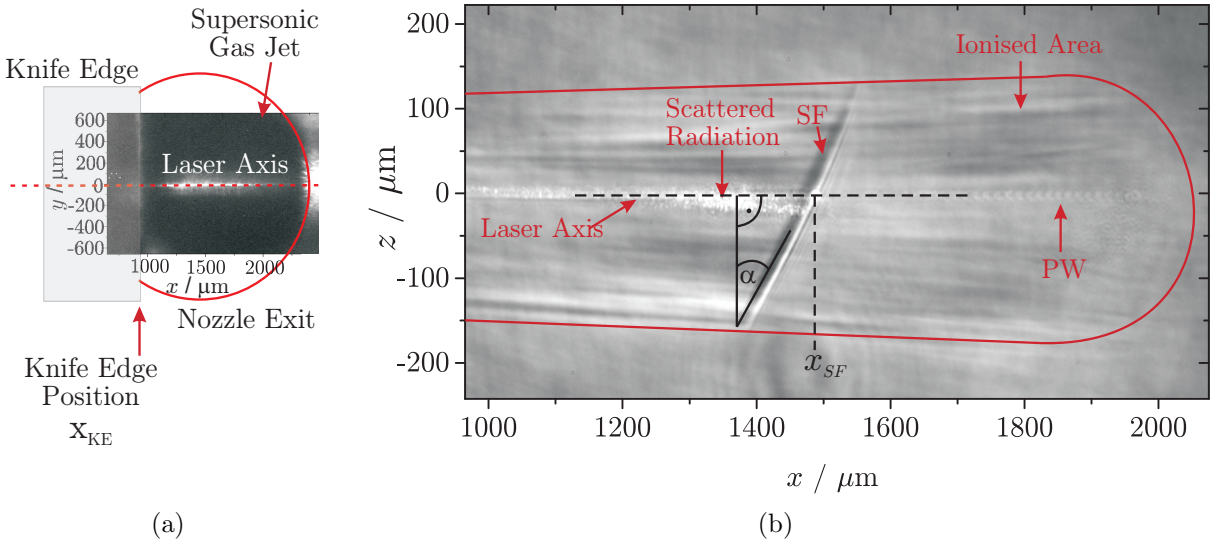

Figure 4.2 *(a) Nozzle and knife edge in top view. (b) Interaction in Sideview. The shadowgram shows a plasma wave, the tilted straight pattern of a shockfront and side scattered radiation.*

4.2.2 Position, Angle and Width of the Shockfront

Both, shockfront position x_{SF} and angle α linearly depend on the position of the knife edge x_{KE} while a dependence of x_{SF} and α on the nozzle backing pressure p_N, the nozzle opening diameter d_{out} or Mach number M was not found. The width of the transition w_{SF} is $\approx 8\,\mu$m.

The relation of the position x_{SF} and the angle α of the shockfront as a function of the position of the knife edge x_{KE} was investigated for both nozzles with similar results. Here, the results for the larger nozzle with $d_{out} = 3.1\,$mm and $M \approx 4$ operated at different backing pressures ($p_N = 20$, 24 and 27 bar) are presented since data in an extensive x-range are available. While it is possible that the found relations do not depend on the Mach number, a more likely explanation could be that the actual Mach numbers of the two different nozzles' differ less than expected from the nozzle geometry.

Position and angle. As shown in Fig. 4.3(a), the shockfront position x_{SF} as a function of x_{KE} can be described by a line with a slope of ≈ 2, which is caused by the increasing shockfront angle $\alpha \approx 128° \arctan\left[x_{KE}/(3600\,\mu\text{m})\right]$ (Fig. 4.3(b)). An increase of α with x_{KE} has already been observed in numerical flow simulations [109] and is most likely the result of a larger overlap of the knife edge with the nozzle, which causes a larger part of the gas jet to be disturbed and consequently, leads to a redirection of a larger amount of gas particles. Moreover, the increasing overlap and hence, the higher force on the knife edge likely causes stronger deformations of the knife edge itself and therefore, might cause the increasing mean deviation of x_{SF} and α for positions deeper inside the gas jet. While for $x_{KE} \approx 220\,\mu$m, the mean deviation of x_{SF} from its average amounts to $\approx 50\,\mu$m, at $x_{KE} \approx 1270\,\mu$m, the deviation is increased to $\approx 250\,\mu$m. Note that neither a dependence

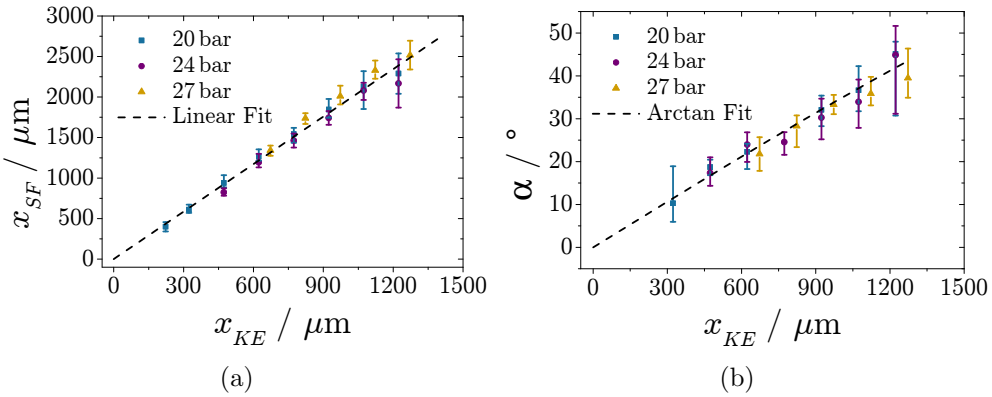

Figure 4.3 *(a) Average position x_{SF} and (b) average tilt α of the shockfront with respect to the position of the knife edge x_{KE}.*

of x_{SF} nor of α on the nozzle backing pressure p_N was found. The origin of the x-axis was chosen such that the extrapolation of $\alpha(x_{KE}) \to 0$ yields $x_{KE} \to 0$, which simultaneously gives $x_{SF}(x_{KE} = 0) \approx 0$. Throughout the whole chapter, $x_{SF} \approx 2x_{KE} > 0$ refers to the calibrated positions of knife edge and shockfront whereas $x_{SF} = x_{KE} = 0$ corresponds

to measurements without knife edge (reference measurements), respectively. As shown in section 3.2.2.1, the position $x = 0$ and thus, $x_{SF} = x_{KE} = 0$ is located at the beginning of the rising electron density profile of the ionised gas jet.

Width. The shockfront is a sudden density drop, which in transverse direction is extended over the whole gas jet. In the ionised area of the gas jet, i.e., in the plasma, the difference in electron density directly before and after the drop generates a difference in the index of refraction of the plasma where the probe light is bent. Since the plasma radially extends over $\approx 100\,\mu$m (cf. Fig. 4.2(b)) and the depth of focus of the probe beam imaging system is $\approx 1.5\,\mu$m, different regions of the shockfront along the probe pulse's path through the plasma are imaged with different sharpness. Therefore, the shockfront is visible as a tilted straight pattern consisting of several dark and bright lines in sideview. Fig. 4.4(a) shows a detail of the shadowgram in Fig. 4.2(b) with shockfront. For the estimation of the width of the shockfront w_{SF}, the FWHM width of the brightest line was measured, which represents the probe light bent away from the region of high density. The procedure is shown exemplarily for the lineout in Fig. 4.4(b) taken from the shadowgram in Fig. 4.4(a) at the position of the horizontal dashed red line. While here, $w_{SF} \approx 6\,\mu$m, on average, $w_{SF} \approx (8 \pm 2)\mu$m. Although this is only a rough estimate, it represents the uncertainty of the determination of a given shockfront position x_{SF}. An estimate of the uncertainty of a single shockfront angle α can also be determined from the alternating pattern of the image of the shockfront. The two solid red lines in Fig.4.4(a) represent the maximum and the minimum angle incorporating the width of a dark stripe of the shockfront pattern. Here, the uncertainty of the determination of the angle of the shockfront amounts to $\approx 3°$.

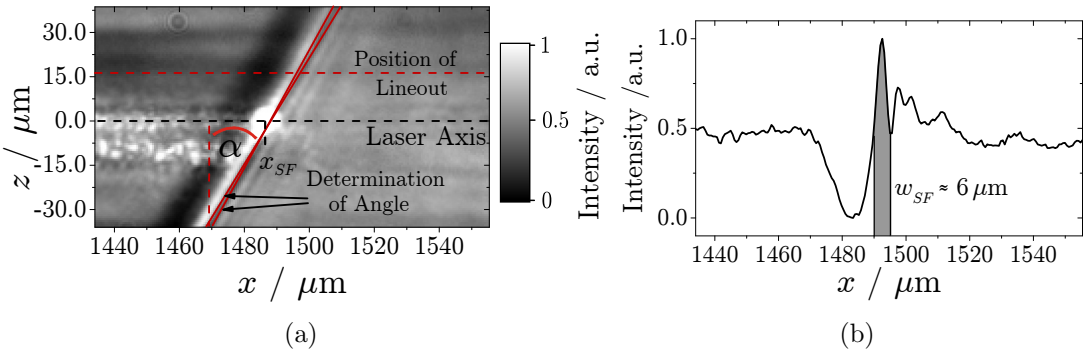

Figure 4.4 *(a) Image of a shockfront in sideview. (b) Lineout along the horizontal red dashed line in (a) for the determination of the width w_{SF} of the shockfront.*

A theoretical estimation of the effective width $w_{SF,eff}$ is based on the assumption that the absolute width of the shockfront w_{SF} at a given temperature is constant and determined by the Mach number M and the mean free path of the fluid l_{mfp} [100]. In helium at $300\,K$, $w_{SF}(M = 3.2) = 2.5\,l_{mpf}$ and $w_{SF}(M = 4) = 2\,l_{mpf}$ [100]. Furthermore, the mean free path

is given by $l_{mfp}\, n_e = constant$ [99] and $l_{mfp} \approx 0.6\,\mu$m at an electron density of $1.9 \times 10^{19}\,\mathrm{cm}^{-3}$ [47]. As the shockfront is tilted by α, the effective width $w_{SF,eff}$ as experienced by the laser pulse is increased leading to a simple relation given by $w_{SF,eff} = w_{SF}/\cos(\alpha)$. In an electron density range of $n_0 \approx (0.77...1.30) \times 10^{19}\mathrm{cm}^{-3}$ where n_0 refers to the undisturbed density of the ionised gas jet and an angle range of $\alpha \approx (10...60)^\circ$, widths between $4\,\mu$m and $12\,\mu$m are obtained, which is in good agreement with the experimentally determined value of $\approx 8\mu$m.

4.2.3 Plasma Parameter and Electron Density Retrieval

Through the measurement of the nonlinear plasma wavelength or frequency, respectively, n_e/γ can be retrieved. In the linear limit, $\gamma \to 1$ and the pure electron density can be deduced.

In this experiment, the electron density n_e could be deduced by means of the plasma wave imaged with the ultrashort probe beam and its imaging system (cf. section 3.4) and from Raman scattered laser light detected with an imaging spectrometer. In both cases, the retrieval of the electron density relies on the measurement of the plasma wavelength or plasma frequency, respectively. Since the plasma wave electrons are excited to oscillate with maximum velocities close to c by the strong pump laser pulse, the relativistic mass increase of the electrons, which can be described by the electrons' γ-factor has to be taken into account and generally, the knowledge of γ is required to calculate n_e from the nonlinear plasma wavelength

$$\lambda_{p,nl} = \sqrt{\gamma}\lambda_p = \frac{2\pi c}{\omega_{p,nl}} = 2\pi c\sqrt{\frac{\epsilon_0 \gamma m_e}{n_e e^2}} \propto \sqrt{\frac{\gamma}{n_e}}, \tag{4.1}$$

and the nonlinear plasma frequency

$$\omega_{p,nl} = \sqrt{\frac{n_e e^2}{\epsilon_0 \gamma m_e}} = \frac{1}{\sqrt{\gamma}}\omega_p \propto \sqrt{\frac{n_e}{\gamma}}. \tag{4.2}$$

In the linear limit, $\gamma \to 1$, i.e., $\lambda_{p,nl} \to \lambda_p$ and $\omega_{p,nl} \to \omega_p$. Moreover, for a top hat laser pulse (THP) in one dimension, the nonlinear plasma wavelength is given by $\lambda_{p,nl} \overset{THP}{\approx} \frac{2}{\pi}\frac{a_0^2/2}{\sqrt{(1+a_0^2/2)}}\lambda_p$ (cf. Eq. (2.30)) and thus, the corresponding relation of γ and a_0 is $\gamma \overset{THP}{\approx} \frac{2}{\pi}\frac{a_0^2/2}{\sqrt{(1+a_0^2/2)}}$. The determination of the linear and nonlinear plasma wavelength and frequency, respectively from the two optical diagnostics is explained in the following sections.

4.2.3.1 Plasma Wave Imaging

In region II ($x > x_{SF}$), the linear plasma wavelength and thus, the pure electron density could be deduced.

The top image of Fig. 4.5(a) shows a contrast enhanced shadowgram with a plasma wave in region II, i.e., after the shockfront. The middle image depicts the central lineout of the

plasma wave from which the local plasma wavelength $\lambda_{p,nl}$ (red line in bottom image of Fig. 4.5(a)) was deduced with the CWT method (cf. section 3.4.1.1). Employing Eq. (4.1), n_e/γ can be calculated, which is shown as blue line in the bottom image of Fig. 4.5(a). For the retrieval of the pure electron density n_e, the section of the plasma wave from which the linear plasma wavelength can be extracted has to be chosen carefully.

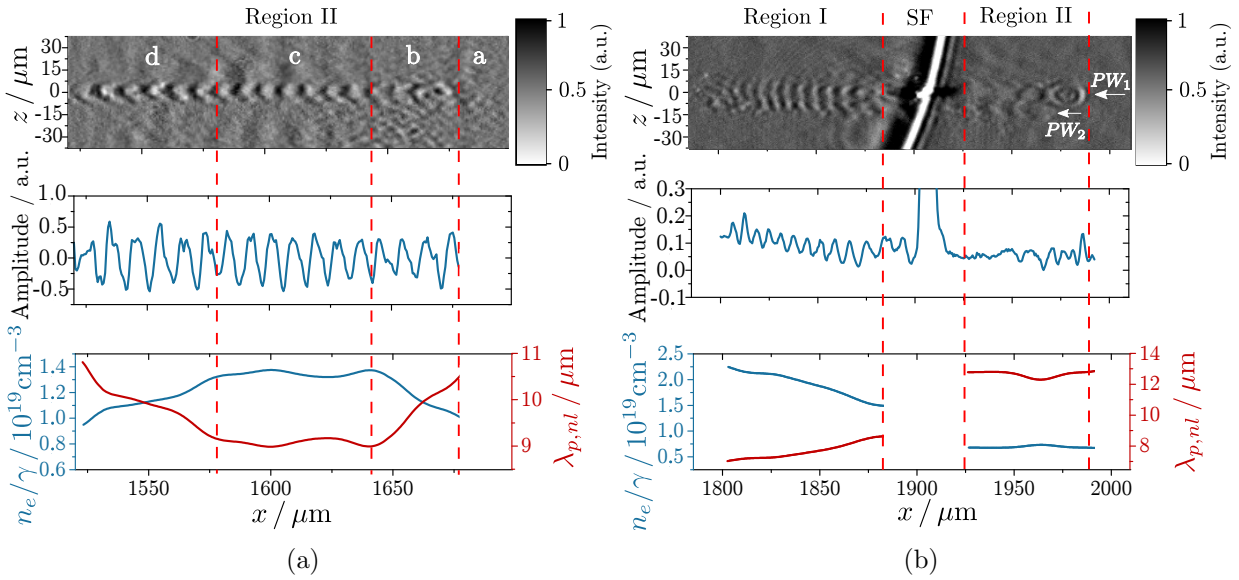

Figure 4.5 *Plasma wave (a) after and (b) in front of and after the shockfront. The subdivisions in the images mark different parts of the plasma wave or the area around the shockfront, respectively.*

The images in Fig. 4.5(a) are divided in four sub-regions: a represents the region in front of the plasma wave while in b, which here is extended over the first three plasma wave periods, a nonlinearly lengthened plasma wavelength can be observed. With increasing distance to the laser pulse, the lengthening becomes weaker – most likely due to the transfer of the oscillation energy to the background plasma – until in region c, the plasma wavelength is constant over seven periods. Due to the reduction of oscillation energy, γ eventually approaches 1 and the approximately constant plasma wavelength in c suggests that no further decrease of γ occurs. This allows to assume that $\gamma \approx 1$ in region c and hence, that one can deduce an approximately linear plasma wavelength. Here, $\lambda_p \approx 8\,\mu$m, which in the linear limit corresponds to $n_e \approx 1.7 \times 10^{19}\,\mathrm{cm}^{-3}$. The plasma wave periods in d are slightly asymmetric with respect to $z = 0$ and the plasma wavefronts have developed a sharp edge, which leads to an inaccurate determination of the wavelength by CWT in region d.

The plasma wave can only be imaged in intermediate electron densities since in high electron densities, the probe beam can be overshone by side scattered radiation (cf. Fig. 4.2(b)) while with decreasing electron density, changes in the index of refraction for a given probing wavelength are decreased and thus, the image contrast is reduced. Generally, the electron density in front of the density transition was to high for plasma wave imaging in the re-

ported experiments. Moreover, for the lowest nozzle backing pressure (8 bar) applied to the nozzle with $d_{out} = 2.1\,\mathrm{mm}$, the image contrast was to low for plasma wave imaging after the density transition. However, on very rare occasions, the plasma wave can be imaged simultaneously in the high density before and in the low density behind the shockfront as shown in the top image of Fig. 4.5(b). Here, the different regions mark the plasma wave behind the shockfront (region II), the area around the shockfront (SF) and the plasma wave in front of the shockfront (region I). A special feature of this shadowgram is that here two plasma waves – PW_1 and PW_2 – were independently driven by separate fractions of the same laser pulse. Since the depth of modulation of PW_2 appears to be significantly weaker than the modulation of PW_1, PW_2 might be driven by a side focus (c.f. Fig. 3.2(b)). The central lineout of the plasma wave PW_1 is shown in the middle image of Fig. 4.5(b), from which except for the part with the shockfront, the plasma wavelength and n_e/γ could be deduced (cf. bottom image of Fig. 4.5(b)). Since generally, the density before the density transition (in region I) gradually increases with larger values of x [47, 109], the increasing plasma wavelength in region I is most likely caused by an increasing γ-factor, i.e., the laser pulse might have evolved to a very high intensity such that the reduction of the γ-factor through the transfer of energy to the background plasma is still in progress at distances $> 100\mu$m behind the position of the laser pulse or front of the plasma wave. Nevertheless, due to the poor image contrast in the front part of the shadowgram in Fig. 4.5(b) and the asymmetries in the rear part, which are mainly caused by the double plasma wave, the deduction of plasma wavelength and n_e/γ might be subject to large errors. Although Fig. 4.5(b) shows an intriguing image of the interaction, such plasma waves were not used for the determination of the linear plasma wavelength , which for the following considerations was carried out with clearly imaged plasma waves exhibiting an approximately constant plasma wavelength as shown in region c in Fig. 4.5(a).

Linear plasma wavelength in region II for different positions of the shockfront. The linear plasma wavelength was measured directly after the shockfront. Fig. 4.6 shows the results for different nozzle backing pressures and different positions of the knife edge in the plasma, which are represented by the position of the shockfront $x_{SF} \approx 2x_{KE}$. Although the plasma wavelength for the lowest backing pressure (8 bar) could not be measured by imaging the plasma wave, it is possible to extrapolate the missing value by comparing the trends of the linear plasma wavelength presented here and the nonlinear plasma wavelength in region II introduced in the following section. Therefore, the electron density in region II will be discussed afterwards in section 4.2.4.2.

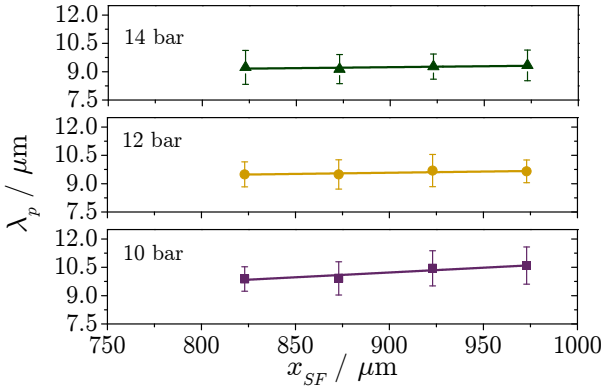

Figure 4.6 *Linear plasma wavelength in region II directly after the shockfront measured for different nozzle backing pressures p_N and knife edge positions x_{KE} represented by the position of the shockfront $x_{SF} \approx 2x_{KE}$. The lines are linear fits to the data.*

4.2.3.2 Raman Scattered Laser Light

Raman shifted laser light could be observed in region I ($x < x_{SF}$) and region II ($x > x_{SF}$). Hence, the nonlinear plasma wavelength and n_e/γ could be deduced before and after the shockfront.

Due to the coupling of laser radiation to the plasma wave, a fraction of the laser radiation experiences a frequency shift (cf. section 2.2.3) by an integer multiple m of the plasma frequency $\omega_{p,nl}$, i.e., $\omega_m = \omega_L \pm m\omega_{p,nl}$ with ω_m being the frequency of the m-th Raman satellite. As reported in [110], the laser light is primarily scattered at the first plasma wave period which can be subject to nonlinear lengthening (cf. sections 2.3.1.5, 4.2.3.1) and generally, the spectral analysis of the scattered radiation and Eq. 4.2 deliver n_e/γ. This radiation is not only generated in forward direction but also scattered normally to the laser axis [110] and thus, can be detected in top view by the imaging spectrometer.

Fig. 4.7(a) shows a spatially resolved optical spectrum where the wavelength of the radiation is resolved along the ordinate and the abscissa corresponds to the pump laser's propagation direction x. The straight line at $\lambda_L = 2\pi c/\omega_L \approx 783\,\text{nm}$ represents the strongest component[1] of the JETI40 spectrum while the bent lines above and below correspond to the m-th Raman satellite, which are emphasised with red or black lines, respectively. The red line was retraced manually while the black lines were calculated from the red line in combination with λ_L. However, the calculated lines reproduce the measured spectral lines quite well.

The Raman lines in Fig. 4.7(a) exhibit a discontinuity at $x \approx 1100\,\mu$m, which clearly correlate to a discontinuity of $\lambda_{p,nl}$ and n_e/γ occurring at the same position (cf. Fig. 4.7(b)). In front of the discontinuity ($x < 1100\mu$m), $\lambda_{p,nl}$ decreases, which indicates an increase of the electron density n_e and/or a decrease of γ, which would suggest decreasing laser intensities. Since at this early stage during the interaction an increase of laser intensity due to the laser pulse's nonlinear evolution in the plasma would be expected, the rising profile of n_e/γ is most likely caused by an increasing electron density profile. Electron density profiles with a

[1]Note that the strongest line is not necessarily the central wavelength (cf. Appendix A.1.1).

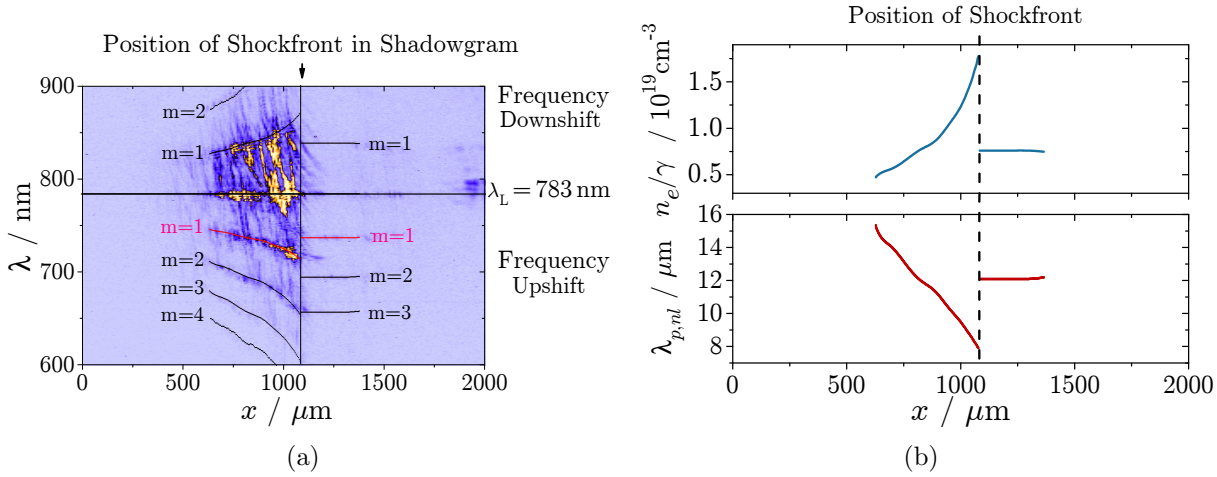

Figure 4.7 *(a) Spatially resolved optical spectrum. The straight horizontal line at 783 nm (emphasised with a solid black line) represents the fundamental laser wavelength while the bent lines are Raman satellites of the order m. The discontinuity of the Raman lines is due to a discontinuity of the electron density generated by a shockfront inside the gas jet. The spectrum is also shown in Appendix B.1 without the additional lines on top. (b) Nonlinear plasma wavelength and n_e/γ retrieved from the Raman satellites.*

similar shape were obtained from numerical flow simulations [109]. Within the width of the discontinuity, which is on the order of few micrometers, the laser intensity and therefore, γ can be assumed to be constant. Hence, the discontinuity can be attributed solely to a sudden change of the electron density, which here is generated by the shockfront induced by the knife edge, which forms a density transition at the position x_{SF}. Different electron density profiles $n_e(x)$ will be discussed in section 4.2.4.4.

Nonlinear plasma wavelength in regions I and II for different positions of the shockfront. The Raman scattered laser light could be observed directly before and after the shockfront, i.e., in regions I and II, respectively. The nonlinear plasma wavelengths in both regions calculated from the Raman satellites are shown in Fig. 4.8 for different backing pressures and different positions of the knife edge in the plasma, which are represented by the position of the shockfront $x_{SF} \approx 2x_{KE}$. In the following sections, some characteristics of the electron density profile of and around the shockfront will be deduced from the nonlinear plasma wavelengths presented here and the linear plasma wavelengths introduced in section 4.2.3.1.

4.2.4 Electron Density and Nonlinear Effects

Aspects of the electron density profile of the shockfront are investigated with the help of the linear (by sideview imaging) and nonlinear (from Raman shifted laser light) plasma wavelengths.

The results introduced in the following sections were achieved using a gas nozzle with a diameter of $d_{out} = 2.1\,\text{mm}$ during Campaign 2. Nevertheless, the undisturbed electron

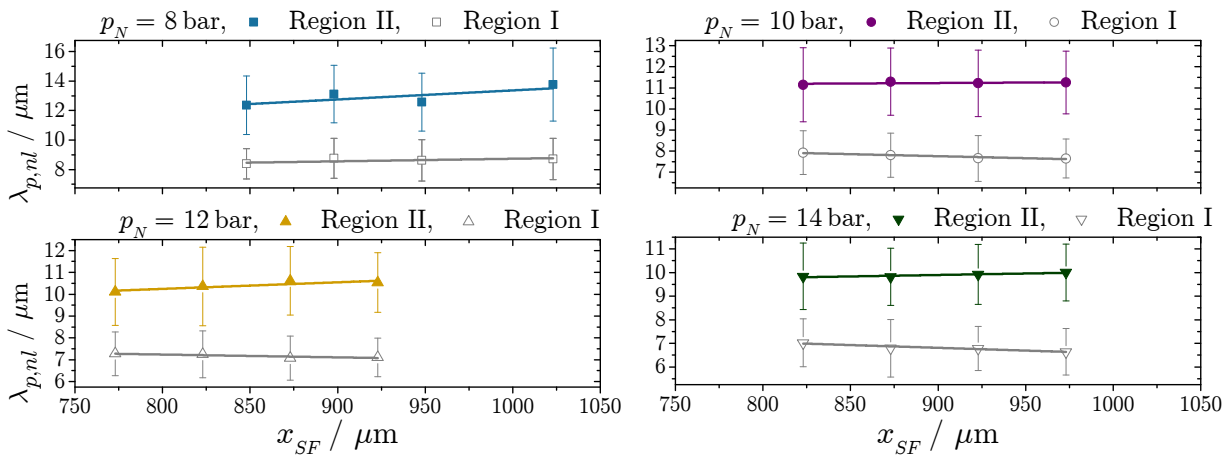

Figure 4.8 *Nonlinear plasma wavelength in region I and region II for different backing pressures and positions of the knife edge x_{KE} represented by the position of the shockfront $x_{SF} \approx 2x_{KE}$. The lines are linear fits to the data.*

density n_0 scales as p_N/d_{out}^2 and can be estimated for the case when using the larger nozzle with $d_{out} = 3.1\,\mathrm{mm}$ employed in Campaign 1. Furthermore, the comparable behaviour of shockfront position x_{SF} and angle α with respect to the position of the knife edge for both nozzles allows to assume similar streaming properties of the gas jet when the knife edge is inserted in both cases and thus, the scalability of the peak electron density n_{SF}.

In the following sections, the electron density profile of and around the shockfront is investigated with the help of the linear and nonlinear plasma wavelengths introduced above. This includes the determination of

1. the relativistic γ-factor by comparing the linear and nonlinear plasma wavelengths directly after the shockfront,

2. the electron density after the shockfront n_0, which requires the linear as well as the nonlinear linear plasma wavelength for extrapolation purposes,

3. the electron density ratio n_{SF}/n_0 of the peak electron density of the shockfront n_{SF} and the undisturbed electron density after the shockfront n_0, which could be deduced from the ratio of the nonlinear plasma wavelengths directly before and after the density transition,

4. the peak electron density of the shockfront n_{SF} using the density ratio n_{SF}/n_0 and the electron density after the shockfront n_0,

5. some electron density profiles $n_e(x)$ with the help of the nonlinear plasma wavelengths before and after the shockfront in combination with the γ-factor.

4.2.4.1 Relativistic γ-Factor after the Shockfront

For different positions of the shockfront and nozzle backing pressures, $\gamma \approx 1.18 \pm 0.60$ could be determined from the linear and nonlinear plasma wavelength directly after the shockfront.

A laser pulse propagating through a plasma evolves to higher intensities (cf. section 2.2.3), which is equivalent to an increasing γ-factor of the oscillating plasma wave electrons. Here, the γ-factor of the oscillating plasma wave electrons could be determined by means of the linear (cf. section 4.2.3.1) and nonlinear plasma wavelength (cf. section 4.2.3.2) via $\gamma = (\lambda_{p,nl}/\lambda_p)^2$ (cf. Eq. 4.1). The results for linear and nonlinear plasma wavelengths measured directly after the shockfront are shown in Fig. 4.9(a) for different shockfront positions $x_{SF} \approx 2x_{KE}$ and nozzle backing pressures.

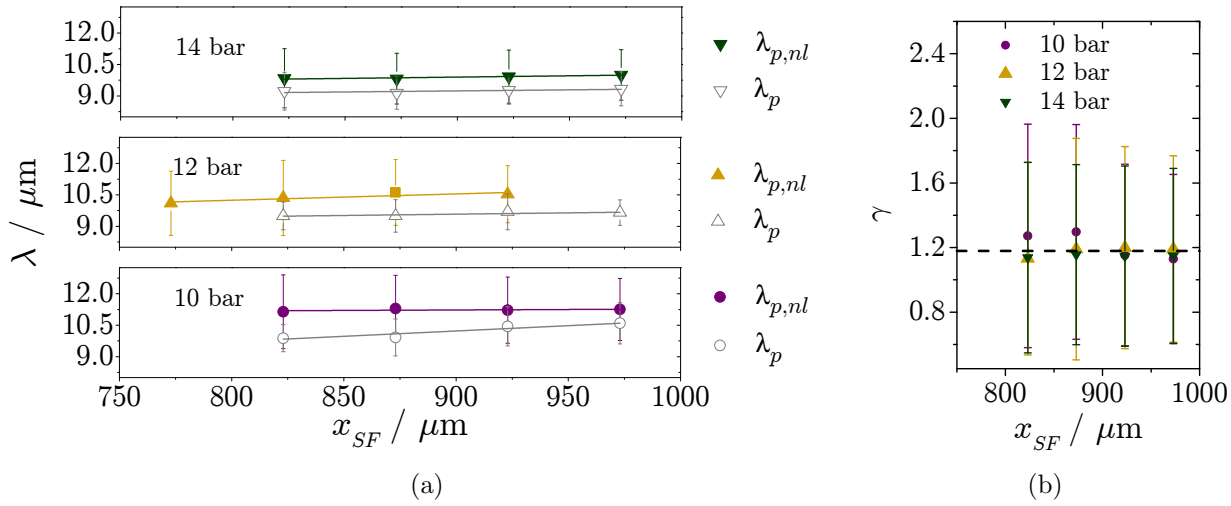

Figure 4.9 *(a) Comparison of the linear and nonlinear plasma wavelengths after the shockfront for different nozzle backing pressures and positions of the knife edge x_{KE} represented by the position of the shockfront $x_{SF} \approx 2x_{KE}$. The lines are linear fits to the data. (b) Relativistic γ-factor calculated from the ratio of linear and nonlinear plasma wavelengths. Here, the dashed line marks the average.*

Since the trends of the linear and nonlinear plasma wavelengths measured in region II directly after the shockfront are comparable for a given nozzle backing pressure, $\gamma = (\lambda_{p,nl}/\lambda_{p,})^2$ (cf. Eq. 4.1) is constant within its error bars and amounts to $\gamma \approx 1.18 \pm 0.60$, i.e, an increase of γ with the expected increase of the laser intensity cannot be confirmed by measurements (cf. Fig. 4.9(b)). Although error bars for the γ-factor reaching below $\gamma = 1$ are physically not relevant, they are the result of the statistical analysis, which simultaneously might be the reason for the seemingly non-evolving laser pulse intensity. Furthermore, the determination of a seemingly constant γ-factor could be caused if the assumption $\gamma \approx 1$ for the deduction of the linear plasma wavelength from the shadowgrams is not correct. Moreover, the measurements might be not sufficiently sensitive to determine γ. PIC-simulations might help to explore the relation of the plasma wavelength, the γ-factor

and the scattered radiation in more detail. An alternative experimental method to observe the evolution of the laser pulse will be presented in chapter 5 where the influence of magnetic fields on the state of polarisation of a probe pulse is explored.

4.2.4.2 Electron Density n_0 after the Shockfront

The electron density after the shockfront n_0 ***linearly depends on the nozzle backing pressure*** p_N***. Both nozzles with*** $d_{out} = 2.1\,mm$ ***and*** $d_{out} = 3.1\,mm$ ***were operated with backing pressures producing comparable density ranges of*** $(0.77 - 1.31) \times 10^{19}\,cm^{-3}$***.***

Since the linear as well as the nonlinear plasma wavelengths after the shockfront (cf. Fig. 4.9(a)) can be considered to be constant within their error bars, their average was calculated for each nozzle backing pressure p_N. Those averages are shown in Fig. 4.10(a) as red filled circles and blue filled squares. Due to the similar dependency of λ_p and $\lambda_{p,nl}$ on the backing pressure, the linear plasma wavelength for the smallest backing pressure $p_N = 8\,\text{bar}$ could be interpolated and is depicted as a grey star.

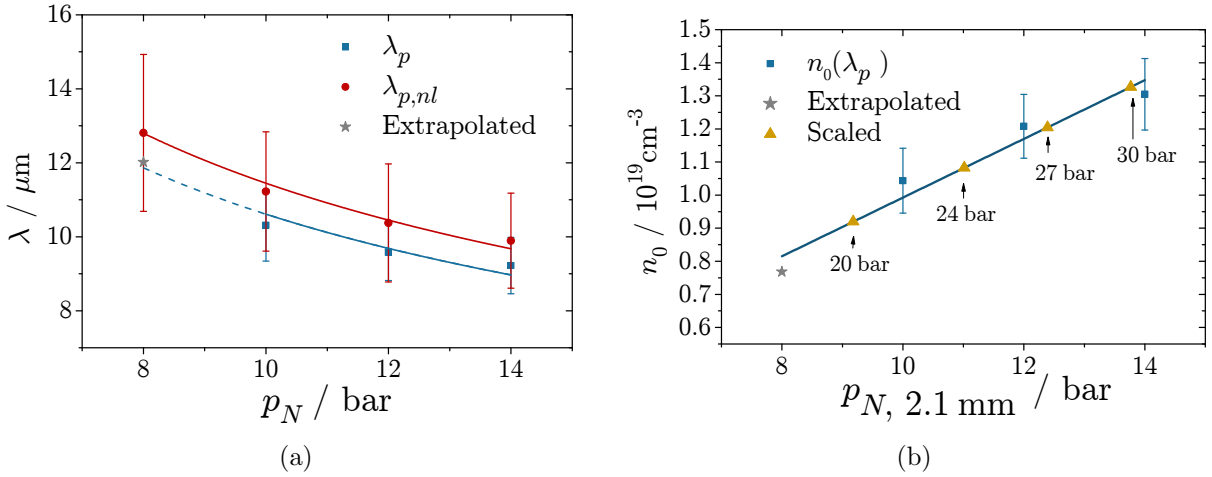

Figure 4.10 *Averages of (a) the linear (blue) and nonlinear (red) plasma wavelengths after the shockfront and (b) the corresponding electron density of the nozzle with* $d_{out} = 2.1\,mm$*. The lines in (a) are* $1/\sqrt{p_N}$ *fits and in (b) a linear fit to the data. The grey stars in both images represent interpolated values. Furthermore, the yellow triangles in (b) depict the scaled electron density for the larger nozzle with* $d_{out} = 3.1\,mm$*.*

As $\lambda_p = 2\pi c\sqrt{\frac{\epsilon_0 m_e}{n_0 e^2}}$, n_0 can be calculated and each backing pressure p_N can be related to the electron density n_0 of the density plateau behind the shockfront. Fig. 4.10(b) shows the electron density calculated from the linear plasma wavelength as blue squares and the extrapolated value as a grey star. To find the scaled electron densities for the larger nozzle, the actual backing pressure was downscaled via $p_{scaled,3.1\,mm} = p_{N,3.1\,mm}\left(\frac{2.1\,mm}{3.1\,mm}\right)^2$. With those downscaled backing pressures, the electron densities (represented by yellow triangles) for the larger nozzle can be read from the linear fit in Fig. 4.10(b). Note that both nozzles were operated in the same density regime.

4.2.4.3 Density Ratio of the Transition and Density of the Shockfront n_{SF}

The density ratio n_{SF}/n_0 as well as the the peak electron density n_{SF} directly in front of the density transition increase for shockfront positions deeper inside the gas jet. n_{SF} additionally increases with nozzle backing pressure p_N.

As explained before, the Raman scattered laser light is a measure of the nonlinear plasma frequency, i.e., the knowledge of γ would be required if one wanted to deduce the actual plasma density at the point from which this light is scattered. Nevertheless, the width of the density transition w_{SF} is on the order of $\approx 8\,\mu$m, which justifies the assumption $\gamma = constant$ at and directly after the front for any position x_{SF} in the plasma. Therefore, the density ratio can be estimated as $\frac{n_{SF}}{n_0} = \left(\frac{\lambda_{p,nl,0}}{\lambda_{p,nl,SF}}\right)^2$. The nonlinear plasma wavelengths in both regions calculated from the Raman satellites are shown in Fig. 4.8 for different backing pressures.

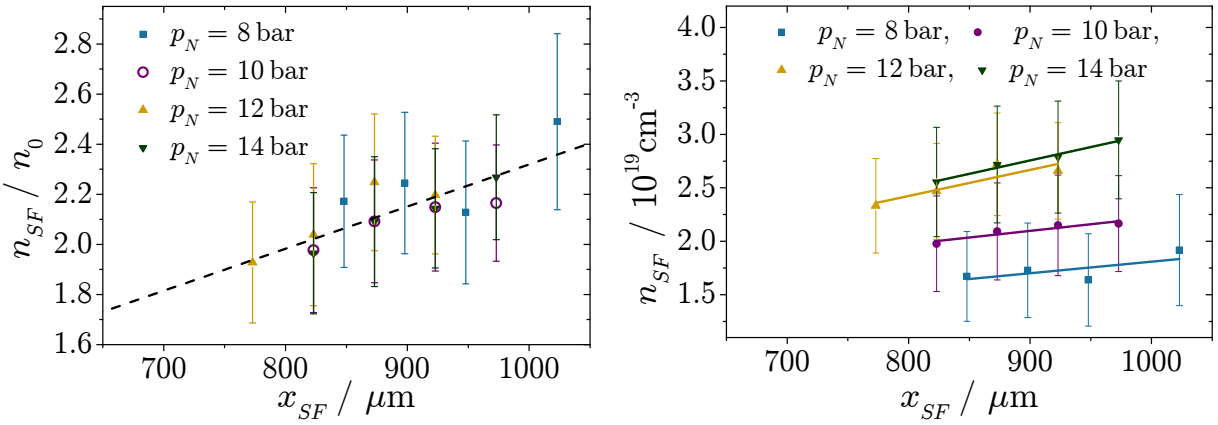

Figure 4.11 *(a) Electron density ratio n_{SF}/n_0 and (b) electron density of the shockfront n_{SF} for different nozzle backing pressures and positions of the knife edge x_{KE} represented by the position of the shockfront $x_{SF} \approx 2x_{KE}$. The lines are linear fits to the data.*

Similar to x_{SF} and α, the density ratio n_{SF}/n_0 depicted in Fig. 4.11(a) does not show a dependence on the nozzle backing pressure p_N. Although the error bars in Fig. 4.11(a) are large, an increase of n_{SF}/n_0 is clearly recognisable for increasing shockfront positions x_{SF}.

It was shown in section 4.2.2 that the shockfront angle α increases with the position of the knife edge x_{KE} which according to Eq. (1) in [47] leads to a decrease of n_{SF}/n_0. Nevertheless, when the knife edge is moved deeper into the gas jet, the area of the nozzle covered by the obstacle increases and more gas has to flow around. Thus, the shockfront becomes stronger and counteracts the expected decrease of n_{SF}/n_0. The increase of the shock angle as well as the density ratio for knife edge positions deeper inside the gas jet could be confirmed using numerical flow simulations [109].

Additionally, the peak electron density at the shockfront n_{SF} can be estimated with the

help of the density ratio n_{SF}/n_0 in combination with the electron density n_0 in region I (cf. section 4.2.4.2). Fig. 4.11(b) shows that the density of the front n_{SF} increases both as a function of the nozzle backing pressure p_N and of the shockfront position x_{SF}.

4.2.4.4 Electron Density Profile

Depending on the exact electron density profile of the shockfront, electron injection might not be restricted to the position of the shockfront.

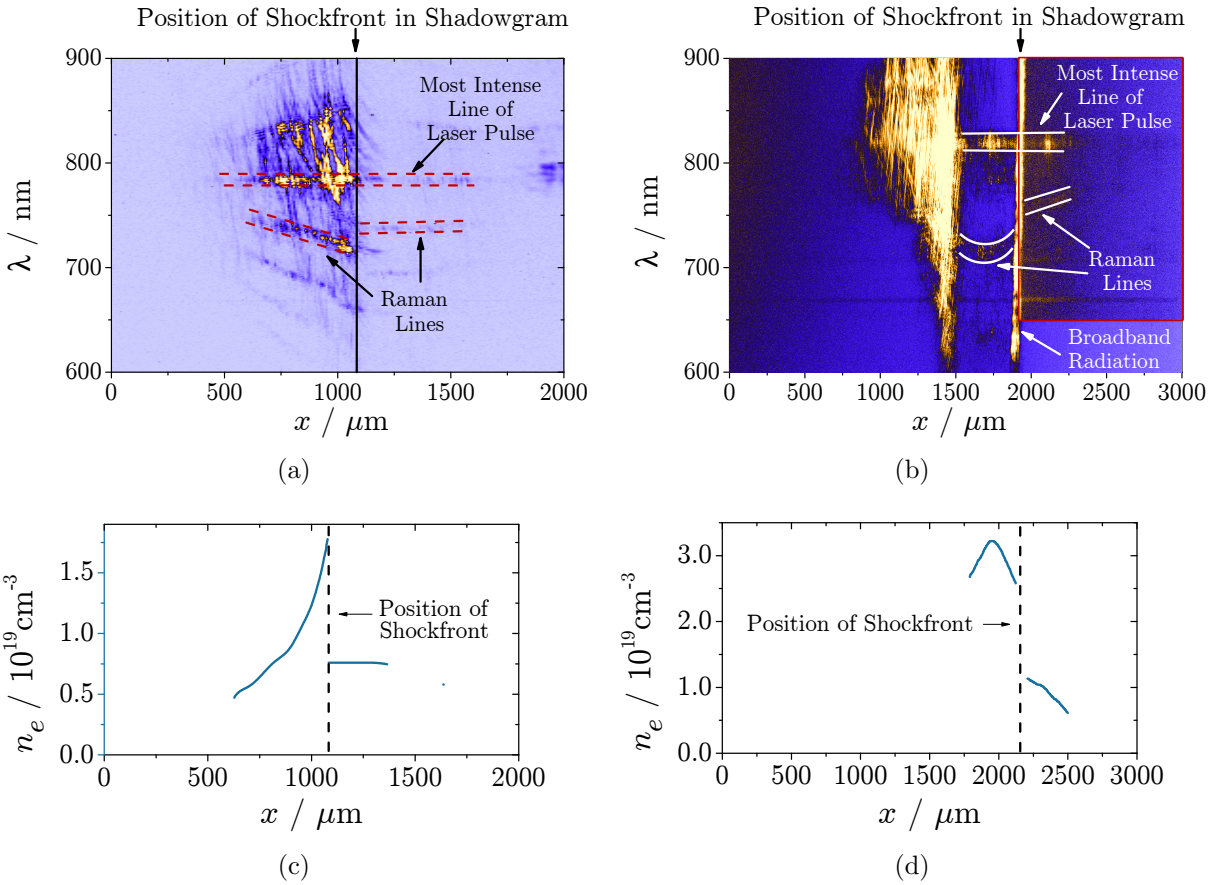

Figure 4.12 *Spatially resolved optical spectrum showing laser radiation scattered at (a) an ideal and (b) a disadvantageous electron density profile. The retrieved density profiles are shown underneath the respective spectrum. Note that the image contrast in (b) is increased to visualise the Raman satellites. The strongest increase of contrast was applied to the red boxed area. The image with original contrast is shown in Appendix B.1. The continuously broadening radiation between 800 μm and 1500 μm is the self modulated spectrum of the laser pulse and the broadband radiation at $x \approx 1850\,\mu m$ is discussed in section 4.3.*

With the imaging spectrometer, the whole interaction length could be observed in a single shot and under ideal conditions – if the Raman satellites are clearly visible over a large region in laser-propagation direction x – the profile of $n_e(x)/\gamma$ can be retrieved (cf. section 4.2.3.2). In combination with a constant γ-factor between $x \approx 500$ and $1900\,\mu m$, the linear electron density profile $n_e(x)$ can be estimated. Although $\gamma = constant$ could not be confirmed in that entire range, $\gamma \approx 1.18$ is adopted from section 4.2.4.1. Nevertheless,

the interpolation of $\gamma = constant$ to a broader range might lead to a significant error in the estimation of $n_e(x)$. Therefore, it has to be kept in mind that the profiles can only be regarded as a rough estimate.

Fig. 4.12(a) shows a spatially resolved optical spectrum, which was already introduced in section 4.2.3.2. The corresponding electron density profile calculated under the above stated assumptions is shown in Fig. 4.12(c) and represents the ideal profile for electron injection at a shockfront. In the increasing density in front of the transition, the plasma wavelength decreases and thus, the phase velocity at the rear of each plasma wave period is decreased with respect to the preceding plasma wave period and the injection of electrons into the plasma wave is avoided (cf. section 2.3.1.3 and 2.3.3). However, at the transition, the situation is reversed and injection is supported by a sudden decrease of phase velocity at the rear of the plasma wave (cf. section 2.3.3), which is caused by the increase of the plasma wavelength in the lower electron density n_0. In contrast, the profile in Fig. 4.12(d), which was retrieved from the spectrum in Fig. 4.12(b) exhibits a continuously decreasing electron density before and after the transition and thus, the position of injection is not necessarily given by the position of the transition.

Although the spectra in Fig. 4.12(a) and (b) were detected in different campaigns, the corresponding electron density profiles are not campaign specific. The shift of the most intense spectral line of the JETI40-spectrum between Campaign 1 and Campaign 2 is briefly discussed in Appendix A.1.1.

Note, that it was not possible to select the data based on the specific density profile as this profile could only be reconstructed for a small number of shots.

4.3 Wavebreaking at the Shockfront

The position x_{WBR} where wavebreaking radiation is emitted identifies the position at which electrons are injected into the plasma wave. Hence, the exact overlap of x_{WBR} and the position of the shockfront x_{SF} demonstrates that electrons are injected in close vicinity to the shockfront.

Since the breaking of the plasma wave is accompanied by the emission of broadband radiation due to the rapid acceleration of charged particles [94] (cf. section 2.3.4), the position of the emission of wavebreaking radiation x_{WBR} – and hence, the position of injection – could be determined using the imaging spectrometer. For each shot for which wavebreaking radiation was detected, the position of the shockfront x_{SF} observed in sideview with the probe beam and its imaging system was determined as well. By comparing these positions, electron injection at the shockfront was investigated.

The measurement was performed with a nozzle with $d_{out} = 3.1\,\mathrm{mm}$ at an electron density $n_0 \approx 1.3 \times 10^{19}\,\mathrm{W/cm^3}$. The knife edge was moved deep into the gas jet ($x_{KE} \approx 950\,\mu\mathrm{m}$),

which intrinsically provides a variation of the shockfront position x_{SF} by $\approx \pm 200\,\mu$m (cf. section 4.2.2).

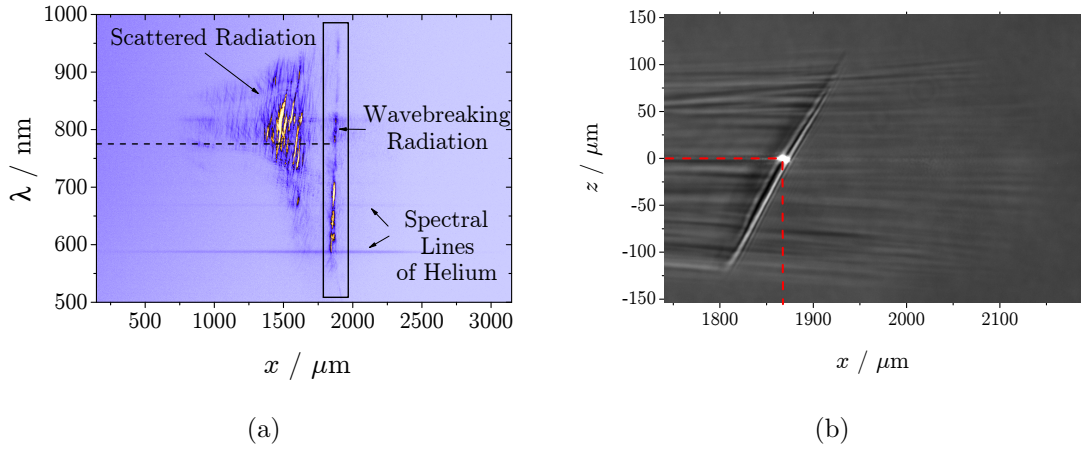

(a) (b)

Figure 4.13 *(a) Spatially resolved optical spectrum showing broadband radiation indicative for wavebreaking (emphasised by a black box). (b) Shockfront in the shadowgram of the same shot. Here, the position of the shockfront x_{SF} is marked by the intersection of the dashed lines. The bright spot at this position corresponds to the emission point of broadband radiation, which was simultaneously detected in top view.*

In the spatially resolved optical spectrum shown in Fig. 4.13(a), scattered laser light and Raman satellites are visible at positions $x \leq 1650\,\mu$m. Moreover, at a position $x_{WBR} \approx 1870\,\mu$m, a broad spectrum is emitted within a width of $\approx 70\,\mu$m in the laboratory frame which is consistent with the characteristics of wavebreaking radiation [94]. Note that the spectral distribution of the broadband radiation shows a weak dependence on the position x, more precisely shorter wavelengths seem to be emitted earlier, i.e., at smaller values of x. This is most likely caused by a misalignment of the imaging spectrometer. Due to this tilt, the position of the emission of wavebreaking radiation x_{WBR} (dashed line in Fig. 4.13(a)) was determined at $\lambda = 775\,$nm, which is approximately the central wavelength of the broadband radiation.

Fig. 4.13(b) depicts a shadowgram with a shockfront, which intersects the laser axis at the position x_{SF}. This position x_{SF} was determined for each shot for which wavebreaking radiation was detected. Frequently, a bright spot can be observed at the intersection of shockfront and laser axis, which is most likely a signature of the emitted broadband radiation in the shadowgrams. However, bright emission visible in shadowgrams can also be caused by laser light side scattered at high electron densities (cf. Fig. 4.2(b)).

It was observed that the frequency of occurrence of wavebreaking radiation decreases with decreasing background electron density and when moving the shockfront positions closer to the beginning of the gas jet. This is most likely caused by a reduction of injected charge (cf. Appendix B.3.1), i.e., the injection of small charges is possibly not detectable

with this method and thus, the absence of wavebreaking radiation in the spatially resolved spectra does not rule out the injection of electrons.

Nevertheless, the linear relation of x_{WBR} and x_{SF} in Fig. 4.14 shows that the detected broadband radiation is emitted close to the shockfront with a standard deviation of $\Delta x_{WBR} \approx \pm 35\,\mu$m. The deviation of x_{WBR} from x_{SF} can for example be caused by the misalignment of the imaging spectrometer or vibrations of the imaging optics which would lead to a reduced accuracy in the determination of x_{WBR} and x_{SF}. On the other hand, the deviation might be real and could be caused by disadvantageous electron density profiles as introduced in section 4.2.4.4.

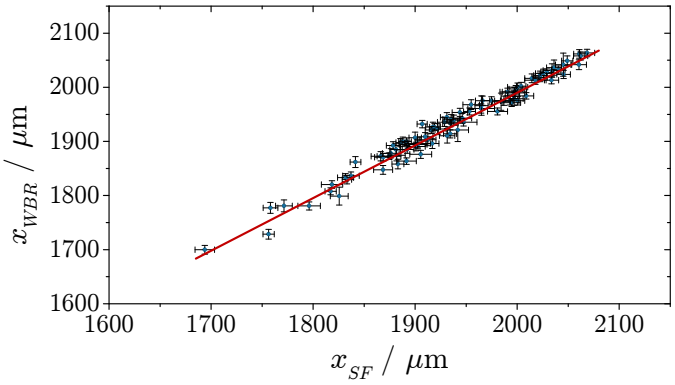

Figure 4.14 *The position of the emission of wavebreaking radiation x_{WBR} was found to be in close vicinity to the position of the shockfront x_{SF}, which was determined in sideview for each shot for which wavebreaking radiation was detected. The red line is a linear fit to the data.*

4.4 Influence on the Electron Energy Distribution

The charge detected with the electron spectrometer is significantly increased when the electron density profile exhibits a density transition. Both, monoenergetic and broadband electron distributions were obtained.

The measurements presented in the following sections were obtained during Campaign 2 using a nozzle with $d_{out} = 2.1\,$mm operated at four different backing pressures corresponding to electron densities between $n_0 \approx 7.7$ and $13.0 \times 10^{18}\,\mathrm{cm}^{-3}$ ($p_N = (8-14)\,$bar). Fig. 4.15(a) shows a typical energetically and angularly resolved electron density map – referred to as electron energy maps in the following sections – obtained in a reference measurement without knife edge at the lowest background electron density of $n_0 \approx 7.7 \times 10^{18}\,\mathrm{cm}^{-3}$. Here, the total charge amounts to $\approx 0.2\,$pC. In contrast, Figs. 4.15(b) and 4.15(c) show two types of electron energy maps which were frequently obtained at the same nozzle backing pressure however, with a knife edge driven into the gas jet. The charge contained in these electron energy maps is significantly higher and amounts to $\approx 1.2\,$pC (monoenergetic in Fig. 4.15(b)) and $\approx 7.4\,$pC (broadband in Fig. 4.15(c)), respectively. Note that both spectral components can also be generated in the same shot as shown in Fig. 4.15(d). The influence of the shockfront on the energy spread is discussed in section 4.4.2.1. Moreover, the frequently appearing energy dependent pointing variations of the electron beam in the electron energy map with

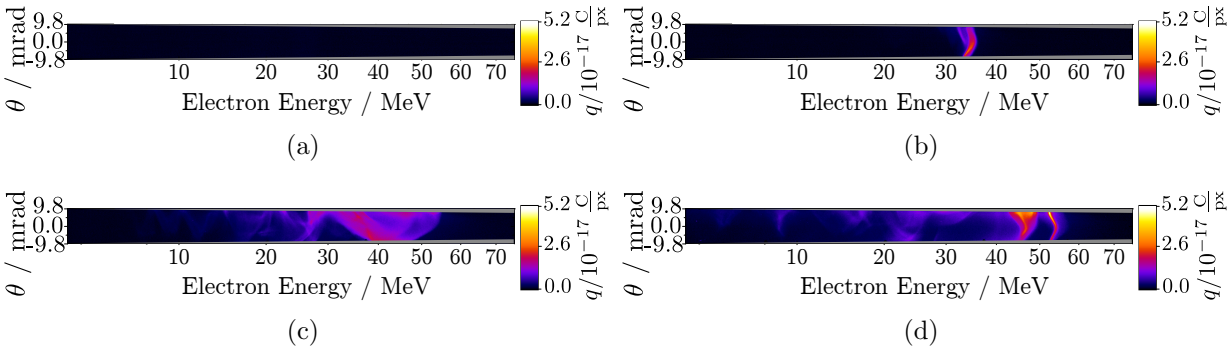

Figure 4.15 *Exemplary electron energy maps at $p_N = 8$ bar. (a) Reference electron energy map obtained without shockfront. (b) Electron energy map with monoenergetic electron distribution obtained with shockfront. (c) Electron energy map with broadband electron energy distribution and energy dependent pointing variations of the electron beam obtained with shockfront. (d) Electron energy map with a monoenergetic as well as a broadband component obtained with shockfront.*

broadband electron energy distribution as e.g. in Fig. 4.15(c) are discussed in detail in section 4.4.2.2.

4.4.1 Energy Gain

Due to the large fluctuation of the electrons' energy gain, the shots with top 10% electron energy were selected for further analysis. The maximum electron energy E of the selected data show a parabola like dependence on the position of the shockfront x_{SF}. Moreover, the maximum achievable electron energy E_{opt} is obtained by those electrons which are accelerated over the optimum acceleration distance l_{opt}. Electrons accelerated over $l_{acc} \neq l_{opt}$ gain a lower kinetic energy E.

Figs. 4.16(a)-4.16(d) show the maximum electron energy E (cf. Fig. 4.17(a)) with respect to the shockfront position x_{SF} which will be referred to as position of injection x_{inj} in the following sections. The black squares represent the data of single shots. Due to the large variation of the electron energy data, for each interval $\Delta x_{inj} = \pm 25\,\mu$m, the shots with the top 10 % electron energy were selected (red filled circles) for further analysis. This can be justified by the assumption that the generation of the highest electron energies is achieved under optimum acceleration conditions for given experimental settings. Reasons for the electron energy fluctuation are discussed in section 4.4.1.1. A parabolic fit to each set of selected data is shown in blue. Note, that a parabolic dependence of electron energy on the acceleration length assumes a linearly increasing $\mathcal{E}$-field with a fixed maximum electric field $\mathcal{E}_{max}$ as it can be expected for quasi static non-linear wakefields (cf. Fig. 2.5(b)). However, in section 4.4.1.4, an adapted interpretation will be presented.

The principal trend of the electron energy in Figs. 4.16(a)-4.16(d) reflects the dependence of the electron energy on the position of injection x_{inj}. Electrons injected close to the end of the gas jet gain only little energy as the remaining acceleration length l_{acc} is comparably short. The further the shockfront – and therefore, the position of injection

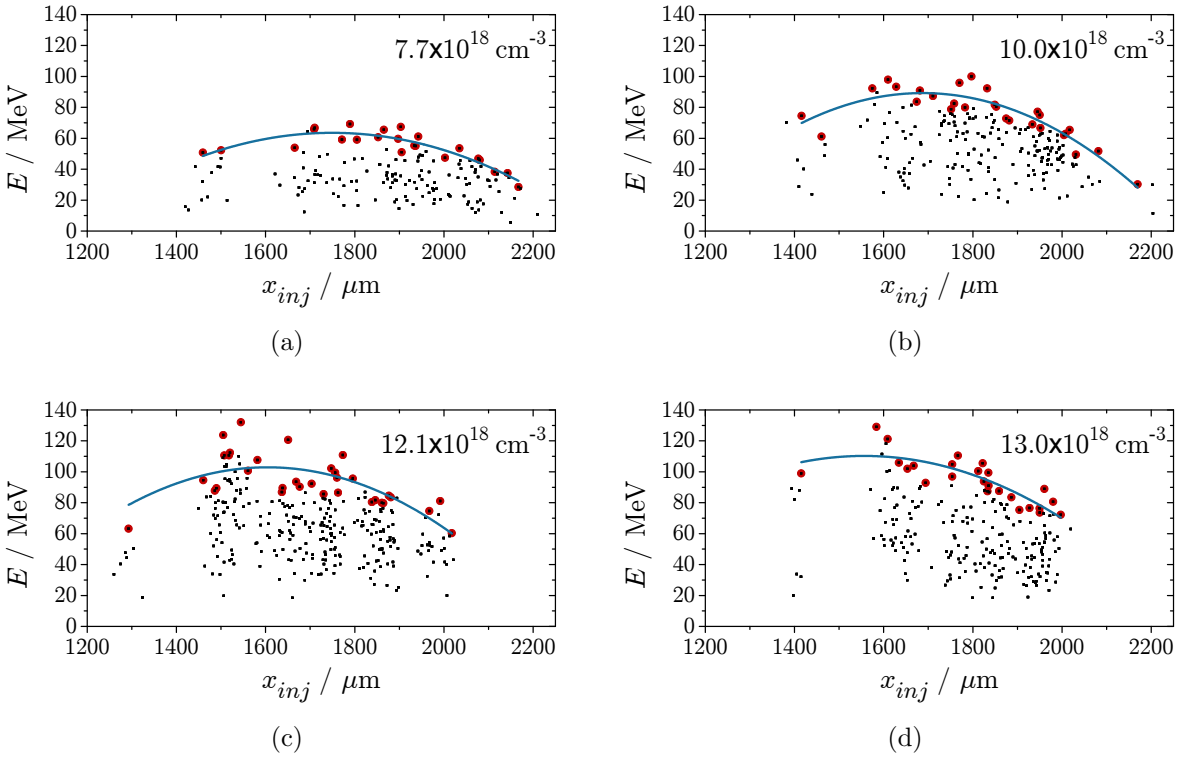

Figure 4.16 *Maximum electron energy E in dependence on the position of injection x_{inj}. In intervals of $\Delta x_{inj} = \pm 25\,\mu m$, the shots with the top 10 % electron energy (red dots) of the single data (black dots) were selected for the analysis of the electron energy gain in dependence on x_{inj} and the electron density n_0. Parabolic fits to the data are shown in blue.*

x_{inj} – is moved towards the beginning of the gas jet, the longer becomes l_{acc} resulting in an increased acceleration length and hence, electron energy gain E. Nevertheless, the increase of l_{acc} beyond the optimum acceleration length for which the electrons gain the maximum achievable kinetic energy, might cause a re-transfer of energy to the plasma. For instance, the limit to the acceleration distance can be pump depletion, diffraction or dephasing (cf. section 2.3.1.5). In the case of pump depletion or diffraction, the plasma wave is no longer driven by the laser pulse. However, the accelerated electron bunch can drive a second wake-field itself leading to a transfer of electron energy to the associated plasma wave [111] and consequently, to the deceleration of the driving electron bunch. In contrast, dephasing of the accelerated electrons with the laser driven plasma wave can only occur as long as the laser pulse is sufficiently intense to drive the plasma wave. In this case, the electrons are decelerated by the positive longitudinal electric field of the front half cycle of the corresponding plasma wave period. Assuming that the accelerated electrons cover the dephasing length with the speed of light c, the dephasing time can be expressed as

$$t_{deph} = \underbrace{\frac{l_{deph,nl}}{c}}_{a} = \underbrace{\frac{\lambda_{p,nl}}{2}\frac{1}{c - v_{ph,p}}}_{b}, \tag{4.3}$$

in the laboratory frame (term a) and the co-moving frame of reference (term b), where its dependence on the plasma wave's phase velocity and the length of the accelerating plasma wave period becomes obvious. With $c/(c - v_{ph,p}) \approx 2n_{cr}/n_e = 2(\lambda_p/\lambda_L)^2$, a simple estimate of the nonlinear dephasing length is given by

$$l_{deph,nl} = \frac{\lambda_p^2}{\lambda_L^2}\lambda_{p,nl}. \tag{4.4}$$

Since λ_p and $\lambda_{p,nl}$ could be deduced in the undisturbed region of the gas jet where the electrons are accelerated (cf. section 4.2.4), this relation will be used for the discussion of the acceleration limit.

E and E_{opt}. As illustrated in Fig. 4.17(a), E describes the maximum electron energy obtained in a specific shot. The electrons with the kinetic energy E were injected at a position x_{inj} and accelerated along the remaining acceleration length l_{acc}, which is shown in Fig. 4.17(b). In contrast E_{opt} labels the maximum achievable electron energy obtained by the electrons injected at the optimum injection position x_{opt} and accelerated along the optimum acceleration length l_{opt}. In order to prevent confusion with the naming of E and E_{opt}, E will be referred to as electron energy and E_{opt} will be called maximum energy in the following sections.

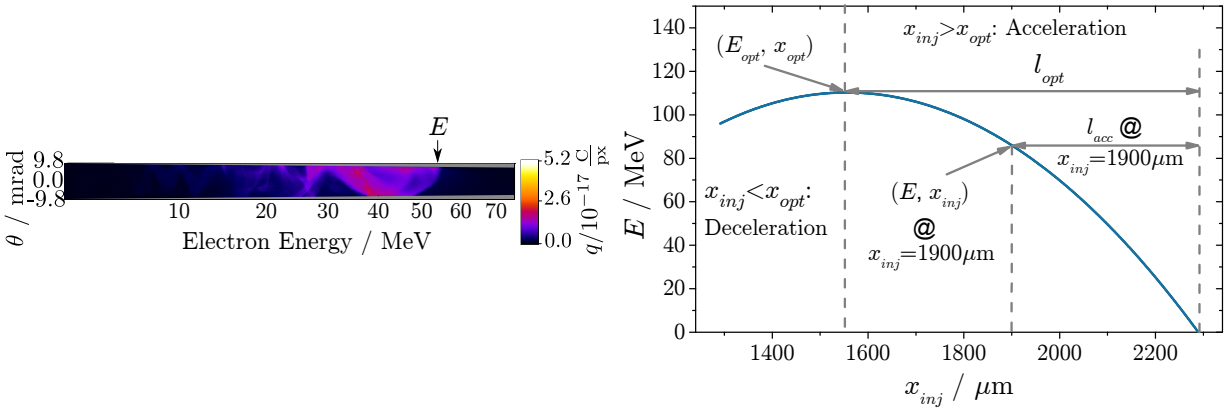

Figure 4.17 *Difference of E and E_{opt}. (a) The electron energy E corresponds to the maximum electron energy in a specific electron energy map. (b) The maximum electron energy E_{opt} is the maximum achievable electron energy of a given experimental setting.*

4.4.1.1 Fluctuation of the Electron Energy E

The observed fluctuations of the electron energy gain might be caused by the measurement of seemingly lower electron energies due to fluctuations of the electrons' pointing and instabilities in the acceleration process due to the nonlinear evolution of the laser pulse to higher intensities.

Since the pointing of two electron bunches generated in the same shot can differ [22], pointing fluctuations might cause the measurement of a seemingly decreased electron energy. The injection of two electron bunches in the same shot could for example occur in two different periods of the plasma wave. For electron pulses accelerated in different plasma wave periods, a different electron energy gain would be expected as with increasing distance to the laser pulse, the plasma wave periods are less strongly driven, i.e., electron pulses injected into the first plasma wave period generally gain a higher kinetic energy than electron pulses in trailing periods.

In vertical direction, the angle of acceptance of the electron spectrometer is limited by the extent of the scintillating screen, which amounts to $\approx \pm 8\,\mathrm{mrad}$ at 60 MeV and decreases with increasing electron energy. Moreover, in horizontal direction, the limitation is given by the width of the slit in front of the magnet and amounts $\approx \pm 4.55\,\mathrm{mrad}$ (cf. section 3.3). The electron beam pointing was measured in Campaign 1 and is discussed in Appendix B.3.3. Assuming similar pointing fluctuations of the electron bunches analysed in this section, the fluctuation in electron beam pointing most likely contributes to the electron energy fluctuation.

Furthermore, instabilities in the acceleration process and thus, in the electron energy gain can be caused by the nonlinear evolution of the laser pulse in the plasma. Although laser pulse evolution is not indicated by the constant γ-factor of the plasma wave electrons deduced at different positions of the shockfront (section 4.2.4.1), the most likely explanation for results in the following sections is based on laser intensity increases through laser pulse evolution (cf. sections 4.4.1.3, 4.4.2.1 and Appendix B.3.1). Laser pulse evolution in the plasma is investigated in more detail in chapter 5.

4.4.1.2 Optimum Acceleration Length and Maximum Achievable Electron Energy

Acceleration until the end of the target suggests that neither diffraction nor depletion limit the acceleration process. Furthermore, dephasing is unlikely since the maximum electron energy E_{opt} and the optimum acceleration length l_{opt} increase with increasing electron density n_0.

Fig. 4.18(a) shows the parabolic fits to the electron energy data, which were introduced in section 4.4.1. Note that those fits are shown in dependence on the position of injection x_{inj}. To emphasise that, the same fits are shown in Fig. 4.18(b) in dependence on the acceleration length l_{acc}. Between $\approx$ 2250...2350 μm in Fig. 4.18(a), all curves exhibit a zero crossing where the electron density (brown) is reduced to $0.5\,n_0$ suggesting that the acceleration process is terminated due to a longitudinal limitation of the plasma and hence the acceleration structure. Thus, neither depletion nor diffraction of the laser pulse seem to play a significant role for the small nozzle with $d_N = 2.1\,\mathrm{mm}$.

Furthermore, with the help of the maximum electron energy E_{opt} and the corresponding optimum acceleration length l_{opt} retrieved from the fits, the relevance of dephasing can be evaluated. In the case of dephasing, the optimum acceleration length l_{opt} would be given

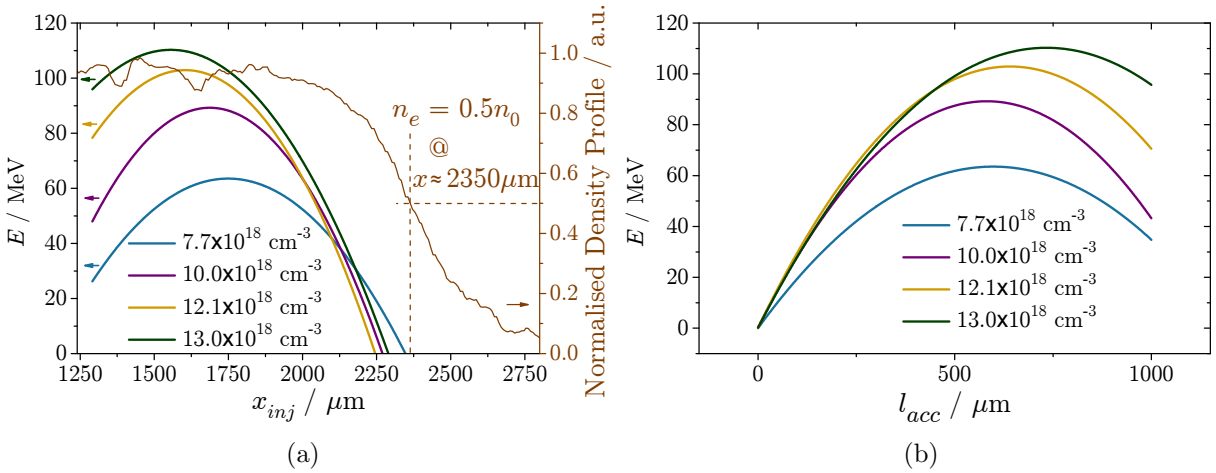

Figure 4.18 *(a) Parabolic fits of the relation of electron energy E and position of injection x_{inj} in different background electron densities and normalised electron density profile of the gas jet (brown). (b) The same parabolic fits in dependence on the acceleration length l_{acc}. Note that the parabolic fits do not necessarily indicate dephasing as the limit to the acceleration process.*

by the dephasing length $l_{deph,nl}$, which decreases with increasing electron density. As a consequence, the maximum achievable electron energy E_{opt} is reduced for increasing density although the accelerating electric fields $\mathcal{E}$ increase at the same time (cf. section 2.3.1.6). However, Fig. 4.19(a) shows that l_{opt} is shorter than $l_{deph,nl}$ for all electron densities n_0 and even increases with n_0, which also causes an increase of E_{opt} (cf. Fig. 4.19(b)). Hence, dephasing is an unlikely limit to the acceleration process.

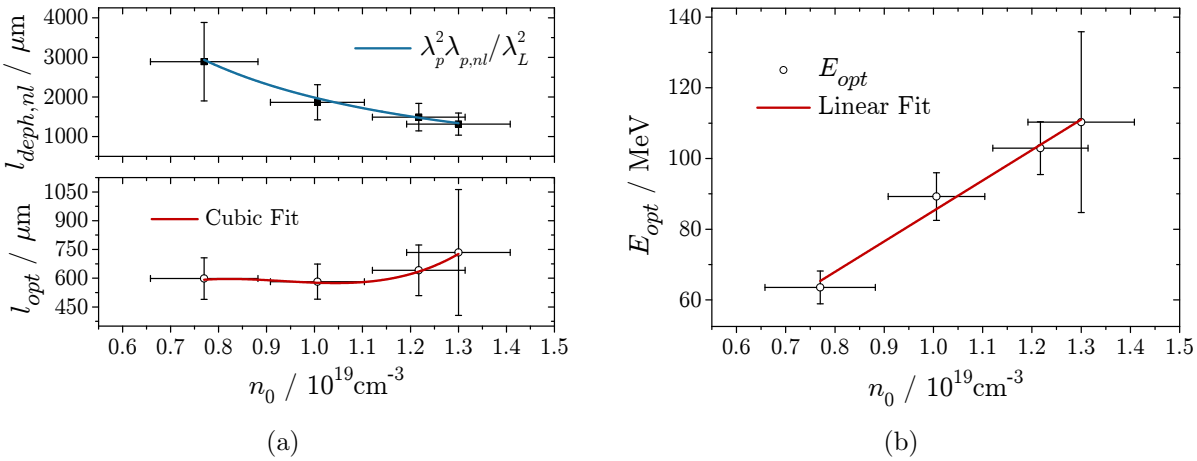

Figure 4.19 *(a) Comparison of the optimum acceleration length l_{opt} regarding the electrons exhibiting the maximum electron energy E_{opt} to the dephasing length l_{deph}. (b) Maximum electron energy E_{opt} in dependence on the electron density n_0.*

4.4.1.3 Acceleration Limit

The optimum acceleration length l_{opt} and thus, the maximum electron energy E_{opt} is probably determined by the evolution of the laser pulse to higher intensities and the remaining acceleration length behind the position of injection, and thus, the position of the electron density transition. The results demonstrate the importance of the observation of the evolution of the laser pulse, which with the help of results in chapter 5 might become possible in the near future.

With increasing electron density n_0, the optimum position of injection x_{opt} for those electrons gaining the highest final energies E_{opt} shifts towards the beginning of the gas jet (cf. Fig. 4.20(a)) and the optimum acceleration length l_{opt} (cf. Fig. 4.20(b)) lengthens. A

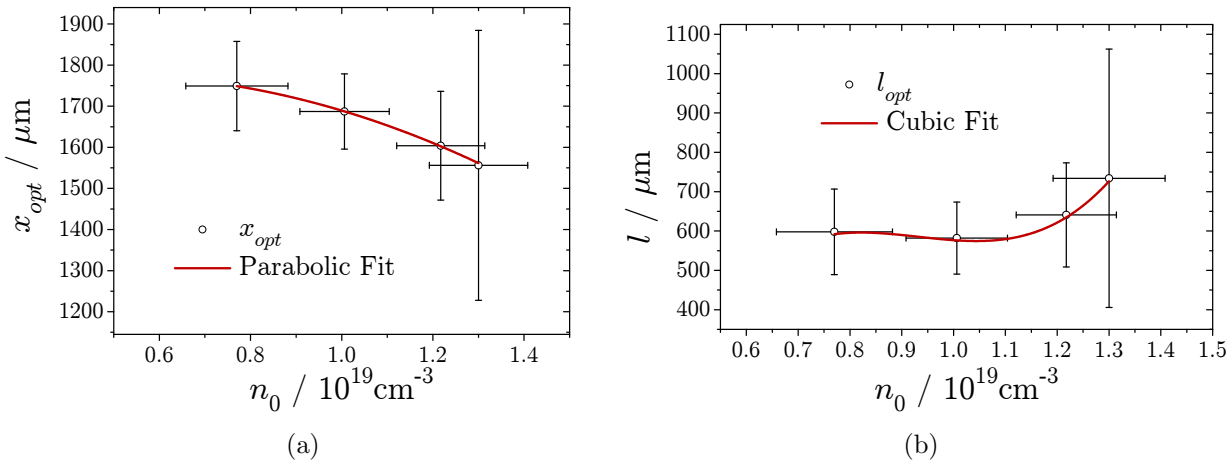

Figure 4.20 *(a) Optimum position of injection x_{opt} with respect to the electron density n_0. The red line is a parabolic fit which was chosen due to its match to the data. With increasing electron density, x_{opt} shifts towards the beginning of the gas jet and the (b) optimum acceleration length l_{opt} lengthens.*

possible reason for that is a more rapid evolution of the laser pulse in higher background densities [94]. In this case, the maximum electron energy E_{opt} and the corresponding optimum position of injection x_{opt} are most likely determined by an interplay of laser pulse evolution and remaining acceleration length l_{acc}, i.e., if the shockfront is located in front of x_{opt}, the electric field of the plasma wave – driven by a marginally evolved laser pulse – is too low to accelerate the electrons to E_{opt}. Vice versa, the larger electric field $\mathcal{E}$ of the plasma wave driven by a more strongly evolved laser pules is not sufficient to counterbalance the reduced acceleration length $l_{acc} < l_{opt}$.

It should be noted here, that the comparison of the linear and nonlinear plasma wavelengths at the position of the electron density transition resulted in $\gamma \approx 1.8$ and neither showed a dependence on the electron density nor on the position of the transition. Nevertheless, as already discussed in section 4.2.4.1, the determination of the γ-factor might not be sufficiently accurate for various reasons. Furthermore, discussions presented in sections 4.4.1.1, 4.4.2.1 and Appendix B.3.1 also suggest the evolution of the laser pulse to

higher intensities. Those contradictory results emphasise the importance of the observation of the evolution of the laser pulse for the interpretation of the experimental results. An alternative experimental approach to investigate the evolution of the laser pulse is presented in chapter 5 where signatures of the laser pulse's strong magnetic field are studied with the help of the ultra-short probe beam.

4.4.1.4 Maximum Accelerating Electric Field

$\mathcal{E}_{max}/\mathcal{E}_0 \approx 1$ ***suggests that the major fraction of the accelerated charge is injected as a consequence of the shockfront and an additional background charge might be caused by transverse wavebreaking.***

According to the argumentation in section 4.4.1.3, the parabolic relation of the electron energy E on the position of injection x_{inj} cannot be regarded in the 'classical' comprehension, which assumes that the acceleration of the injected electrons in a linearly decreasing electric field is determined by a maximum accelerating field $\mathcal{E}_{max}$ and plasma wavelength (dephasing length) at a given electron density n_0. Since here, the observed parabolic relation observed is most likely an interplay of a variable maximum electric field – due to the evolution of the laser pulse to higher intensities – with a varying acceleration length l_{acc}, which both depend on the position of the shockfront and hence, on x_{inj}, the evaluation of the accelerating electric field in this section only corresponds to the electrons injected at x_{opt}, which are accelerated to E_{opt}.

Nevertheless, for those electrons accelerated to E_{opt} considered separately, the acceleration in a linear electric field with a maximum electric field $\mathcal{E}_{max}$ along the acceleration distance l_{opt} is a valid assumption. Therefore, the relation of the electron energy E_{opt} on the acceleration length l_{opt} and the maximum electric field $\mathcal{E}_{max}$ is given by

$$E_{opt} = \frac{e}{2}\mathcal{E}_{max} l_{opt}, \tag{4.5}$$

where E_{opt} and l_{opt} are retrieved from the fitted curves shown in Fig. 4.18(a).

The result for $\mathcal{E}_{max}$ is shown in Fig. 4.21(a). From $\mathcal{E}_0 = \frac{m_e c \omega_p}{e}$ one might expect an increase of $\mathcal{E}_{max}$ with n_0, which could not be confirmed for the highest density $n_0 \approx 1.3 \times 10^{19}\,\mathrm{cm}^{-3}$. However, here the error bars are significantly larger than for the lower densities, which is caused by the stronger fluctuation of the electron energy. As already addressed in section 4.4.1.1, the increased fluctuation of the kinetic energy at the highest electron density might be caused by pointing fluctuations which have an increased relevance for higher energy electrons since those electrons cover a longer distance inside the electron spectrometer and thus, experience a larger deviation from the laser axis than lower energy electrons with the same transverse momentum, i.e., the higher energy electrons might not impinge on the scintillating screen and are in this case not detected. Furthermore, higher electron densities

usually cause stronger laser pulse evolutions, which is related to stronger instabilities. Laser pulse evolution in the plasma is investigated in chapter 5.

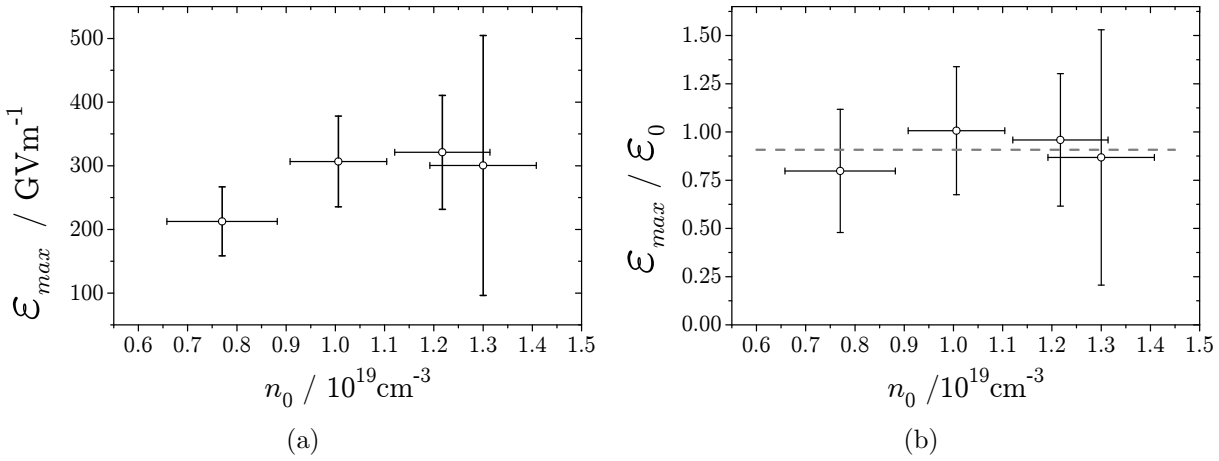

Figure 4.21 *(a) Maximum accelerating electric field $\mathcal{E}_{max}$ experienced by the electrons accelerated to E_{max} with respect to the background electron density n_0. (b) Ratio of $\mathcal{E}_{max}$ to the nonlinear cold wavebreaking limit $\mathcal{E}_0$. The dashed line represents the average of the four data points.*

Additionally, Fig. 4.21(b) shows the ratio of the maximum electric field to the cold non-relativistic wavebreaking limit amounting to $\mathcal{E}_{max}/\mathcal{E}_0 \approx 1$ for all densities, which suggests that the major fraction of the accelerated electrons is injected at the shockfront. Nevertheless, the self injected background charge, e.g. due to transverse wavebreaking should be taken into account for the interpretation of the data. This is especially relevant for the discussion of the energy spread of the accelerated electron bunch in section 4.4.2.1.

4.4.2 Energy Spread and Betatron Oscillations

Monoenergetic and broadband electron energy distributions were obtained. Moreover, the broadband electron energy distributions frequently exhibit energy dependent pointing variations of the electron beam.

Monoenergetic (Fig. 4.22(a)) and broadband (Fig. 4.22(b)) electron energy distributions were frequently observed in the experiment and as demonstrated in Fig. 4.22(c), electron pulses exhibiting both features can also be generated in the same shot. In the following section, the bandwidth of the electron energy distributions will be discussed. Moreover, the broadband electron energy distributions frequently show energy dependent pointing variations of the electron beam which will be investigated in section 4.4.2.2.

4.4.2.1 Energy Spread

The energy spread evolves in dependence on the position of the electron density transition and is probably influenced by the width of the transition w_{SF}, its electron density ratio n_{SF}/n_0 and the deformation of the bubble at the transition, which might affect the electron density distribution of the plasma wave over distances of the order of $100\,\mu$m.

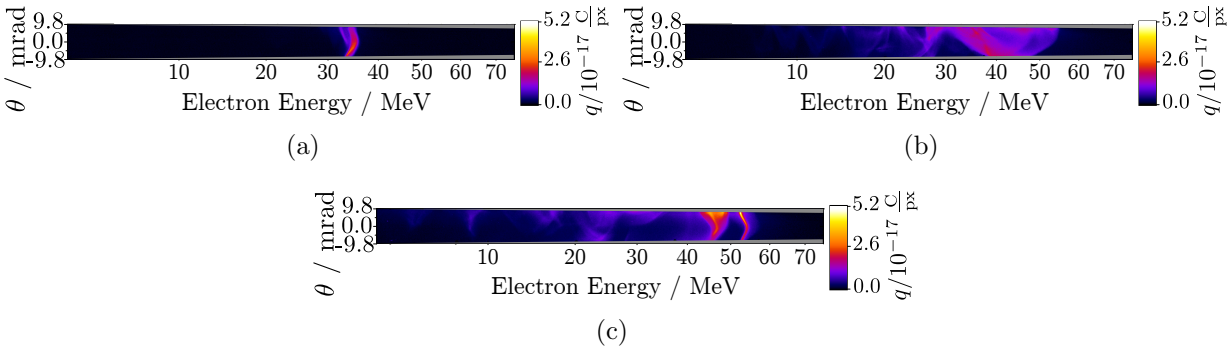

Figure 4.22 *Typical electron energy maps generated in a plasma with a sudden electron density transition. (a) Monoenergetic electron energy distribution, (b) broadband electron energy distribution with energy dependent pointing variations of the electron beam in transverse direction, (c) both features.*

As a consequence of Coulomb repulsion and the reduction of the plasma wave's accelerating field by the accelerated charge, beam loading can lead to a broadening of the electron energy distribution. Generally, the purely monoenergetic electron beams have a lower total charge than the broadband electron energy distributions. In Fig. 4.22 , $|q|_{mono} \approx 1.2\,\mathrm{pC}$, $|q|_{broad} \approx 7.4\,\mathrm{pC}$ and $|q|_{broad,mono} \approx 7.0\,\mathrm{pC}$ and thus, beamloading might contribute to the larger energy spread present in the electron energy maps in Figs. 4.22(b) and 4.22(c). Nevertheless, these electron energy distributions were obtained by the acceleration of electrons in an electron density of $n_0 \approx 7.7 \times 10^{18}\,\mathrm{cm}^{-3}$. In a slightly lower electron density of $n_0 \approx 5.4 \times 10^{18}\,\mathrm{cm}^{-3}$, a threshold above which beamloading influences the energy spread was determined to $\approx 25\,\mathrm{pC}$ [112]. Since here only charges up to $\approx 8\,\mathrm{pC}$ were detected inside the electron spectrometer, beamloading is probably not relevant. However, the acceptance of the electron spectrometer is limited in transverse direction and hence, a significant amount of charge might not be detected, i.e., beamloading as a cause for the broadening of the electrons' energy spread cannot be ruled out entirely.

Fig. 4.23(a) shows that the frequency of occurrence of monoenergetic electron energy distributions decreases for shockfront positions deeper inside the gas jet while the frequency of occurrence of broadband electron energy distributions grows (Fig. 4.23(b)). The experimental investigation of electron injection at a sharp density transition was put forward by [47] and the generation of low energy spread electron bunches was attributed to the injection of the electrons within a width $w_{SF} < \lambda_p$ and thus, the strongly limited duration of the injection process occuring within a strongly limited area in phase space. In the reported experiment, the angle of the shockfront increases with x_{SF}, which increases the effective width of the transition (cf. section 4.2.2). Compared to the minimum width of the shockfront at an angle of 0°, for maximum angles of $\alpha \approx 45°$, an increase of the width by a factor of $\sqrt{2}$ is to be expected. Therefore, the changing width of the transition might contribute

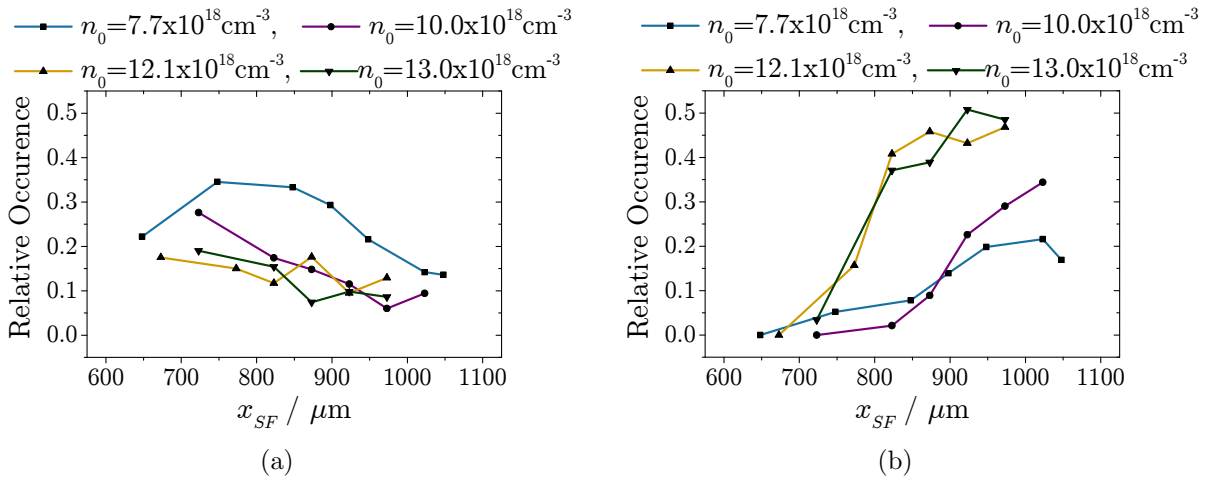

Figure 4.23 *Frequency of occurrence of (a) monoenergetic and (b) broadband electron energy distributions in the electron energy maps. The position of the knife edge x_{KE} is represented by the position of the shockfront $x_{SF} \approx 2x_{KE}$. Note that both features can be generated in the same shot (cf. Fig. 4.22).*

to the evolution of the energy spread. Furthermore, the density ratio n_{SF}/n_0 might play a role. With increasing n_{SF}/n_0 but a constant electron density n_0 in region II, the change of plasma wavelength $\Delta\lambda_p$ is increased and hence, the rear of the plasma wave is slowed down for a longer time, which allows for a longer period of injection. This assumption is supported by the increase of n_{SF}/n_0 with x_{SF} in the experiment. Hence, a convolution of w_{SF} and $\Delta\lambda_p$ might also contribute to the bandwidth of the electron bunches. Unfortunately, with the PIC simulated parameter scan (cf. appendix B.2) neither of the two assumptions could be supported. Calculations in section 4.4.2.2 suggest that the injection process takes place over distances of the order of 100 μm, which is significantly longer than the width of the shockfront $w_{SF} \approx 8\mu$m, i.e., the electrons are possibly not only injected at the shockfront. This continuous injection might be caused by more strongly driven plasma waves at positions deeper inside the plasma in combination with the deformation of the plasma wave at a tilted front (a deformation could be observed in the PIC-simulations, cf. Fig. 4.26(a)), which might influence the behaviour of the plasma wave's electron density distribution at distances significantly larger than $\approx 8\mu$m away from the shockfront and thus, might possibly cause a longer period of injection. Note that the constant γ-factor does not indicate an increase of laser intensity with x_{SF}. However, as already suggested in section 4.2.4.1, the determination of the γ-factor might be not sufficiently accurate for various reasons. Furthermore, discussions in sections 4.4.1.1, 4.4.1.3 and Appendix B.3.1 support the assumption that the laser pulse evolves to higher intensities with increasing position of the shockfront. It has to be emphasised again, that the observation of the evolution of the laser pulse is of enormous importance for the interpretation of the experimental results. A possible method for the

investigation of laser pulse evolution in the plasma is presented in chapter 5.

4.4.2.2 Betatron Oscillations

The energy dependent pointing variations of the electron beam observed in the electron energy maps could be traced back to Betatron oscillations. Moreover, a simple model suggests that the broadband electron distributions are chirped. Results of three-dimensional PIC simulations suggest that the generation of the Betatron oscillations is triggered by a finite angle α of the electron density transition.

Broadband electron energy distributions with periodic energy dependent pointing variations of the electron beam as shown in the electron energy map in Fig. 4.22(b) can be a signature of Betatron oscillations. Such modulations in electron energy maps could be simulated by [113, 114] where a homogeneous background electron density was assumed. Due to the tailored electron density in the experiment presented here, the observed transverse modulations could not be calculated with these models. To incorporate the measured electron density profile, a new model employing equations from [10] (1D, referred to as Model A in the following) and [75] (3D, referred to as Model B in the following) was developed. Strictly speaking, Betatron oscillations are not present in a 1-dimensional plasma wave due to the absence of transverse fields. Nevertheless, the Betatron wavelength λ_β depends on the electron energy and therefore, a mathematical description of the oscillations is possible. Despite their one-dimensional form, the equations employed for Model B describe a three-dimensional acceleration process and represent a mixture of a one-dimensional analytical approach coupled with the results of three-dimensional PIC-simulations. While the calculation is carried out similarly for Model A and B, the exact relations of the phase velocities of the wake as well its maximum electric field differ.

Motion in forward direction. The electric field $\mathcal{E}$ of one period of a nonlinear plasma wave can be approximated with a linear relation (cf. section 2.3.1.2). In the co-moving frame of reference where a position with respect to the co-moving plasma wave is represented by $\xi = x - v_{\Phi,p}t$ with [2]

$$v_{\Phi,p} = c \begin{cases} \sqrt{1-\frac{\omega_p^2}{\omega_0^2}} & \text{for Model A,} \\ (1-\frac{3}{2}\frac{\omega_p^2}{\omega_0^2}) & \text{for Model B,} \end{cases} \tag{4.6}$$

the electric field can be described by

$$\mathcal{E}(\xi) = -\mathcal{E}_{max}\left(1 - \frac{\xi}{\frac{1}{2}\lambda_{p,nl}}\right), \tag{4.7}$$

where $\lambda_{p,nl}$ (cf. section 4.2.4) is the nonlinear plasma wavelength, i.e., $\xi = 0$ is located at the rear of the first plasma wave period and the electrons are accelerated between $\xi = 0$ and

[2] The phase velocity for Model B is obtained by linearly approximating the phase velocity of Model A and incorporating the etching of the front of the laser pulse [75].

$\xi = \lambda_{p,nl}/2$, which represents the position inside the plasma wave where the electrons enter the decelerating region (dephasing) (cf. Fig. 4.25). Furthermore, the maximum electric field of the plasma wave is given by

$$\mathcal{E}_{max} = \mathfrak{f}_{\mathcal{E}}\mathcal{E}_0 \begin{cases} 1 & \text{for} \quad \text{Model A,} \\ \sqrt{a_0} & \quad\quad\ \ \text{Model B,} \end{cases} \tag{4.8}$$

where $\mathcal{E}_0 = m_e c\omega_p/e$ and $\mathfrak{f}_{\mathcal{E}}$ is a fit factor to reduce the accelerating field and will be determined below. The additional factor $\sqrt{a_0}$ for Model B is adopted from [75]. While no standard procedure for the deduction of a_0 from plasma parameters has been established yet, here, a_0 is deduced by equating the blowout radius [75] to one half of the nonlinear plasma wave period investigated in section 4.2.3.2

$$R_{bo} = \frac{\sqrt{a_0}}{\pi}\lambda_p \stackrel{!}{=} 1/2\lambda_{p,nl}, \tag{4.9}$$

since a_0 is only required for Model B. From $\lambda_{p,nl}/\lambda_p = \sqrt{\gamma} \approx 1.1$ (cf. section 4.2.4.1) follows $a_0 \approx 3$.

In the following discussion, electrons are assumed to be injected at the rear of the plasma wave. Hence, the electron energy and therefore γ_{e^-} can be calculated with

$$E = e\int_0^{l_{acc}} \mathcal{E}_{max}(\xi_{e^-})\left(1 - \frac{\xi_{e^-}}{\frac{1}{2}\lambda_{p,nl}}\right)\mathrm{dx} = (\gamma_{e^-} - 1)m_e c^2, \tag{4.10}$$

where ξ_{e^-} is the position of the respective electron inside the plasma wave determined by the relative movement with the velocities $v_{\Phi,p}$ and c, respectively. Note, that γ_{e^-} is the γ-factor of the electrons accelerated inside the plasma wave and does not refer to the γ-factor of the oscillating plasma electrons constituting the plasma wave γ_Φ. For the calculation of the energy gain in the plasma wave, the following assumptions were made:

- continuous injection at the rear of the plasma wave period (cf. section 4.4.2.1),
- since at the time of injection, the injected electrons already have a velocity close to the speed of light c, the electron velocity in the co-moving frame of reference is approximated with $c - v_{\Phi,p}$,
- simultaneous termination of the acceleration process for all electrons such that the phase relation of the electrons is maintained.

Motion in transverse direction. As soon as the electrons leave the longitudinal axis of symmetry of the wakefield, they experience the transverse $\mathcal{E}$-field of the plasma wave

leading to Betatron oscillations with the energy dependent wavelength (cf. section 2.3.5)

$$\lambda_\beta = \lambda_p \sqrt{2\gamma_{e^-}} \,. \tag{4.11}$$

In the case of continuous injection, the wakefield contains low energy electrons at the rear and high energy electrons towards the middle of the first plasma wave period and hence a continuously changing Betatron wavelength. When the electrons are injected with a fixed phase relation with respect to each other – given by the injection with a fixed transverse momentum or a fixed off-axis position in the bubble – they form an electron wave with a phase

$$\Phi_{e^-} = k_\beta x - \omega_\beta t + \Phi_0, \tag{4.12}$$

where dispersion is neglected, i.e., $\omega_\beta = c k_\beta$ for electrons moving with the speed of light. Here, $k_\beta = \frac{2\pi}{\lambda_\beta}$ is the wave number and the constant phase Φ_0 describes the unknown but constant initial conditions determined by the injection process. Assuming a sinusoidal oscillation with a position dependent wave vector, the transverse displacement can be estimated with

$$z(l_{acc,i}) \propto \cos[k_\beta l_{acc,i} - \omega t_{max} + \Phi_0] = \cos[k_\beta (l_{acc,i} - l_{max}) + \Phi_0], \tag{4.13}$$

where each acceleration length $l_{acc,i}$ corresponds to a certain electron energy given by Eq. (4.10). After the termination of the acceleration process, the electrons' oscillatory motion is terminated as the transverse wakefields driving the oscillation are no longer present either. Nevertheless, the structure of the wave remains if the electrons do not experience any additional forces in z-direction. Therefore, Betatron oscillations inside the wakefield might be observed in the electron energy maps as energy dependent pointing variations of the electron beam. Note that oscillations in the horizontal plane are neglected as they could not be resolved with the electron spectrometer.

Reconstructed electron energy distributions. The energy dependent pointing variations of the electron beam observed in the electron energy maps could be reconstructed using Model A as well as Model B, which supports the assumption that these modulations are caused by Betatron oscillations. The left hand side column of Fig. 4.24 shows three different electron energy maps overlayed with white lines, which represent the energy dependent pointing variations of the electron beam calculated with Model A. The same electron energy maps are shown in the right hand side column of Fig. 4.24 overlayed with the transverse modulations calculated with Model B. Note that the amplitude of the calculated modulations shown in Fig. 4.24 is normalised to the angle of acceptance of the electron

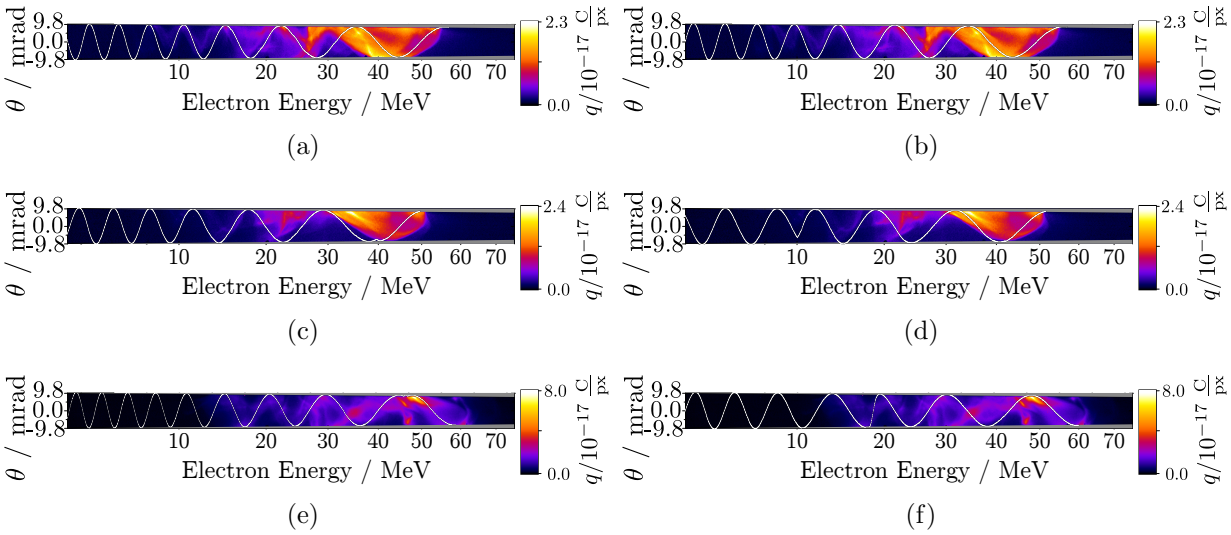

Figure 4.24 *Measured electron energy distributions overlayed with the reconstructed transverse modulations. Left hand side: Model A. Right hand side: Model B.*

spectrometer, which amounts to 9.8 mrad at 3 MeV and decreases to 7.8 mrad at 72 MeV. However, due to phase shifts caused by the density transition, this relative amplitude can be reduced as e.g. in Fig. 4.24(d) at ≈ 10 MeV.

The calculated modulations were adapted to the measured electron energy distributions by varying the position of the onset of injection x_{inj}, the acceleration length l_{acc} and the initial phase Φ_0, which is constant for a given electron energy distribution. The parameters are shown in Table 4.2 for all electron energy maps in Fig. 4.24. For all calculations the accelerating field is reduced by the factor $\mathfrak{f}_{\mathcal{E}} = 0.6$, which influences the phase of the electron wave and thus, the wavelength of the transverse modulations. The reduction of the accelerating field is equivalent to a reduced instantaneous electron energy gain, which simultaneously causes a compression of the Betatron wavelength.

	Model A				Model B			
x_{SF}/μm	Fig.	x_{inj}/μm	l_{max}/μm	Φ_0/rad	Fig.	l_{max}/μm	Φ_0/rad	
1305	4.24(a)	1305	387	-0.2	4.24(b)	1062	208	-0.2
1279	4.24(c)	1279	272	0.2	4.24(d)	1138	176	0.2
791	4.24(e)	791	327	91	4.24(f)	622	228	3

Table 4.2 *Fit parameters used to reconstruct the energy dependent pointing variations observed in the electron energy maps shown in Fig. 4.24.*

Generally, Model A supports the assumption of the onset of injection at the position of the shockfront x_{SF}, which correlates the maximum energy E of a given electron energy distribution to the position of the shockfront. The electron energy maps shown in Figs. 4.24(a) and 4.24(b) were generated in a gas jet with a shockfront at the position $x_{SF} \approx 1305\,\mu$m,

which is identical to the ideal position of injection for Model A while for Model B, the ideal position of injection $x_{inj} = 1062\,\mu$m is located significantly in front of the shockfront. The larger deviation of the assumed onset of injection suggested by Model B might be caused by an inaccurate estimation of a_0, which was deduced using the γ-factor investigated in section 4.2.4.1 as well as equations from [75].

Since the reconstructed electron energy distributions represent the electrons' distribution at the end of the acceleration process, the electrons' position (blue line) inside the bubble (red line) can be visualised as shown in Fig. 4.25. Due to the electrons position close to the

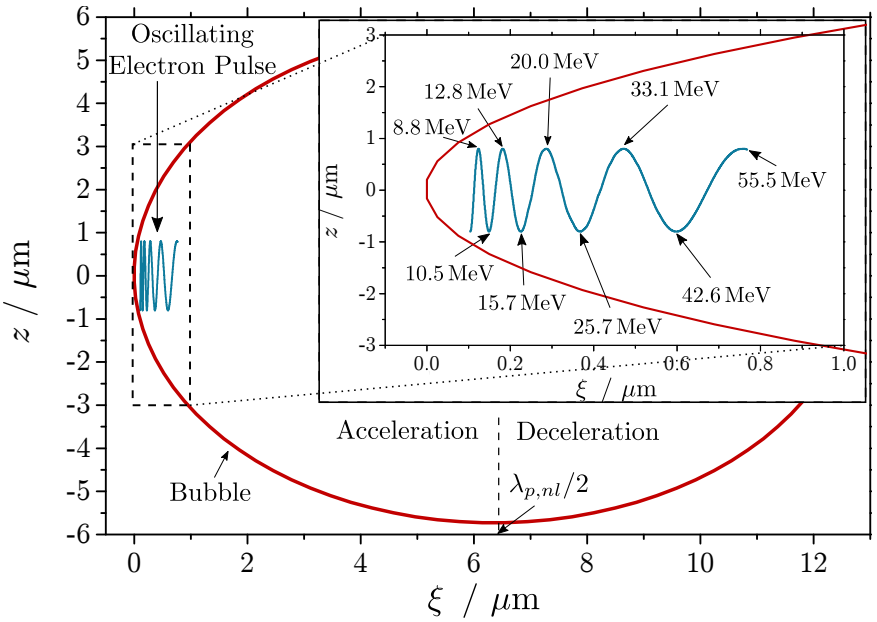

Figure 4.25 *With the calculated electron wave (blue) at the end of the acceleration process, each longitudinal position of the bubble (red) can be correlated to an electron energy.*

rear of the bubble, the inset into Fig. 4.25 shows the area inside the black dashed frame in a different scale. Each part of the electron wave corresponds to a certain electron energy, i.e., it is possible to correlate a longitudinal position inside the bubble to an electron energy. The measurement and analysis of the energy dependent pointing variations provides information on the chirp and the longitudinal density distribution of the electron pulse which is an important information for the application of the LWFA electrons e.g. for a free electron laser. Note that comparisons of this kind usually require PIC-simulations, while here, only a simple calculation was carried out.

Generation at the shockfront. The generation of the energy dependent pointing variations of the electron beam could be investigated with three-dimensional PIC-simulations. A possible reason for the periodic pointing variations in the broadband electron energy distributions is the angle of the shockfront α, which continuously increases with x_{SF}. This assumption is supported by the default simulation ($a_0 = 2$, $\alpha = 22.5°$, $w_{SF} = 5\,\mu$m and $n_{SF}/n_0 = 2$ with $n_0 = 7.7 \times 10^{18}\,\mathrm{cm}^{-3}$) where the plasma wave is severely deformed at the tilted electron density transition (cf. Fig. 4.26(a)) leading to injection with an initial trans-

verse momentum. The corresponding electron electron energy map (Fig. 4.26(b)) shows a periodic modulation in transverse direction. A different scenario can be observed for the

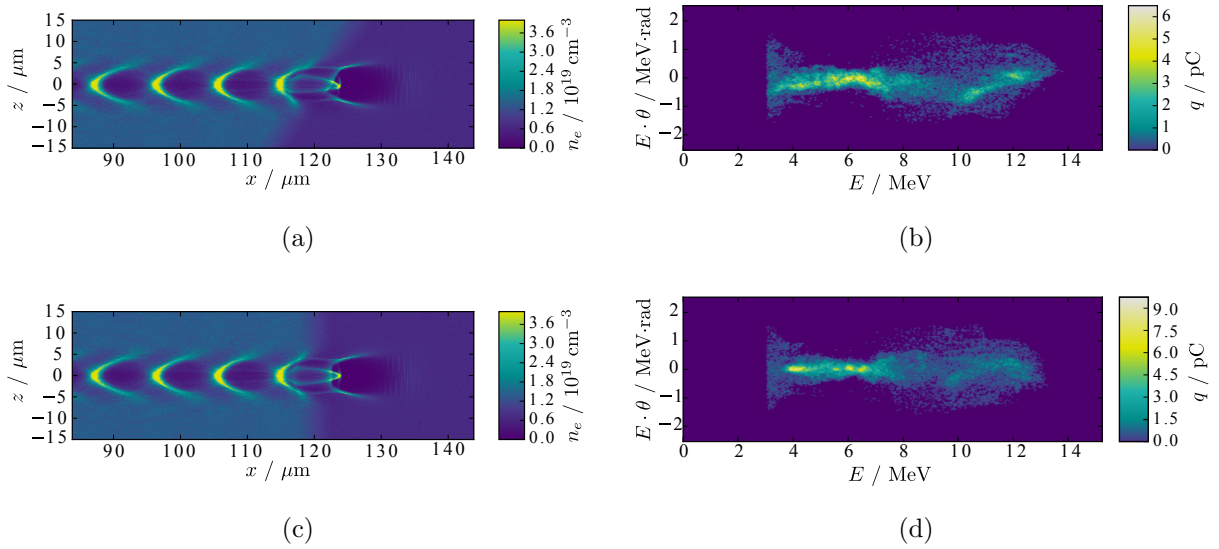

Figure 4.26 *Simulated electron density maps (left hand side) and electron energy maps (right hand side). (a), (b)* $\alpha = 22.5°$*. (c),(d)* $\alpha = 0°$*.*

simulation with $\alpha = 0$ where the other parameters were kept at the default values. Although of-axis injection can be observed in the electron density map shown in Fig 4.26(c), the electron energy map (Fig. 4.26(d)) does not show a transverse modulation with a clear phase relation as in Fig. 4.26(b).

5. Towards the Indirect Observation of the Laser Pulse Evolution in a Plasma

Due to the small temporal (fs) and spatial (μm) scales relevant for laser wakefield acceleration, the observation of the underlying processes is challenging. Nevertheless, the observation of the interaction is required to gain deeper insight and thus, to have the chance to improve the accelerator output with respect to e.g. stability, energy or charge. By means of shadowgraphy with an ultra short probe beam [52], the evolution of the plasma wave was investigated. Moreover, magnetic fields in the region of interaction – inextricably connected to LWFA – were explored using polarimetry [48, 56, 58, 108]. The combination of both methods allows for a more detailed investigation of the evolution of plasma wave and laser pulse.

In this chapter, the change of polarisation of an ultrashort probe pulse in the region of interaction of laser pulse and plasma wave is investigated at different times during the interaction. The evolution of the polarisation signals suggests that besides a rotation of the plane of polarisation ψ (induced by the Faraday effect), a phase shift δ possibly as a consequence of the Cotton-Mouton effect is accumulated by two perpendicular polarisation components of the probe beam in the region of interaction. Moreover, the investigation of PIC-simulated rotation maps shows that the magnetic field of the main laser pulse might play a major role for these changes of polarisation.

5.1 Probe Beam and Magnetic Fields

Initially, the probe pulse is linearly polarised. Nevertheless, the strong magnetic fields in the region of interaction can change the probe pulse's state of polarisation via the Faraday effect and the Cotton-Mouton effect.

In the experiment, a laser pulse propagating in x-direction drives a plasma wave in which electrons can be accelerated close to the speed of light. Moreover, a probe pulse initially polarised in x-direction propagates through the region of interaction along $-\vec{e}_y$. In Fig. 5.1, the main laser pulse shown in green is represented by its oscillating magnetic field $\mathcal{B}_L$ while the ultra-short probe pulse is illustrated in red in terms of its initial electric field $\vec{\mathcal{E}}_{init}$. The azimuthal magnetic field B_φ (olive) of the plasma wave (its electron density distribution is indicated by the blue line) and the accelerated electrons (dark blue dots) has a field component $\mathcal{B}_\parallel$ parallel to the direction of propagation of the probe pulse, i.e., it can rotate

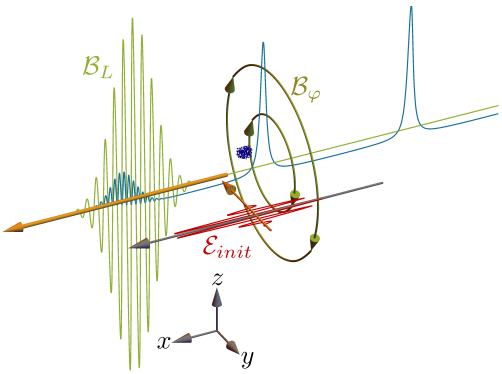

Figure 5.1 *The plasma wave's on-axis electron density distribution (blue line) and the accelerated electron pulse (dark blue dots) are surrounded by an azimuthal magnetic field $\mathcal{B}_\varphi$ (olive circles), which in z-direction overlaps with the oscillating magnetic field $\mathcal{B}_L$ of the main laser pulse (green oscillating line). In those magnetic fields, the state of polarisation of the ultrashort probe beam (red oscillating line) can be changed.*

the plane of polarisation of the probe pulse (Faraday effect). This process can then generate an electric field component of the probe pulse in z-direction. In the magnetic fields $\mathcal{B}_\perp$ perpendicular to the direction of propagation of the probe pulse, which are provided by the the azimuthal magnetic field as well as the main laser pulse in z-direction, the probe pulse's electric field components in x and z-direction can be shifted in phase with respect to each other (Cotton-Mouton effect). Faraday effect and Cotton-Mouton effect are explained in section 2.3.6.

5.2 Evolution of the Polarisation Signal Type

Different types of the polarisation signal could be observed at different times during the interaction. While the signal types observed early during the interaction have already been discussed in the literature, the signal types appearing later during the interaction have never been observed before in laser wakefield acceleration experiments.

Due to the propagation of the main laser pulse through the plasma in $\vec{e}_x$-direction, the region of interaction moves and the investigation of the interaction at different times during the interaction requires the observation of different positions inside the plasma. These positions are given by $x = v_{g,L}t$ where $v_{g,L}$ is the group velocity of the main laser pulse and t the time elapsed since the laser pulses has entered the plasma, i.e., time and position are directly connected.

In the reported experiment, the interaction taking place inside a plasma with a length of $\approx 2.1\,\mathrm{mm}$ is probed between the positions $x \approx 500\,\mu\mathrm{m}$ and $x \approx 2000\,\mu\mathrm{m}$ in steps of $\Delta x \approx 71\,\mu\mathrm{m}$. At each position, 100 data sets consisting of two polarograms and an electron energy map were recorded. Data sets showing a clear plasma wave in both polarograms as well as a total charge $> 6\,\mathrm{pC}$ detected with the electron spectrometer were analysed with respect to the probe beam's change of polarisation. Since the plasma wave is located in the region of interaction, an image of a clear plasma wave in a shadowgram or polarogram suggests that the region of interaction is imaged sharply. Moreover, with increasing charge of the accelerated electron pulses, the chance of detecting a signature of their magnetic field increases.

In the experiment, polarisation signals with different overall shapes or signal types could be observed. Each signal type 1-5 shown in Fig. 5.2 appears at a specific time during the interaction for the first time. The time of first appearance is displayed in the upper left corners of each image represented by the position $x = v_{g,L}t$. Signal type 1 can be observed

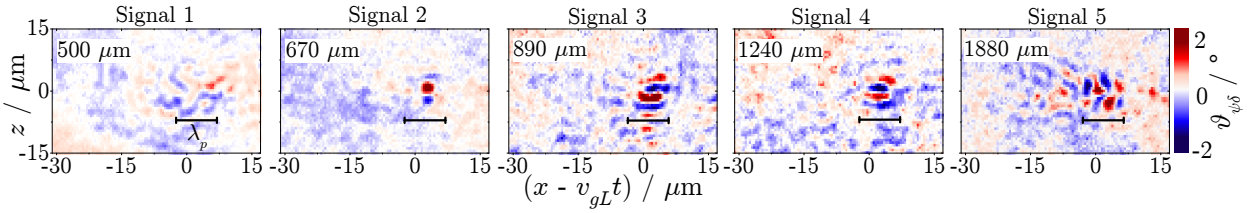

Figure 5.2 *Typical polarisation signal types with the time of first appearance given by $x = v_{g,L}t$ in the upper left corner of each image. Moreover, the black line illustrates the plasma wavelength $\lambda_p \approx 9.4\mu m$.*

for the first time at $v_{g,L}t \approx 500\,\mu$m, type 2 at $v_{g,L}t \approx 670\,\mu$m etc. until type 5 appears at $v_{g,L}t \approx 1880\,\mu$m. Despite the appearance of a new signal type, formerly observed signals can still be generated at those later times. Assuming that a specific signal type represents a specific stage during the interaction, the increase of observable signal types can be attributed to the nonlinear nature of laser plasma interaction and is in that context a signature of slower and faster evolutions of the interaction, i.e., signal 2 observed at $v_{g,L}t \approx 670\,\mu$m corresponds to a fast evolution while the same signal appearing later during the interaction – for instance at $v_{g,L}t \approx 1000\,\mu$m – is the consequence of a slower evolution.

Signal types 1 and 2 were discussed in [57, 58] and [29, 56], respectively. While signal type 1 was attributed to the magnetic fields present due to the generation of a wakefield, signal type 2 was traced back to the magnetic fields of the accelerated electrons and the plasma wave. Nevertheless, both signals were explained by Faraday rotation in the parallel magnetic field components $\mathcal{B}_{\parallel}$ of the plasma wave and the accelerated electrons. At later times during the interaction, the polarisation signal becomes more and more complex (signal types $3-5$) and develops an alternating sense of rotation in propagation direction of the main beam with sub-λ_p length scales (signal type 5). On average, the plasma wavelength in this experiment was $\lambda_p \approx 9.4\,\mu$m. Those small scales could only be resolved due to the high temporal and spatial resolution of the probe beam and its imaging system (cf. section 3.4) and have therefore, never been observed before within the framework of laser wakefield acceleration.

The Faraday effect is caused by magnetic fields which are oriented parallel to the propagation direction of the probe pulse and the sense of the rotation of the plane of polarisation depends on the sign of these magnetic fields. In this experimental configuration, the parallel magnetic fields are a component of the azimuthal magnetic fields surrounding the plasma wave as well as the accelerated electron pulse and the sign of the magnetic field is given by

the direction of movement of plasma wave and the electron pulse. Therefore, an alternating sign of the angle of polarisation rotation in propagation direction of the main pulse would require an alternating direction of current which is not to be expected in this experiment. An explanation for the alternating sense of rotation is presented in the following section.

5.3 Contributions of Rotation ψ and Phaseshift δ to the Retrieved Angle $\vartheta_{\psi,\delta}$

The signal types appearing early during the interaction can be explained using the Faraday effect alone whereas the alternating sense of rotation in propagation direction of the latest signal might be caused by an interplay of Faraday rotation and a phase shift generated as a consequence of the Cotton-Mouton effect.

To explore the generation of signal type 5 (cf. Fig. 5.2) or more precisely, the alternating sense of rotation of $\vartheta_{\psi,\delta}$ in propagation direction of the main beam, we will now take a closer look on the data analysis method presented in section 3.4.2.1. Therefore, the retrieved angle $\vartheta_{\psi,\delta}$ is examined in two scenarios – S1 and S2 – with the help of one-dimensional, predetermined distributions of $\psi(x)$ and $\delta(x)$, which are shown in Fig. 5.3(a). $\psi(x)$ and $\delta(x)$ represent the distributions of the angle of Faraday rotation and the phase shift in main pulse propagation direction x accumulated along the probe beam's path through the plasma, i.e., along $\vec{e}_y$. While different phase shift distributions $\delta(x)$ are employed in S1 and S2, both scenarios use identical distributions of the angle of rotation $\psi(x)$. The amplitude of the angle of Faraday rotation $\psi(x)$ was adapted to the results presented in Fig. 5.2 and the FWHM length of $\psi(x)$ was set to $\lambda_p = 9.4\,\mu$m, which was chosen to generate a polarisation signal similar to signal 2 and signal 5 from the same distribution $\psi(x)$. Moreover, the phase shift $\delta(x)$ for scenario S2 was adapted such that in combination with $\psi(x)$ a signal similar to signal 5 could be generated.

In both cases, the intensity distributions I_R and I_T are computed with Eq. 3.1, where $\beta_T = \beta_R = 1$, $\psi_T = 75.0°$ and $\psi_R = 108.6°$. The angle $\vartheta_{\psi,\delta}$ (Fig. 5.3(c)) is then retrieved by inverting the intensity ratio $\frac{I_T}{I_R}(\psi,\delta)$ (Fig. 5.3(b)) under the assumption $\delta = 0$, which is the standard procedure applied to the experimental data. In Fig. 5.3, S1 and S2 are represented by black solid or dashed orange lines, respectively.

In regions of changed polarisation, the intensity ratio calculated for scenario 1 where $\delta = 0$ is increased with respect to regions of initial polarisation. The retrieval of $\vartheta_{\psi,\delta}$ from the uniform distribution $I_T/I_R(\psi, \delta = 0)$ results in a uniform distribution identical to the input parameter $\psi(x)$. In contrast, the intensity distribution calculated for scenario 2 where δ ranges between 0° and 180° is an alternating brightness modulation with respect to regions of initial polarisation, which is transferred to $\vartheta_{\psi,\delta}$ in the form of an alternating

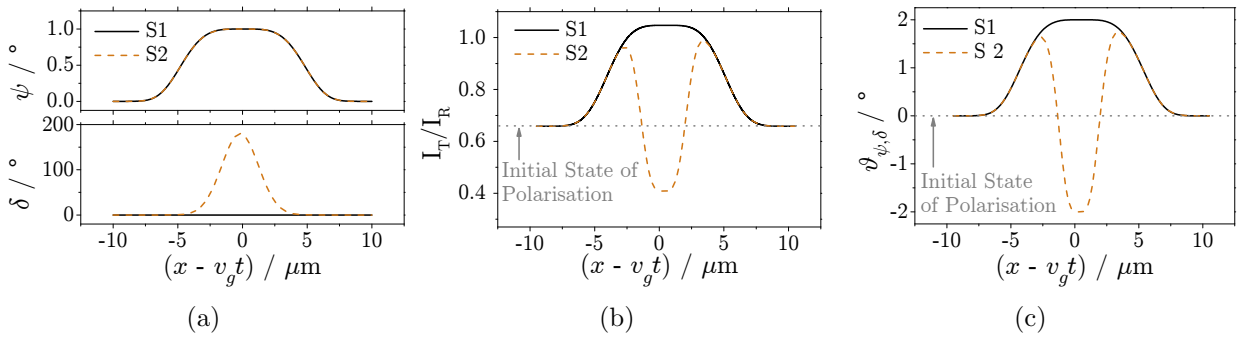

Figure 5.3 *(a) Predetermined distributions of the angle of rotation ψ and phase shift δ. (b) Intensity ratios. (c) Rotation of the major axis of the polarisation ellipse $\vartheta_{\psi,\delta}$.*

sense of rotation.

While scenario 1 supports the assumption that signal types 1 and 2 (cf. Fig. 5.2) are generated by Faraday rotation in the parallel magnetic fields $\mathcal{B}_{\parallel}$ of the plasma wave and the accelerated electrons, the results for scenario 2 suggest that the more complex signal types (3-5) might be additionally influenced by a phase shift, which possibly arises from the perpendicular magnetic fields $B_{\perp}$ of plasma wave, accelerated electrons as well as the laser pulse (Cotton Mouton-effect). Especially, the alternating sense of rotation of $\vartheta_{\psi,\delta}$ in propagation direction of the main beam in signal 5 can be explained by scenario 2. Note that an influence of the Cotton-Mouton effect has never been observed before in laser wakefield acceleration experiments.

5.4 Three-Dimensional Particle in Cell Simulations

The electric fields of a PIC-simulated probe beam propagating through the region of interaction, which takes place in a three-dimensional simulation box were post processed to obtain artificial polarograms and rotation maps.

With the help of three-dimensional PIC simulations, the origin of the complex polarisation signals is further investigated. In the simulations carried out with EPOCH [96] by Evangelos Siminos from the University of Gothenburg, the interaction of main pulse and plasma takes place in a $(150\times70\times70)\,\mu\mathrm{m}^3$ box with a cell size of $(0.056\times0.133\times0.133)\,\mu\mathrm{m}^3$. Each cell contains two macro particles representing the electron density distribution with a rising edge of a few $100\,\mu\mathrm{m}$ at the front and a plateau of $n_0 = 1.7\times10^{19}\,\mathrm{cm}^{-3}$. The parameters of main and probe pulse propagating in x-direction and $-y$-direction, respectively are listed in Table 5.1.

To simulate optical probing, at different times during the simulated interaction, a probe pulse enters the simulation box. During the probe pulse's propagation through the plasma, the movement of the simulation box is stopped while the propagation of the main pulse is continued. After the probe pulse has passed the region of interaction, the probe fields

Main pulse	
Pulse duration	36 fs
Diameter of focus	18.8 μm
Peak intensity	2.5×10^{18} W/cm^2
Central wavelength	810 nm
Position of focus	300 μm
Probe pulse	
Central wavelength	750 nm
Pulse duration	chirped: 12 fs
	Fourier limited: 4.4 fs

Table 5.1 *Parameters of main and probe pulse in the simulation and the experiment.*

obtained from the PIC simulation are extracted and post-processed [105] on the basis of the paraxial approximation and the thin lens approximation applied to a $4f$-imaging system as illustrated in Fig. 5.4. In a $4f$-system, object plane (O_{4f}), first lens ($L1$), Fourier plane (F), second lens ($L2$, identical to $L1$) and image plane I_{4f} are arranged in this order with a distance f between adjacent elements where f is the focal length of the lenses. Due to the

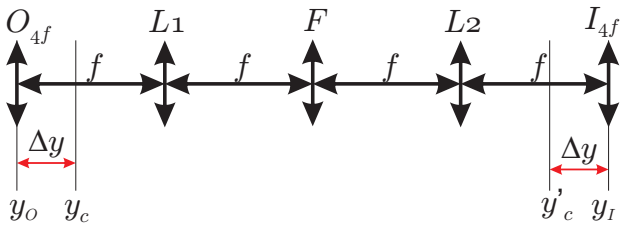

Figure 5.4 *The symmetry of the $4f$ imaging setup is advantageous for the calculation of the image.*

symmetry of the $4f$-system, the fields of the probe beam located at $y_c = y_O + \Delta y$ between the object plane and first lens are identical to the probe beams field after its propagation to the position $y'_c = y_I - \Delta y$ except for a reversal of the field with respect to the x- and z-axes (reversal of image) and a constant phase factor. Hence, the propagation of the probe beam through the optical elements can be replaced by a back-propagation to the object plane in vacuum. Note that the object plane is usually set to the centre of the plasma wave. Since in the back propagation procedure, the aperture in the Fourier plane F is neglected, an aperture with a diameter D is modelled by eliminating all field components with a transverse wave vector $k_\perp = \sqrt{k_x^2 + k_z^2} > \omega D/(2cf)$ in Fourier space. Subsequently, the portion of the filtered field transmitted through a polarizer set to an angle ψ_R or ψ_T is computed. To image the probe beam, it is back propagated in vacuum to the object plane where the intensity integrated in propagation direction results in a polarogram. Rotation maps are generated from the polarograms as described in section 3.4.2.1 for the experimentally obtained data.

Further analysis of the PIC-simulated data (e.g. in section 5.7) was carried out by the author of this thesis.

5.5 Polarisation Signals Generated from the Electric Field of the PIC-Simulated Probe Beam

The evolution of the PIC-simulated polarisation signals is comparable to the experimental results.

Fig. 5.5 compares the PIC-simulated (top) and the experimentally (bottom) obtained polarisation signals . While the interaction proceeds more rapidly in the simulation, which is indicated by the difference in $v_{g,L}t$, the evolution of the signal's shape is similar. Therefore,

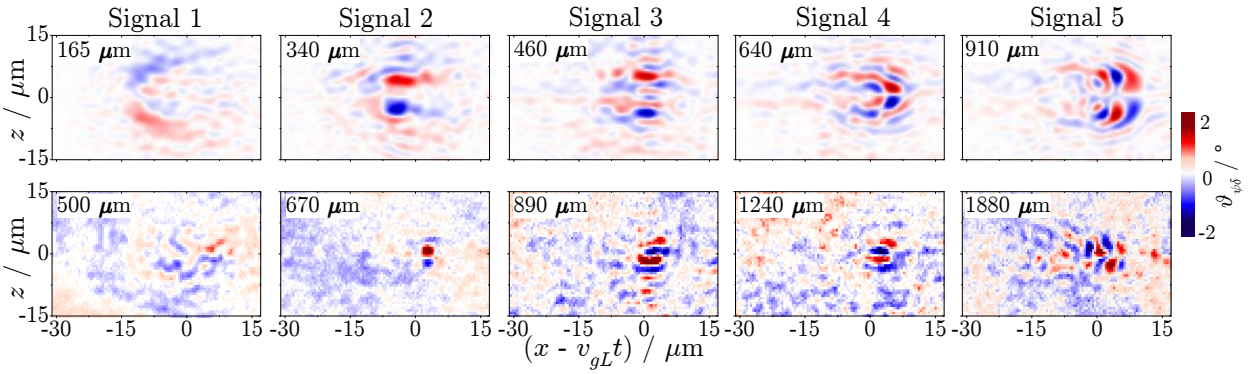

Figure 5.5 *Typical polarisation signals of (top) simulation and (bottom) experiment. Each signal type appears for the first time at a specific time during the interaction given by $x = v_{g,L}t$ in the upper left corner of each image.*

the generation of the alternating sense of rotation of $\vartheta_{\psi,\delta}$ in signal 5 will be analysed in more detail with the PIC-simulated data. Note that in the simulation, electrons are injected at $v_{g,L}t \approx 800\,\mu$m whereas polarisation signals are already present at $v_{g,L}t \approx 165\,\mu$m. Hence, the polarisation signal cannot be regarded as a reliable indicator for injected electrons. The contribution of the accelerated electrons will be further discussed in the following section.

5.6 Source of the Polarisation Signal

Since the alternating signal is generated at the front of the plasma wave where also the laser pulse is situated, a phase shift generated as a consequence of the Cotton-Mouton effect is most likely caused by the strong magnetic fields of the laser pulse.

To generate a rotation map showing the final state of polarisation, the probe beam has to propagate through the whole region of interaction. Consequently, from a probe beam that has passed through only a fraction of the region of interaction, an intermediate rotation map is obtained. The study of different stages in the generation of a polarisation signal helps to localise the source of the signal. Fig. 5.6 shows four steps in the generation of signal type 5. Here, the bottom images in (a) and (b) are identical to the top images in (b) and (c), respectively to visualise the differences of the images corresponding to the different times during the generation of signal 5. The images in greyscale show the electron

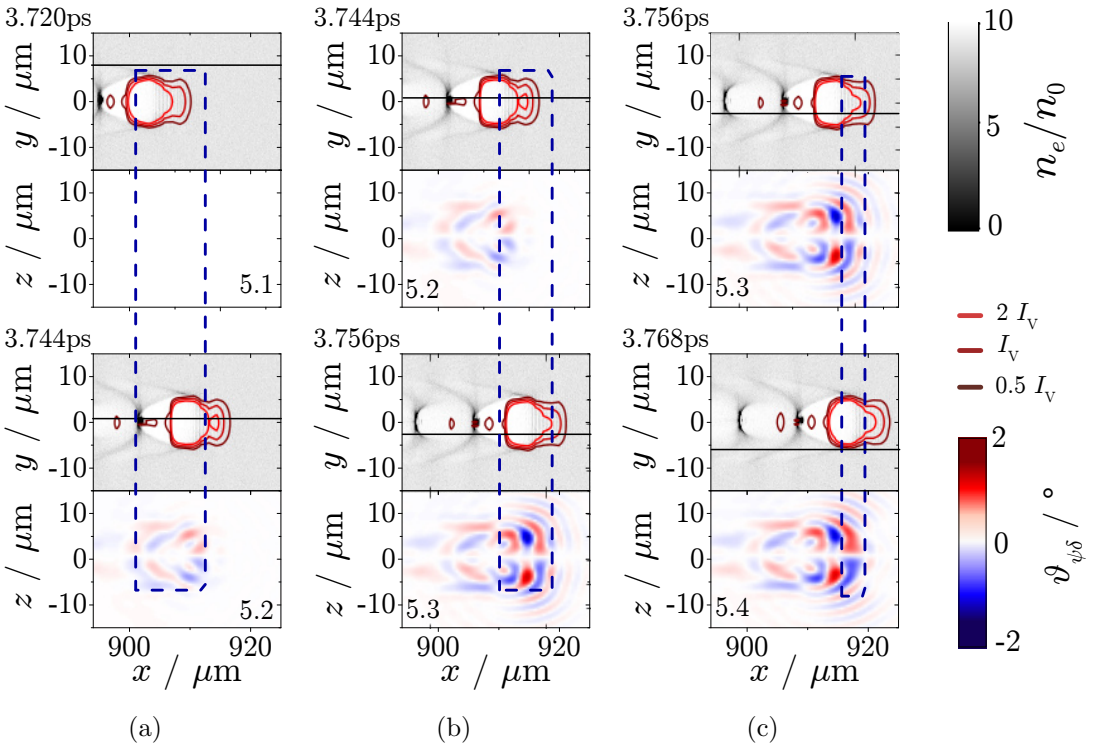

Figure 5.6 *Step by step generation of signal type 5 from the PIC-simulated electric field of the probe pulse. Density maps of the electron density distribution at the centre of the plasma wave are shown in greyscale. They are overlayed with the intensity contours of the laser pulse in red and with a black solid line representing the position of the centre of the probe pulse at the respective time. Note that the probe pulse propagates in $-y$-direction. Underneath each density map, rotation maps generated from the electric fields of the probe pulse at the same time are shown in a red-blue colour scale. The dashed boxes emphasise the propagation of the plasma wave and the main laser pulse while the polarisation signal is generated step by step. Note that the bottom images of (a) are identical to the top images of (b) and the bottom images of (b) are identical to the top images of (c). The images are arranged in this configuration to visualise the differences between the images corresponding to the different times during the generation of signal type 5.*

density distribution in the central plane ($z = 0$) of the plasma wave overlayed with red lines representing the intensity contours of the laser pulse at $0.5I_V$, I_V and $2I_V$ with I_V being the vacuum focus intensity. Moreover, the position of the centre of the probe pulse which propagates in $-y$-direction is shown as a horizontal solid black line. At the time $t_1 = 3.720\,\text{ps}$ (Fig. 5.6(a), top), the probe pulse arrives at the region of interaction, at the time $t_2 = 3.744\,\text{ps}$ (Fig. 5.6(a), bottom; Fig. 5.6(b), top) the probe pulse approaches the centre of the plasma wave ($y = 0$), at the time $t_3 = 3.756\,\text{ps}$ (Fig. 5.6(b)), bottom; Fig. 5.6(c), top) the probe pulse has just passed the centre of the plasma wave and at the time $t_4 = 3.768\,\text{ps}$ it leaves the accelerating structure (Fig. 5.6(c), bottom). Note that the main pulse and the plasma wave propagate in x-direction while the probe pulse propagates through the region of interaction in $-y$-direction, i.e., in the plane for the upper images but out of the plane for the simulated polarograms. The rotation maps generated from the

probe pulse's electromagnetic field at the times $t_1 \dots t_4$ are shown underneath the respective density map and are labled as 5.1 to 5.4. At the time t_1, the probe pulse is still in its initial state of polarisation. However, at $t = t_2$, a low amplitude signal has built up. While the rear part of the signal has not significantly changed at the time $t = t_3$, the signal's front part has developed a larger amplitude and an alternating sense of rotation in x-direction. At the time t_4, the signal is fully developed and its front is slightly elongated with respect to signal 5.3

The longitudinal extent of signal 5.2 in Fig. 5.6(a) is framed with a dashed box, which helps to correlate the probe pulse's and the plasma wave's propagation during the signal's generation. Between $t = t_1$ and $t = t_2$, the probe pulse propagates through the upper wall of the plasma wave, which is the source of the rear part of the polarisation signal. In rotation map 5.3 (Fig. 5.6(b)), the front part of the polarisation signal is framed with a dashed box. In the time span between t_2 and t_3, the probe pulse propagates through the centre of the plasma wave and the position of the alternating polarisation signal is correlated to the front of the plasma wave. Finally, when the probe pulse propagates through the bottom wall of the plasma wave, the signal is not significantly changed anymore.

The contribution of the rear part of the plasma wave where the accelerated electrons are situated between t_1 and t_4 seems to be marginal. Nevertheless, the upper and the lower bubble walls influence the signal at the outer x-positions. This is caused by the dependence of Faraday effect and Cotton-Mouton effect on the electron density, which inside the bubble (where the accelerated electrons are located) is very low compared to the walls of the bubble. Most importantly, the generation of the alternating front signal seems to be related to the front of the plasma wave where also the laser pulse is situated. Therefore, a possible influence of the Cotton-Mouton effect would be dominated by the magnetic field of the laser pulse, which is approximately one order of magnitude larger than the transverse component of the magnetic field of the plasma wave. Note that the fast oscillating magnetic field of the main laser pulse influences the probe pulse's state of polarisation as the the phase shift δ is proportional to $\mathcal{B}_\perp^2$, i.e., it is not averaged out.

5.7 Interplay of Faraday Effect and Cotton-Mouton Effect

The interplay of Faraday effect and Cotton-Mouton effect is investigated by means of coupled differential equations and PIC simulated data present at the time of generation of signal type 5.

The interplay of the Faraday effect and the Cotton-Mouton effect is discussed with the

help of [95]

$$\mathrm{d}\chi = \frac{1}{2}\sin(2\psi)\mathrm{d}\delta, \tag{5.1}$$

and

$$\mathrm{d}\vartheta_{\psi,\delta} = \mathrm{d}\psi_{FR} - \frac{1}{2}\tan(2\chi)\mathrm{d}\delta, \tag{5.2}$$

which describe the incremental ellipticity $\mathrm{d}\chi$ as well as the incremental angle of the rotation of the polarisation ellipse $\mathrm{d}\vartheta_{\psi,\delta}$. Moreover, $\mathrm{d}\psi = \frac{e}{2m_e c\, n_{cr}} \frac{n_e}{\gamma} \vec{\mathcal{B}}_{\parallel} \mathrm{d}y$ is the incremental angle of Faraday rotation and $\mathrm{d}\delta = \frac{e^2}{2m_e^2 c\, n_{cr} \omega_0} \frac{n_e}{\gamma} B_{\perp}^2 \mathrm{d}y$ is the phase shift caused by the Cotton-Mouton effect (cf. section 2.3.6). The coupled differential equations (5.1) and (5.2) are solved with the help of the PIC-simulated data at the time $t = 3.770\,\mathrm{ps}$ corresponding to the time of generation of signal type 5, which as shown in Figs. 5.5 and 5.12(b) exhibits an alternating sense of rotation in the direction of propagation of the main pulse. In contrast to those polarisation signals obtained by postprocessing the PIC-simulated probe pulse's electric fields (cf. top images in Fig. 5.5 or Fig. 5.12(b)), quasistatic distributions of the electron density n_e, the electrons' γ-factor as well as the magnetic fields $\mathcal{B}_{\parallel}$ and $\mathcal{B}_{\perp}$ are used for the present calculations. While the simultaneous propagation of the probe pulse and the main laser pulse as well as the plasma wave under 90° is incorporated, the pulse duration of the probe pulse is neglected for the following considerations. As in the PIC-simulation, the probe pulse propagates in $-y$-direction and thus, the polarisation signal is observed in the $x-z$-plane, where x is the direction of propagation of the main pulse and the plasma wave.

5.7.1 Faraday Effect

The Faraday effect alone does not cause an alternating sense of rotation of the polarisation signal.

To calculate the pure angle of Faraday rotation, the perpendicular magnetic fields are neglected, i.e., $\mathcal{B}_{\perp} = 0$ and thus, $\mathrm{d}\delta = 0$ and $\mathrm{d}\chi = 0$ such that $\mathrm{d}\vartheta_{\psi,\delta} = \mathrm{d}\psi_{FR}$. As a representation of the three-dimensional distribution of $\mathrm{d}\psi$, Fig. 5.7(a) shows the slice

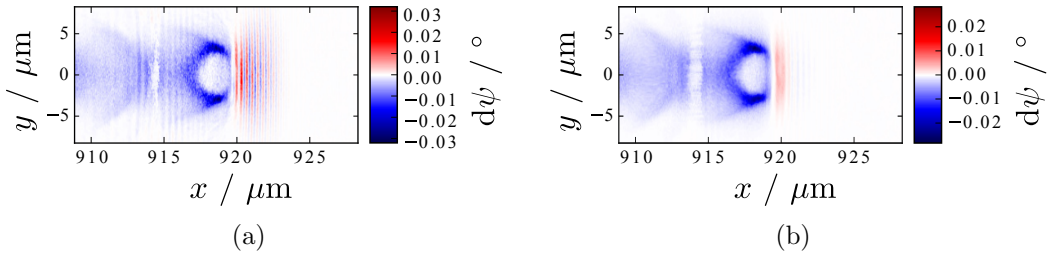

Figure 5.7 *Incremental angle of Faraday rotation $d\psi$ in the plane $z = 4.67\mu m$. (a) Original distribution. (b) Effective distribution.*

$z = 4.76\,\mu\mathrm{m}$ since at the line $z = 4.76\,\mu\mathrm{m}$, the amplitude of signal 5 (cf. Fig. 5.12(b)) is

maximum. While the shape of the distribution of dψ is strongly related to the electron density distribution n_e of the plasma wave, its sign is determined by the sign of the parallel magnetic field $\mathcal{B}_\parallel$, i.e., the oscillating sign at the front of the bubble structure of dψ is caused by $\mathcal{B}_\parallel$. From section 5.1 it is known that $\mathcal{B}_\parallel$ is generated by the particle currents of plasma wave and the accelerated electrons as well as the displacement currents induced by the temporally varying electric fields of the plasma wave. The oscillating sign at the front of the bubble structure of dψ is most likely dominated by displacement currents which at this position might be a consequence of the small scale charge separation of the order of the laser wavelength as a result of the electrons' oscillation in the electric field of the main pulse. The fast oscillations at the front of the bubble structure in Fig. 5.7(a) are averaged out and do not contribute to ψ. The effective distribution of dψ is shown in Fig. 5.7(b).

The generation of the final angle of Faraday rotation ψ is illustrated in Fig. 5.8 where ψ and dψ are shown in a red-blue colour scheme, which represents positive and negative values, respectively. The exact length and colour scales are shown in Figs. 5.7(b) and 5.10(a). If dψ was a static field structure, the probe beam would propagate parallel to the

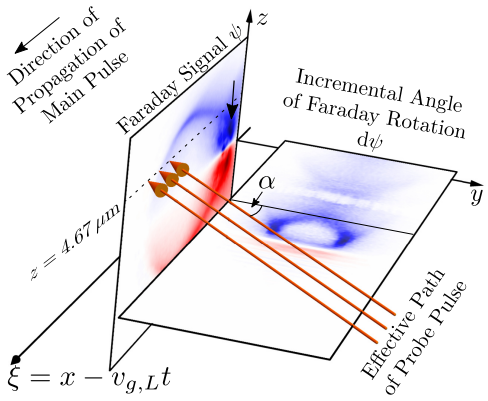

Figure 5.8 *The integration of the incremental angle of Faraday rotation dψ along the probe beams path (orange arrows) is an estimate of the pure angle of Faraday rotation ψ. The exact length and colour scales are shown in Figs. 5.7(b) and 5.10(a).*

solid black line on top of $d\psi$ and the sign of $d\psi$ would be directly transfered to the Faraday signal ψ. Nevertheless, the probe pulse propagates under 90° with respect to the main pulse and the plasma wave and all components move with approximately $v_{g,L}$. Therefore, the probe beam's effective path (orange arrows) through dψ is tilted by the angle $\alpha = 45°$ and each component of the probe beam that has passed the positive (red) field structure of dψ subsequently propagates through a region of negative values (blue). Due to the comparably low amplitude of the positive field structure at the front, the final angle ψ is purely negative at positions $z > 0$ and does not show an alternating sense of rotation in the direction of propagation of the main pulse as present in the post processed signal (cf. Fig. 5.12(b)). A further fundamental difference to the polarisation signal obtained by postprocessing the electric fields of the probe pulse is the large contribution of the peak at the rear of the first plasma wave period to ψ, which in Figs. 5.8 and 5.10(a) is marked with a

black arrow. In the PIC-simulation, probe light is scattered at the strong density gradients of the plasma wave and since in the post processing procedure an aperture is used to filter this scattered light, it does not contribute to the detected signal. Note that the aperture used in the post processing procedure is adapted to the aperture of the optics employed in the experiment. Nevertheless, Eqs. (5.1) and (5.2) do not account for the scattering of light at density gradients. Fig. 5.9 compares the lineout of signal 5 (blue) at the position $z = 4.76\,\mu$m to the lineout of ψ (black) at the same position. It should be noted that the amplitude of the polarisation signal obtained by solving Eq. (5.2) is significantly lower than the amplitude obtained from the PIC-simulated electric fields of the probe pulse. This issue will be addressed below.

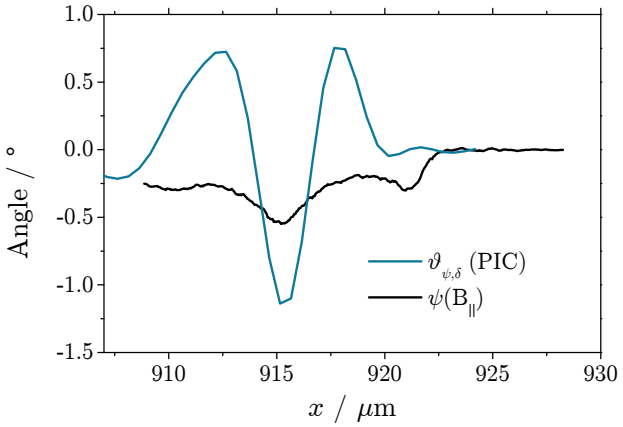

Figure 5.9 *Comparisson of the lineouts of signal type 5 at the position $z = 4.67\,\mu$m obtained from postprocessing the PIC-simulated electric field of the probe pulse (blue) and the solution of Eq. 5.2 (black) under the assumption $d\delta = 0$ and $\chi = 0$ in dependence on the magnetic field $\mathcal{B}_\parallel$.*

5.7.2 Contribution of the Cotton-Mouton Effect

An interplay of Faraday and Cotton-Mouton effect can cause an alternating sense of rotation of the polarisation signal.

By incorporating the PIC-simulated perpendicular magnetic fields $\mathcal{B}_\perp$, the solution of Eq. 5.2 represents an interplay of the Faraday and the Cotton-Mouton effect. However, using the original values of the magnetic fields from the PIC-simulation, the alternating signal in the direction of propagation of the probe pulse still cannot be observed. Through an increase of the magnetic field strengths with maximum values of $\mathcal{B}_{\parallel,max} \approx 1.8 \times 10^4\,\mathrm{T}$ by a factor of 3 and $\mathcal{B}_{\perp,max} \approx 8.5 \times 10^4\,\mathrm{T}$ by a factor of 9, the solution of the coupled differential equations, which is shown in Fig. 5.10(b) delivers an alternating signal similar to those detected in the experiment and obtained by postprocessing the electric fields of the simulated probe pulse. Since the magnetic field of the laser pulse is almost one order of magnitude larger than the perpendicular magnetic field component generated by the plasma wave and the accelerated electrons, the phase shift δ, which leads to the alternation of the polarisation signal is caused by the magnetic field of the laser pulse. Fig. 5.11 compares the lineouts of the post processed signal (blue) and the signal obtained from the differential

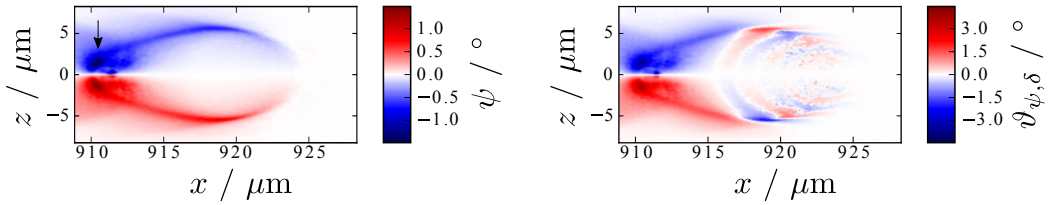

Figure 5.10 *(a) Angle of Faraday rotation ψ obtained by solving Eq. 5.2 under the assumption $d\delta = 0$ and $\chi = 0$. (b) Rotation of the polarisation ellipse $\vartheta_{\psi,\delta}$ calculated with multiples of the PIC-simulated magnetic fields ($3\mathcal{B}_{\parallel}$ and $9\mathcal{B}_{\perp}$).*

equations solved with the increased magnetic fields (green), which are in good agreement.

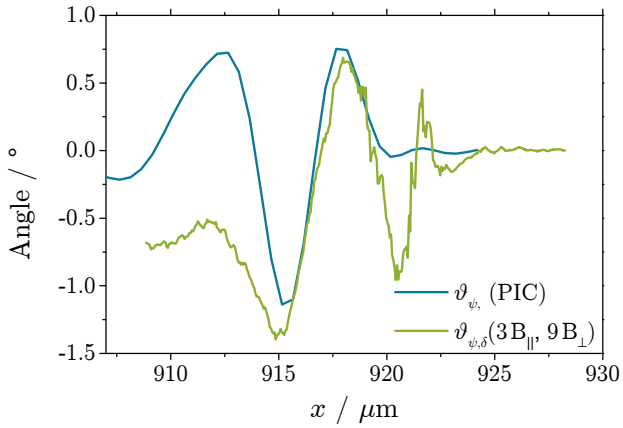

Figure 5.11 *Comparisson of the lineouts of signal 5 at the position $z = 4.67\,\mu m$ obtained from postprocessing the PIC-simulated electric field of the probe pulse (blue) and the solution of Eq. 5.2 (green) calculated with multiples of the PIC-simulated magnetic fields ($3\mathcal{B}_{\parallel}$ and $9\mathcal{B}_{\perp}$).*

As already observed above in the discussion of the pure Faraday effect, the amplitudes of the signal obtained from Eq. 5.2 underestimates the contribution of the magnetic fields. This might be caused by the simplifications made for the calculation, i.e., the use of quasi-static field distributions and the negligence of the duration of the probe pulse. Furthermore, the coupled differential equations do not account for propagation effects such as scattering and refraction of probe light in the plasma. An alternative reason might be the negligence of relativistic effects, more precisely the influence of the Lorentz transformation, which is currently investigated by M. B. Schwab [115]. The Lorentz transformation of the magnetic field strengths to the inertial system of the probe pulse causes an increase and a decrease of the magnetic fields at different positions and could possibly explain the difference between the results obtained through the postprocessing procedure and solving the coupled differential equations.

5.7.3 Laser Pulse Evolution in Simulation and Experiment

The evolution of laser pulse and plasma wave can be observed through the evolution of the polarisation signal. For the first time, the laser pulse intensity could be correlated to signatures of the oscillating magnetic field of the laser pulse.

Figs. 5.12(a) and 5.12(b) show polarisation signals at an early ($v_{g,L}t \approx 340\,\mu m$, sig-

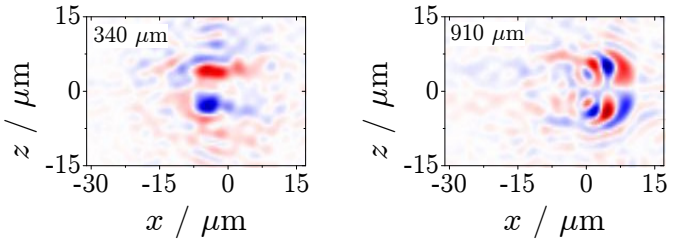

(a) (b)

Figure 5.12 *Polarisation signals obtained by postprocessing the PIC-simulated electric fields of the probe pulse. (a) Signal type 2. (b) Signal type 5.*

nal type 2) and a late ($v_{g,L}t \approx 910\,\mu$m, signal type 5) time during the interaction in the PIC-simulation, which have been introduced in section 5.5 already. While signal type 2 (Fig. 5.12(a)) can be explained by the Faraday effect alone, the alternating sense of rotation of signal type 5 (Fig. 5.12(b)) is most likely caused by an interplay of the Faraday effect and the Cotton-Mouton effect. This can be supported by the maxima of the magnetic fields oriented perpendicular to the direction of propagation of the probe pulse present in the PIC simulation data at the time of generation of the two signals (cf. Table 5.2). At

	Signal type 2	Signal type 5
Simulation		
$v_{g,L}t$ / μm	340	910
$\mathcal{B}_\perp$ /T	5.4×10^4	8.5×10^4
$\langle\vec{S}\rangle$ / $10^{19}\,\mathrm{W/cm^2}$	3.4	9.2
$I(\mathcal{B}_\perp)$ / $10^{19}\,\mathrm{W/cm^2}$	3.5	8.7
Experiment		
$v_{g,L}t$ / μm	670	1880

Table 5.2 *Maxima of the magnetic field oriented perpendicular to the direction of propagation of the probe pulse and maximum laser intensity represented by $\frac{1}{2}|\vec{S}|$ and $I(\mathcal{B}_\perp)$ in the PIC-simulation at $v_{g,L}t \approx 340\,\mu m$ (signal type 2) and $v_{g,L}t \approx 910\,\mu m$ (signal type 5). The corresponding polarisation signal types were observed in the experiment for the first time at $v_{g,L}t \approx 670\,\mu m$ and $v_{g,L}t \approx 1880\,\mu m$.*

$v_{g,L}t \approx 910\,\mu$m, $\mathcal{B}_\perp$ is increased with respect to the fields present at $v_{g,L}t \approx 340\,\mu$m. Additionally, Table 5.2 shows the maximum of the main laser pulse's intensity calculated from the Pointing vector as $I = |\langle\vec{S}\rangle_T| \approx \frac{1}{2}|\vec{S}| = \frac{1}{2}c^2\epsilon_0|\vec{\mathcal{E}}_L \times \vec{\mathcal{B}}_L|$ and from the maximum of the oscillating laser field $|\vec{\mathcal{B}}_L| \approx \mathcal{B}_\perp$ as $I = \frac{1}{2}\epsilon_0 c\mathcal{E}_L^2 \approx 1/2\epsilon_0 c^3\mathcal{B}_\perp^2$. Since the intensities computed with the two methods are similar at the respective positions $v_{g,L}t \approx 340\,\mu$m (signal type 2) and $v_{g,L}t \approx 910\,\mu$m (signal type 5), the laser pulse intensity can be approximated with the laser pulse's magnetic field alone. Moreover, the relation of the main laser pulse's intensity and the laser pulse's magnetic field can be utilised to correlate a specific polarisation signal type and amplitude to a certain laser pulse intensity. More precisely, the increase of the

main laser pulse's intensity from $3.4 \times 10^{19}\,\mathrm{W/cm^2}$ to $8.7 \times 10^{19}\,\mathrm{W/cm^2}$ – i.e., an increase by a factor of ≈ 2.5 – is correlated to the evolution of the polarisation signal from signal type 2 to signal type 5. This allows to draw conclusions regarding the evolution of the main laser pulse's intensity in the experiment. While in the PIC-simulation, signal types 2 and 5 could be observed at $v_{g,L}t \approx 340\,\mu$m and $v_{g,L}t \approx 910\,\mu$m, respectively, in the experiment these signal types appeared for the first time at $v_{g,L}t \approx 670\,\mu$m and $v_{g,L}t \approx 1880\,\mu$m, respectively.

Since the evolution of the polarisation signal in simulation and experiment is similar, one can assume a comparable laser plasma interaction and thus, an increase of the laser pulse intensity in the experiment by a factor of ≈ 2.5 is likely while the exact intensities at the respective positions might differ from the values obtained in the simulation. For a future application of this method as an on-line diagnostic for the intensity of the laser pulse at a given position in the plasma, a possible correlation of the polarisation signal type to a threshold intensity will have to be investigated, e.g., with the help of PIC-simulations. Nevertheless, the results above support the assumption of laser pulse evolution to higher intensities for larger propagation distances $v_{g,L}t$ in the plasma, which helped to interprete the data presented in Chapter 4 but unfortunately, could not be confirmed by the deduction of the γ-factor at different positions in the plasma (cf. section 4.2.4.1). Hence, the observation of the evolution of the main laser pulse is of enormous importance for the analysis of experimentally obtained data. In the reported experiment, the evolution of the laser intensity inside the plasma could be investigated for the first time by means of signatures of the oscillating magnetic field of the laser pulse.

6. Conclusions and Outlook

For future applications of the accelerated electron pulses and their secondary radiation, the electron pulse parameters have to be controllable and stable from shot-to-shot. One approach towards controllability is controlled injection of electrons into the accelerating phase of the plasma wave at a defined position inside a plasma which allows to tune the electron energy gain of the injected electrons. In this thesis controlled injection at a steep density transition towards lower densities was investigated. Due to the sudden lengthening of the plasma wavelength in the lower electron density, the rear of the plasma wave, which is modified in the lower density after the density transition, is seemingly stopped and the electrons forming the first density peak of the plasma wave behind the laser pulse generated in the higher electron density oscillate into the accelerating phase of the modified plasma wave. The density transition is located between the locally increased density of a shockfront generated by a knife edge brought into a supersonic gas jet and the following undisturbed part of that gas jet. By varying the position of the knife edge, the position of the shockfront and thus, the electron density profile of the ionised gas jet is changed. Therefore, the properties of the shockfront were characterised in detail in dependence on the position of the knife edge. Injection at the density transition could be observed through the detection of wavebreaking radiation emitted at the transition position. Furthermore, a correlation between the electron energy gain and the position of the transition was found. The maximum achievable electron energy gain is most likely not limited by dephasing or depletion but by an interplay of laser pulse evolution to higher intensities and the remaining acceleration length suggesting that despite the controllability of the position of injection, the acceleration process is still subject to the nonlinear interaction of laser pulse and plasma wave. Nevertheless, the constant γ-factor deduced for different positions of the shockfront does not indicate laser pulse evolution. These contradictory results could for example be caused by the statistical nature of the analysis of the data for the determination of γ. To shed some light on that, a technique to observe the evolution of the laser pulse is required and will be discussed below. While so far, the energy spread of the accelerated electrons was attributed solely to the width of the density transition, the results of the reported experiments suggest that the density ratio of the transition might play a role as well. Since the time during which the rear of the plasma wave is seemingly stopped is determined by the change of plasma wavelength, the time of injection might be increased by increasing the density ratio. Additionally, the period of injection might be increased through the deformation of the plasma wave at a tilted front, which might affect the behaviour of the

plasma wave's electron density distributions at distances behind the shockfront longer than the width of the front w_{SF}. Energy dependent pointing variations of the electron beam frequently observed in broadband electron energy distributions could be attributed to Betatron oscillations of the electron pulse in the transverse fields of the plasma wave. The results of three-dimensional PIC-simulations suggest that the oscillations are triggered by the tilt of the shockfront. The measurement and analysis of these transverse modulations provides information on the chirp and the longitudinal density distribution of the electron pulse inside the plasma wave, which is an important information for the application of the LWFA electrons e.g. for a free electron laser.

Optical observation of the evolution of the plasma wave and magnetic fields inextricably connected to laser wakefield acceleration might be the key to understanding the nonlinear processes in more detail and thus, to stabilise the accelerator output. While the plasma wave could be imaged with an ultra short probe pulse in combination with a high resolution imaging system, the optical observation of the magnetic fields additionally requires the investigation of the change of polarisation of the probe pulse acquired inside the region of interaction. This was realised in a setup designed to retrieve the angle of rotation of the plane of polarisation of the probe pulse by an angle ψ due to the magnetic fields of the plasma wave and the accelerated electrons oriented parallel to the direction of propagation of the probe pulse (Faraday effect). Therefore, the region of interaction was imaged onto two cameras equipped with a polarizer each. The polarisation signals observed early during the interaction are comparable to results discussed in previous publications and could be explained by the Faraday effect alone. Nevertheless, new types of polarisation signals with sub plasma wavelength features – more precisely, an alternating sense of rotation of the polarisation within one plasma wave period – were observed at later times during the interaction. Those signals could only be observed due to the ultra short probe pulse and its high resolution imaging system and are most likely generated in an interplay of the Faraday and the Cotton-Mouton effect where the latter occurs in magnetic fields perpendicular to the propagation direction of the probe pulse and generates a phase shift δ between the electric field components of the probe pulse. As a consequence, the angle retrieved from the experimental data is influenced by both, the rotation ψ and the phase shift δ and represents the angle of rotation $\vartheta_{\psi,\delta}$ of the polarisation ellipse. A similar evolution of the polarisation signal could be observed in three-dimensional PIC-simulations which also helped to trace back the generation of these sub plasma wavelength features to the front of the plasma wave where also the laser pulse is situated. In this configuration, the phase shift is most likely generated by the strong oscillating magnetic field of the laser pulse, which is almost one order of magnitude larger than the perpendicular field component of the plasma wave.

Therefore, high resolution polarimetry might be suitable for the on-line and in-situ observation of the evolution of the laser pulse, which – as discussed above – is important for the interpretation of experimental data. Methods to separate the contributions of laser pulse and plasma wave are suggested in the following sections.

Determination of the full state of polarisation and evolution of the laser pulse. Using 4 cameras equipped with polarisers set to polariser angles $\psi_p = 0°$, $\psi_p = 90°$, $\psi_p = 45°$ and $\psi_p = 135°$ with respect to full transmission of the initially linearly polarised probe pulse, the Stokes parameters S_0, S_1, S_2 and S_3 can be deduced. Table 6.1 shows different expressions for the Stokes parameters for a wave propagating in y-direction where $I_0 = S_0$ represents the full intensity of the probe light while I_p is the polarised fraction, i.e., in the case of fully polarised light $I_p = I_0$. The definition column shows how to calculate the Stokes parameters from the measured intensity profiles of the probe beam after the polarizers. Moreover, with the Stokes parameters in cartesian or spherical representation, the phase shift δ, the rotation of the polarisation ellipse $\vartheta_{\psi,\delta}$ and the ellipticity of the wave χ can be calculated. As discussed in chapter 5, the polarisation signal $\vartheta_{\psi,\delta}(x,z)$ evolves as a consequence of the evolution of laser pulse and plasma wave. The plain polarisation signal $\vartheta_{\psi,\delta}(x,z)$ generated at an early stage during the interaction, could be explained by the Faraday effect and thus, the rotation of the plane of polarisation through the magnetic fields parallel to the direction of propagation of the probe pulse – and therefore, by the plasma wave. In this case $\vartheta_{\psi,\delta}(x,z)$ is identical to the angle of Faraday rotation $\psi(x,z)$ and the phase shift $\delta(x,y) = 0$. In contrast, the alternating sense of rotation of $\vartheta_{\psi,\delta}(x,z)$ at a later time during the interaction could be correlated to the generation of a phase shift δ which can be attributed to an increase of the magnetic fields oriented perpendicular to the direction of propagation of the probe pulse. In three-dimensional PIC-simulations, a perpendicular magnetic field of $\mathcal{B}_{perp} \approx 5.4 \times 10^4$ T was present during the generation of the plain signal early during the interaction whereas at a later time during the interaction, an alternating sense of rotation was generated with a perpendicular field of $\mathcal{B}_{perp} \approx 8.5 \times 10^4$ T. Since the perpendicular magnetic fields are dominated by the strong magnetic field of the laser pulse, the evolution of the laser pulse can be indirectly observed by the deduction of δ. Moreover, the evolution of ψ, which is generated by the magnetic fields parallel to the direction of propagation of the probe pulse – and therefore, by the plasma wave – provides insight into the evolution of the plasma wave. The investigation of the nonlinear evolution of the laser pulse and plasma wave can help to find and understand the origin of instabilities, which lead to shot-to-shot fluctuations of the accelerator output. When the sources of the instabilities are determined, strategies to stabilise the interaction can be developed.

Evolution of the plasma wave. Although the angle of rotation given by the ratio of

	Definition	cartesian	spherical
S_0	$= I(\psi_p = 0°) + I(\psi_p = 90°)$	$= \langle \mathcal{E}_z^2 + \mathcal{E}_x^2 \rangle$	$= I_0$
S_1	$= I(\psi_p = 0°) - I(\psi_p = 90°)$	$= \langle \mathcal{E}_z^2 - \mathcal{E}_x^2 \rangle$	$= I_p \cos(2\vartheta_{\psi,\delta}) \cos(2\chi)$
S_2	$= I(\psi_p = 45°) - I(\psi_p = 135°)$	$= \langle \mathcal{E}_z \mathcal{E}_x \cos(\delta) \rangle$	$= I_p \sin(2\vartheta_{\psi,\delta}) \cos(2\chi)$
S_3	$= I_{RC} - I_{LC}$	$= \langle \mathcal{E}_z \mathcal{E}_x \sin(\delta) \rangle$	$= I_p \sin(2\chi)$

Table 6.1 *Stokes Parameters in different representations.*

the electric field components can be calculated by $\sin(2\chi) = \sin(2\psi)\sin(\delta)$ or $\tan(2\vartheta_{\psi,\delta}) = \tan(2\psi)\cos(\delta)$, this angle ψ is most likely not identical to the angle of pure Faraday rotation since a phase shift simultaneously acquired with the rotation of the plane of polarisation can reduce the final angle of rotation. Consider a rotation by the angle ψ and a subsequent phase shift by the angle δ which can be expressed as $\mathcal{E}_z \propto \sin(\Phi_x + \delta)\sin(\psi)$. A further rotation by ψ gives $\mathcal{E}_z \propto [\sin(\Phi_x + \delta) + \sin(\Phi_x)]\sin(\psi)$. Hence, the rotation is maximum if $\delta = 2n\pi$ with n being an integer while the rotation is zero if $\delta = (2n+1)\pi$. Nevertheless, the evolution of the plasma wave can be investigated, when the influence of the phase shift can be eliminated.

In contrast to the Cotton Mouton effect, the Faraday effect is sensitive to the sign of the magnetic field. Hence, the oscillating magnetic field of the laser pulse can generate a phase shift when the laser field is oriented perpendicular to the direction of propagation of the probe pulse while its influence on the rotation of the plane of polarisation in case of parallel orientation is averaged out. Since the perpendicular component of the plasma wave is significantly weaker than the magnetic field of the laser pulse, the influence of the Cotton-Mouton effect might be negligible if the magnetic field is oriented in the direction of propagation of the probe beam and the angle of rotation might solely represent the parallel magnetic fields of the plasma wave. Both, the evolution of the plasma wave and the laser pulse might be observed simultaneously by rotating the plane of polarisation of the main pulse to 45° and probing with two probe pulses both propagating transversely through the region of interaction but in different orientations with respect to the magnetic field of the main laser pulse.

In the future, secondary radiation generated during laser wakefield acceleration might be used for high resolution imaging, which is important for further research, e.g., in physics, chemistry or biology as well as for medical imaging. This thesis represents a step towards the application of LWFA since this requires stability and controlability of the accelerator output. Improved controllability could be demonstrated through controlled injection of electrons into the plasma waves. The remaining instabilities might be caused by nonlinear laser pulse evolution to higher intensities. Nevertheless, a method to observe this evolution was demonstrated above. Through the observation of laser pulse evolution, the exact

causes of the instabilities can be investigated in more detail, which can help to eliminate those instabilities and hence, generate electron pulses and secondary radiation with stable parameters.

Bibliography

[1] E. Rutherford: Phil. Mag. **6** (21), 1911

[2] A. R. Steere: *A TIMELINE OF MAJOR PARTICLE ACCELERATORS*, Master Thesis, Michigan State University 2005

[3] E. D. Bloom, D. H. Coward, H. DeStaebler, J. Drees, G. Miller, L. W. Mo, R. E. Taylor, M. Breidenbach, J. I. Friedman, G. C. Hartmann and H. W. Kendall: *High-Energy Inelastic $e-p$ Scattering at 6° and 10°*, Physical Review Letters **23** (16), S. 930–934, 1969, pRL
URL `http://link.aps.org/doi/10.1103/PhysRevLett.23.930`

[4] M. Breidenbach, J. I. Friedman, H. W. Kendall, E. D. Bloom, D. H. Coward, H. DeStaebler, J. Drees, L. W. Mo and R. E. Taylor: *Observed Behavior of Highly Inelastic Electron-Proton Scattering*, Physical Review Letters **23** (16), S. 935–939, 1969, pRL
URL `http://link.aps.org/doi/10.1103/PhysRevLett.23.935`

[5] *The Higgs boson, (2017 January 23).*
URL `https://home.cern/topics/higgs-boson`

[6] *Large Hadron Collider, (2017 January 23).*
URL `http://www.lhc-facts.ch/`

[7] *Chicago sees floods of LHC data and new results at ICHEP, (2017 January 23).*
URL `http://home.cern/about/updates/2016/08/chicago-sees-floods-lhc-data-and-new-results-ichep`

[8] T. Tajima and J. M. Dawson: *Laser Electron Accelerator*, Physical Review Letters **43** (4), S. 267–270, 1979, pRL
URL `http://link.aps.org/doi/10.1103/PhysRevLett.43.267`

[9] J. M. Dawson: *Nonlinear Electron Oscillations in a Cold Plasma*, Physical Review **113** (2), S. 383–387, 1959, pR
URL `http://link.aps.org/doi/10.1103/PhysRev.113.383`

[10] E. Esarey, C. B. Schroeder and W. P. Leemans: *Physics of laser-driven plasma-based electron accelerators*, Reviews of Modern Physics **81** (3), S. 1229–1285, 2009, rMP
URL `http://link.aps.org/doi/10.1103/RevModPhys.81.1229`

[11] P. Chen, J. M. Dawson, R. W. Huff and T. Katsouleas: *Acceleration of Electrons by the Interaction of a Bunched Electron Beam with a Plasma*, Physical Review Letters **54** (7), S. 693–696, 1985, pRL
URL https://link.aps.org/doi/10.1103/PhysRevLett.54.693

[12] J. B. Rosenzweig, D. B. Cline, B. Cole, H. Figueroa, W. Gai, R. Konecny, J. Norem, P. Schoessow and J. Simpson: *Experimental Observation of Plasma Wake-Field Acceleration*, Physical Review Letters **61** (1), S. 98–101, 1988, pRL
URL https://link.aps.org/doi/10.1103/PhysRevLett.61.98

[13] D. Strickland and G. Mourou: *Compression of amplified chirped optical pulses*, Optics Communications **56** (3), S. 219–221, 1985
URL http://www.sciencedirect.com/science/article/pii/0030401885901208

[14] A. Modena, Z. Najmudin, A. E. Dangor, C. E. Clayton, K. A. Marsh, C. Joshi, V. Malka, C. B. Darrow, C. Danson, D. Neely and F. N. Walsh: *Electron acceleration from the breaking of relativistic plasma waves*, Nature **377** (6550), S. 606–608, 1995, 10.1038/377606a0
URL http://dx.doi.org/10.1038/377606a0

[15] C. I. Moore, A. Ting, K. Krushelnick, E. Esarey, R. F. Hubbard, B. Hafizi, H. R. Burris, C. Manka and P. Sprangle: *Electron Trapping in Self-Modulated Laser Wakefields by Raman Backscatter*, Physical Review Letters **79** (20), S. 3909–3912, 1997, pRL
URL http://link.aps.org/doi/10.1103/PhysRevLett.79.3909

[16] A. Ting, C. I. Moore, K. Krushelnick, C. Manka, E. Esarey, P. Sprangle, R. Hubbard, H. R. Burris, R. Fischer and M. Baine: *Plasma wakefield generation and electron acceleration in a self-modulated laser wakefield accelerator experiment*, Physics of Plasmas **4** (5), S. 1889–1899, 1997
URL http://aip.scitation.org/doi/abs/10.1063/1.872332

[17] M. I. K. Santala, Z. Najmudin, E. L. Clark, M. Tatarakis, K. Krushelnick, A. E. Dangor, V. Malka, J. Faure, R. Allott and R. J. Clarke: *Observation of a Hot High-Current Electron Beam from a Self-Modulated Laser Wakefield Accelerator*, Physical Review Letters **86** (7), S. 1227–1230, 2001, pRL
URL http://link.aps.org/doi/10.1103/PhysRevLett.86.1227

[18] A. Pukhov and J. Meyer-ter Vehn: *Laser wake field acceleration: the highly non-linear broken-wave regime*, Applied Physics B **74** (4), S. 355–361
URL http://dx.doi.org/10.1007/s003400200795

[19] J. Faure, Y. Glinec, A. Pukhov, S. Kiselev, S. Gordienko, E. Lefebvre, J. P. Rousseau, F. Burgy and V. Malka: *A laser-plasma accelerator producing monoenergetic electron beams*, Nature **431** (7008), S. 541–544, 2004, 10.1038/nature02963
URL http://www.nature.com/nature/journal/v444/n7120/suppinfo/nature05393_S1.html

[20] C. G. R. Geddes, C. Toth, J. van Tilborg, E. Esarey, C. B. Schroeder, D. Bruhwiler, C. Nieter, J. Cary and W. P. Leemans: *High-quality electron beams from a laser wakefield accelerator using plasma-channel guiding*, Nature **431** (7008), S. 538–541, 2004, 10.1038/nature02900
URL http://dx.doi.org/10.1038/nature02900

[21] S. P. D. Mangles, C. D. Murphy, Z. Najmudin, A. G. R. Thomas, J. L. Collier, A. E. Dangor, E. J. Divall, P. S. Foster, J. G. Gallacher, C. J. Hooker, D. A. Jaroszynski, A. J. Langley, W. B. Mori, P. A. Norreys, F. S. Tsung, R. Viskup, B. R. Walton and K. Krushelnick: *Monoenergetic beams of relativistic electrons from intense laser-plasma interactions*, Nature **431** (7008), S. 535–538, 2004, 10.1038/nature02939
URL http://dx.doi.org/10.1038/nature02939

[22] W. P. Leemans, B. Nagler, A. J. Gonsalves, C. Toth, K. Nakamura, C. G. R. Geddes, E. Esarey, C. B. Schroeder and S. M. Hooker: *GeV electron beams from a centimetre-scale accelerator*, Nat Phys **2** (10), S. 696–699, 2006, 10.1038/nphys418
URL http://dx.doi.org/10.1038/nphys418

[23] X. Wang, R. Zgadzaj, N. Fazel, Z. Li, S. A. Yi, X. Zhang, W. Henderson, Y. Y. Chang, R. Korzekwa, H. E. Tsai, C. H. Pai, H. Quevedo, G. Dyer, E. Gaul, M. Martinez, A. C. Bernstein, T. Borger, M. Spinks, M. Donovan, V. Khudik, G. Shvets, T. Ditmire and M. C. Downer: *Quasi-monoenergetic laser-plasma acceleration of electrons to 2?GeV*, Nat Commun **4**, 2013
URL http://dx.doi.org/10.1038/ncomms2988

[24] W. P. Leemans, A. J. Gonsalves, H. S. Mao, K. Nakamura, C. Benedetti, C. B. Schroeder, C. Tóth, J. Daniels, D. E. Mittelberger, S. S. Bulanov, J. L. Vay, C. G. R. Geddes and E. Esarey: *Multi-GeV Electron Beams from Capillary-Discharge-Guided Subpetawatt Laser Pulses in the Self-Trapping Regime*, Physical Review Letters **113** (24), S. 245002, 2014, pRL
URL http://link.aps.org/doi/10.1103/PhysRevLett.113.245002

[25] S. Steinke, J. van Tilborg, C. Benedetti, C. G. R. Geddes, C. B. Schroeder, J. Daniels, K. K. Swanson, A. J. Gonsalves, K. Nakamura, N. H. Matlis, B. H. Shaw, E. Esarey

and W. P. Leemans: *Multistage coupling of independent laser-plasma accelerators*, Nature **530** (7589), S. 190–193, 2016
URL http://dx.doi.org/10.1038/nature16525

[26] H. P. Schlenvoigt, K. Haupt, A. Debus, F. Budde, O. Jackel, S. Pfotenhauer, H. Schwoerer, E. Rohwer, J. G. Gallacher, E. Brunetti, R. P. Shanks, S. M. Wiggins and D. A. Jaroszynski: *A compact synchrotron radiation source driven by a laser-plasma wakefield accelerator*, Nat Phys **4** (2), S. 130–133, 2008, 10.1038/nphys811
URL http://dx.doi.org/10.1038/nphys811

[27] M. Fuchs, R. Weingartner, A. Popp, Z. Major, S. Becker, J. Osterhoff, I. Cortrie, B. Zeitler, R. Horlein, G. D. Tsakiris, U. Schramm, T. P. Rowlands-Rees, S. M. Hooker, D. Habs, F. Krausz, S. Karsch and F. Gruner: *Laser-driven soft-X-ray undulator source*, Nat Phys **5** (11), S. 826–829, 2009, 10.1038/nphys1404
URL http://dx.doi.org/10.1038/nphys1404

[28] W. P. Leemans, C. G. R. Geddes, J. Faure, C. Tóth, J. van Tilborg, C. B. Schroeder, E. Esarey, G. Fubiani, D. Auerbach, B. Marcelis, M. A. Carnahan, R. A. Kaindl, J. Byrd and M. C. Martin: *Observation of Terahertz Emission from a Laser-Plasma Accelerated Electron Bunch Crossing a Plasma-Vacuum Boundary*, Physical Review Letters **91** (7), S. 074802, 2003, pRL
URL http://link.aps.org/doi/10.1103/PhysRevLett.91.074802

[29] A. Buck, M. Nicolai, K. Schmid, C. M. S. Sears, A. Savert, J. M. Mikhailova, F. Krausz, M. C. Kaluza and L. Veisz: *Real-time observation of laser-driven electron acceleration*, Nat Phys **7** (7), S. 543–548, 2011, 10.1038/nphys1942
URL http://dx.doi.org/10.1038/nphys1942

[30] O. Lundh, C. Rechatin, J. Lim, V. Malka and J. Faure: *Experimental Measurements of Electron-Bunch Trains in a Laser-Plasma Accelerator*, Physical Review Letters **110** (6), S. 065005, 2013, pRL
URL http://link.aps.org/doi/10.1103/PhysRevLett.110.065005

[31] S. Kneip, C. McGuffey, F. Dollar, M. S. Bloom, V. Chvykov, G. Kalintchenko, K. Krushelnick, A. Maksimchuk, S. P. D. Mangles, T. Matsuoka, Z. Najmudin, C. A. J. Palmer, J. Schreiber, W. Schumaker, A. G. R. Thomas and V. Yanovsky: *X-ray phase contrast imaging of biological specimens with femtosecond pulses of betatron radiation from a compact laser plasma wakefield accelerator*, Applied Physics Letters **99** (9), S. 093701, 2011
URL https://aip.scitation.org/doi/abs/10.1063/1.3627216

[32] J. Wenz, S. Schleede, K. Khrennikov, M. Bech, P. Thibault, M. Heigoldt, F. Pfeiffer and S. Karsch: *Quantitative X-ray phase-contrast microtomography from a compact laser-driven betatron source*, Nature Communications **6**, S. 7568, 2015
URL http://dx.doi.org/10.1038/ncomms8568

[33] M. Chen, Z.-M. Sheng, Y.-Y. Ma and J. Zhang: *Electron injection and trapping in a laser wakefield by field ionization to high-charge states of gases*, Journal of Applied Physics **99** (5), S. 056109, 2006
URL http://scitation.aip.org/content/aip/journal/jap/99/5/10.1063/1.2179194

[34] M. Z. Mo, A. Ali, S. Fourmaux, P. Lassonde, J. C. Kieffer and R. Fedosejevs: *Quasimonoenergetic electron beams from laser wakefield acceleration in pure nitrogen*, Applied Physics Letters **100** (7), S. 074101, 2012
URL http://scitation.aip.org/content/aip/journal/apl/100/7/10.1063/1.3685464

[35] A. Pak, K. A. Marsh, S. F. Martins, W. Lu, W. B. Mori and C. Joshi: *Injection and Trapping of Tunnel-Ionized Electrons into Laser-Produced Wakes*, Physical Review Letters **104** (2), S. 025003, 2010, pRL
URL http://link.aps.org/doi/10.1103/PhysRevLett.104.025003

[36] C. E. Clayton, J. E. Ralph, F. Albert, R. A. Fonseca, S. H. Glenzer, C. Joshi, W. Lu, K. A. Marsh, S. F. Martins, W. B. Mori, A. Pak, F. S. Tsung, B. B. Pollock, J. S. Ross, L. O. Silva and D. H. Froula: *Self-Guided Laser Wakefield Acceleration beyond 1 GeV Using Ionization-Induced Injection*, Physical Review Letters **105** (10), S. 105003, 2010, pRL
URL http://link.aps.org/doi/10.1103/PhysRevLett.105.105003

[37] C. McGuffey, A. G. R. Thomas, W. Schumaker, T. Matsuoka, V. Chvykov, F. J. Dollar, G. Kalintchenko, V. Yanovsky, A. Maksimchuk, K. Krushelnick, V. Y. Bychenkov, I. V. Glazyrin and A. V. Karpeev: *Ionization Induced Trapping in a Laser Wakefield Accelerator*, Physical Review Letters **104** (2), S. 025004, 2010, pRL
URL http://link.aps.org/doi/10.1103/PhysRevLett.104.025004

[38] D. Umstadter, J. K. Kim and E. Dodd: *Laser Injection of Ultrashort Electron Pulses into Wakefield Plasma Waves*, Physical Review Letters **76** (12), S. 2073–2076, 1996, pRL
URL http://link.aps.org/doi/10.1103/PhysRevLett.76.2073

[39] E. Esarey, R. F. Hubbard, W. P. Leemans, A. Ting and P. Sprangle: *Electron Injection into Plasma Wakefields by Colliding Laser Pulses*, Physical Review Letters **79** (14), S. 2682–2685, 1997, pRL
URL http://link.aps.org/doi/10.1103/PhysRevLett.79.2682

[40] J. Faure, C. Rechatin, A. Norlin, A. Lifschitz, Y. Glinec and V. Malka: *Controlled injection and acceleration of electrons in plasma wakefields by colliding laser pulses*, Nature **444** (7120), S. 737–739, 2006, 10.1038/nature05393
URL http://dx.doi.org/10.1038/nature05393

[41] C. G. R. Geddes, K. Nakamura, G. R. Plateau, C. Toth, E. Cormier-Michel, E. Esarey, C. B. Schroeder, J. R. Cary and W. P. Leemans: *Plasma-Density-Gradient Injection of Low Absolute-Momentum-Spread Electron Bunches*, Physical Review Letters **100** (21), S. 215004, 2008, pRL
URL http://link.aps.org/doi/10.1103/PhysRevLett.100.215004

[42] A. J. Gonsalves, K. Nakamura, C. Lin, D. Panasenko, S. Shiraishi, T. Sokollik, C. Benedetti, C. B. Schroeder, C. G. R. Geddes, J. van Tilborg, J. Osterhoff, E. Esarey, C. Toth and W. P. Leemans: *Tunable laser plasma accelerator based on longitudinal density tailoring*, Nat Phys **7** (11), S. 862–866, 2011, 10.1038/nphys2071
URL http://dx.doi.org/10.1038/nphys2071

[43] M. Hansson, B. Aurand, X. Davoine, H. Ekerfelt, K. Svensson, A. Persson, C. G. Wahlström and O. Lundh: *Down-ramp injection and independently controlled acceleration of electrons in a tailored laser wakefield accelerator*, Physical Review Special Topics - Accelerators and Beams **18** (7), S. 071303, 2015, pRSTAB
URL http://link.aps.org/doi/10.1103/PhysRevSTAB.18.071303

[44] H. Suk, N. Barov, J. B. Rosenzweig and E. Esarey: *Plasma Electron Trapping and Acceleration in a Plasma Wake Field Using a Density Transition*, Physical Review Letters **86** (6), S. 1011–1014, 2001, pRL
URL http://link.aps.org/doi/10.1103/PhysRevLett.86.1011

[45] P. Tomassini, M. Galimberti, A. Giulietti, D. Giulietti, L. A. Gizzi, L. Labate and F. Pegoraro: *Production of high-quality electron beams in numerical experiments of laser wakefield acceleration with longitudinal wave breaking*, Physical Review Special Topics - Accelerators and Beams **6** (12), S. 121301, 2003, pRSTAB
URL http://link.aps.org/doi/10.1103/PhysRevSTAB.6.121301

[46] H. Suk, H. J. Lee and I. S. Ko: *Generation of high-energy electrons by a femtosecond terawatt laser propagating through a sharp downward density transition*, Journal of the Optical Society of America B **21** (7), S. 1391–1396, 2004
URL http://josab.osa.org/abstract.cfm?URI=josab-21-7-1391

[47] K. Schmid, A. Buck, C. M. S. Sears, J. M. Mikhailova, R. Tautz, D. Herrmann, M. Geissler, F. Krausz and L. Veisz: *Density-transition based electron injector for laser driven wakefield accelerators*, Physical Review Special Topics - Accelerators and Beams **13** (9), S. 091301, 2010, pRSTAB
URL http://link.aps.org/doi/10.1103/PhysRevSTAB.13.091301

[48] A. Buck, J. Wenz, J. Xu, K. Khrennikov, K. Schmid, M. Heigoldt, J. M. Mikhailova, M. Geissler, B. Shen, F. Krausz, S. Karsch and L. Veisz: *Shock-Front Injector for High-Quality Laser-Plasma Acceleration*, Physical Review Letters **110** (18), S. 185006, 2013, pRL
URL http://link.aps.org/doi/10.1103/PhysRevLett.110.185006

[49] M. Burza, A. Gonoskov, K. Svensson, F. Wojda, A. Persson, M. Hansson, G. Genoud, M. Marklund, C. G. Wahlström and O. Lundh: *Laser wakefield acceleration using wire produced double density ramps*, Physical Review Special Topics - Accelerators and Beams **16** (1), S. 011301, 2013, pRSTAB
URL http://link.aps.org/doi/10.1103/PhysRevSTAB.16.011301

[50] N. H. Matlis, S. Reed, S. S. Bulanov, V. Chvykov, G. Kalintchenko, T. Matsuoka, P. Rousseau, V. Yanovsky, A. Maksimchuk, S. Kalmykov, G. Shvets and M. C. Downer: *Snapshots of laser wakefields*, Nat Phys **2** (11), S. 749–753, 2006, 10.1038/nphys442
URL http://dx.doi.org/10.1038/nphys442

[51] M. B. Schwab, A. Sävert, O. Jäckel, J. Polz, M. Schnell, T. Rinck, L. Veisz, M. Möller, P. Hansinger, G. G. Paulus and M. C. Kaluza: *Few-cycle optical probe-pulse for investigation of relativistic laser-plasma interactions*, Applied Physics Letters **103** (19), S. 191118, 2013
URL http://scitation.aip.org/content/aip/journal/apl/103/19/10.1063/1.4829489

[52] A. Sävert, S. P. D. Mangles, M. Schnell, E. Siminos, J. M. Cole, M. Leier, M. Reuter, M. B. Schwab, M. Möller, K. Poder, O. Jäckel, G. G. Paulus, C. Spielmann, S. Skupin, Z. Najmudin and M. C. Kaluza: *Direct Observation of the Injection Dynamics of a*

Laser Wakefield Accelerator Using Few-Femtosecond Shadowgraphy, Physical Review Letters **115** (5), S. 055002, 2015, pRL
URL http://link.aps.org/doi/10.1103/PhysRevLett.115.055002

[53] J. R. Marquès, J. P. Geindre, F. Amiranoff, P. Audebert, J. C. Gauthier, A. Antonetti and G. Grillon: *Temporal and Spatial Measurements of the Electron Density Perturbation Produced in the Wake of an Ultrashort Laser Pulse*, Physical Review Letters **76** (19), S. 3566–3569, 1996, pRL
URL http://link.aps.org/doi/10.1103/PhysRevLett.76.3566

[54] C. W. Siders, S. P. Le Blanc, D. Fisher, T. Tajima, M. C. Downer, A. Babine, A. Stepanov and A. Sergeev: *Laser Wakefield Excitation and Measurement by Femtosecond Longitudinal Interferometry*, Physical Review Letters **76** (19), S. 3570–3573, 1996, pRL
URL http://link.aps.org/doi/10.1103/PhysRevLett.76.3570

[55] Z. Li, H.-E. Tsai, X. Zhang, C.-H. Pai, Y.-Y. Chang, R. Zgadzaj, X. Wang, V. Khudik, G. Shvets and M. C. Downer: *Single-Shot Visualization of Evolving Laser Wakefields Using an All-Optical Streak Camera*, Physical Review Letters **113** (8), S. 085001, 2014, pRL
URL https://link.aps.org/doi/10.1103/PhysRevLett.113.085001

[56] M. C. Kaluza, H. P. Schlenvoigt, S. P. D. Mangles, A. G. R. Thomas, A. E. Dangor, H. Schwoerer, W. B. Mori, Z. Najmudin and K. M. Krushelnick: *Measurement of Magnetic-Field Structures in a Laser-Wakefield Accelerator*, Physical Review Letters **105** (11), S. 115002, 2010, pRL
URL http://link.aps.org/doi/10.1103/PhysRevLett.105.115002

[57] B. Walton, A. E. Dangor, S. P. D. Mangles, Z. Najmudin, K. Krushelnick, A. G. R. Thomas, S. Fritzler and V. Malka: *Measurements of magnetic field generation at ionization fronts from laser wakefield acceleration experiments*, New Journal of Physics **15** (2), S. 025034, 2013
URL http://stacks.iop.org/1367-2630/15/i=2/a=025034

[58] A. Flacco, J. Vieira, A. Lifschitz, F. Sylla, S. Kahaly, M. Veltcheva, L. O. Silva and V. Malka: *Persistence of magnetic field driven by relativistic electrons in a plasma*, Nat Phys **11** (5), S. 409–413, 2015
URL http://dx.doi.org/10.1038/nphys3303

[59] J. D. Jackson: *Classical Electrodynamics*, John Wiley and Sons 1962

[60] E. Hecht: *Optik*, Oldenbourg **3. Auflage**

[61] A. E. Siegman: *Lasers*, University Science Books **First Edition**, 1986

[62] B. E. A. Saleh and M. C. Teich: *Fundamentals of Photonics*, John Wiley and Sons **First Edition**, 1991

[63] V. Yanovsky, V. Chvykov, G. Kalinchenko, P. Rousseau, T. Planchon, T. Matsuoka, A. Maksimchuk, J. Nees, G. Cheriaux, G. Mourou and K. Krushelnick: *Ultra-high intensity- 300-TW laser at 0.1 Hz repetition rate*, Optics Express **16** (3), S. 2109–2114, 2008
URL `http://www.opticsexpress.org/abstract.cfm?URI=oe-16-3-2109`

[64] P. Mulser and D. Bauer: *High Power Laser Matter Interaction*, Springer 2010

[65] F. F. Chen: *Introduction to PLasma Physics and Controlled Fusion*, Plenum Press New York and London **Second Edition**

[66] J. A. Bittencourt: *Fundamentals of Plasma Physics*, Springer 2004

[67] P. Gibbon: *Short pulse laser interactions with matter*, Imperial College Press 2005

[68] A. K. and, Y. Ralchenko, J. R. Team and N. ASD:
URL `http://physics.nist.gov/asd`

[69] W. B. Mori: *The physics of the nonlinear optics of plasmas at relativistic intensities for short-pulse lasers*, Quantum Electronics, IEEE Journal of **33** (11), S. 1942–1953, 1997

[70] G.-Z. Sun, E. Ott, Y. C. Lee and P. Guzdar: *Self-focusing of short intense pulses in plasmas*, Physics of Fluids **30** (2), S. 526–532, 1987
URL `http://scitation.aip.org/content/aip/journal/pof1/30/2/10.1063/1.866349`

[71] P. Sprangle, E. Esarey, A. Ting and G. Joyce: *Laser wakefield acceleration and relativistic optical guiding*, Applied Physics Letters **53** (22), S. 2146–2148, 1988
URL `http://scitation.aip.org/content/aip/journal/apl/53/22/10.1063/1.100300`

[72] G. A. Mourou, T. Tajima and S. V. Bulanov: *Optics in the relativistic regime*, Reviews of Modern Physics **78** (2), S. 309–371, 2006, rMP
URL `http://link.aps.org/doi/10.1103/RevModPhys.78.309`

[73] B. Hafizi, A. Ting, P. Sprangle and R. F. Hubbard: *Relativistic focusing and ponderomotive channeling of intense laser beams*, Physical Review E **62** (3), S. 4120–4125, 2000, pRE
URL http://link.aps.org/doi/10.1103/PhysRevE.62.4120

[74] S. Mangles: *An Overview of Recent Progress in LaserWakefield Acceleration Experiments*, 2016 **1**, 2016
URL https://e-publishing.cern.ch/index.php/CYR/article/view/224

[75] W. Lu, M. Tzoufras, C. Joshi, F. S. Tsung, W. B. Mori, J. Vieira, R. A. Fonseca and L. O. Silva: *Generating multi-GeV electron bunches using single stage laser wakefield acceleration in a 3D nonlinear regime*, Physical Review Special Topics - Accelerators and Beams **10** (6), S. 061301, 2007, pRSTAB
URL http://link.aps.org/doi/10.1103/PhysRevSTAB.10.061301

[76] S. Gordienko and A. Pukhov: *Scalings for ultrarelativistic laser plasmas and quasimonoenergetic electrons*, Physics of Plasmas **12** (4), S. 043109, 2005
URL http://scitation.aip.org/content/aip/journal/pop/12/4/10.1063/1.1884126

[77] V. I. Berezhiani and I. G. Murusidze: *Interaction of highly relativistic short laser pulses with plasmas and nonlinear wake-field generation*, Physica Scripta **45** (2), S. 87, 1992
URL http://stacks.iop.org/1402-4896/45/i=2/a=007

[78] S. V. Bulanov, V. I. Kirsanov and A. S. Sakharov: *Excitation of ultrarelativistic plasma waves by pulse of electromagnetic radiation*, JETP Lett **50**, S. 710, 1989
URL http://jetpletters.ac.ru/ps/1127/article_17078.pdf

[79] A. I. Akhiezer and R. V. Polovin: *Theory of Wave Motion of an Electron Plasma*, Sov. Phys. JETP **3** (5), 1956
URL http://www.jetp.ac.ru/cgi-bin/dn/e_003_05_0696.pdf

[80] S. V. Bulanov, F. Pegoraro, A. M. Pukhov and A. S. Sakharov: *Transverse-Wake Wave Breaking*, Physical Review Letters **78** (22), S. 4205–4208, 1997, pRL
URL http://jetpletters.ac.ru/ps/1127/article_17078.pdf

[81] T. Esirkepov, S. V. Bulanov, M. Yamagiwa and T. Tajima: *Electron, Positron, and Photon Wakefield Acceleration: Trapping, Wake Overtaking, and Ponderomotive Acceleration*, Physical Review Letters **96** (1), S. 014803, 2006, pRL
URL https://link.aps.org/doi/10.1103/PhysRevLett.96.014803

[82] E. Esarey, B. A. Shadwick, C. B. Schroeder and W. P. Leemans: *Nonlinear Pump Depletion and Electron Dephasing in Laser Wakefield Accelerators*, AIP Conference Proceedings **737** (1), S. 578–584, 2004
URL http://scitation.aip.org/content/aip/proceeding/aipcp/10.1063/1.1842594

[83] B. A. Shadwick, C. B. Schroeder and E. Esarey: *Nonlinear laser energy depletion in laser-plasma acceleratorsa)*, Physics of Plasmas **16** (5), S. 056704, 2009
URL http://scitation.aip.org/content/aip/journal/pop/16/5/10.1063/1.3124185

[84] C. M. Wang and J. P. Goedbloed: *Magnetically tapered plasma channels for laser wakefield accelerators*, Journal of Physics D: Applied Physics **41** (8), S. 085203, 2008
URL http://stacks.iop.org/0022-3727/41/i=8/a=085203

[85] T. Katsouleas: *Physical mechanisms in the plasma wake-field accelerator*, Physical Review A **33** (3), S. 2056–2064, 1986, pRA
URL http://link.aps.org/doi/10.1103/PhysRevA.33.2056

[86] P. Sprangle, B. Hafizi, J. R. Peñano, R. F. Hubbard, A. Ting, C. I. Moore, D. F. Gordon, A. Zigler, D. Kaganovich and T. M. Antonsen: *Wakefield generation and GeV acceleration in tapered plasma channels*, Physical Review E **63** (5), S. 056405, 2001, pRE
URL http://link.aps.org/doi/10.1103/PhysRevE.63.056405

[87] D. J. Spence, A. Butler and S. M. Hooker: *First demonstration of guiding of high-intensity laser pulses in a hydrogen-filled capillary discharge waveguide*, Journal of Physics B: Atomic, Molecular and Optical Physics **34** (21), S. 4103, 2001
URL http://stacks.iop.org/0953-4075/34/i=21/a=303

[88] A. Pukhov and S. Gordienko: *Bubble regime of wake field acceleration: similarity theory and optimal scalings*, Philosophical Transactions of the Royal Society of London A: Mathematical, Physical and Engineering Sciences **364** (1840), S. 623–633, 2006
URL http://rsta.royalsocietypublishing.org/roypta/364/1840/623.full.pdf

[89] J. Krall, A. Ting, E. Esarey and P. Sprangle: *Self-modulated-laser wakefield acceleration*, in: *Particle Accelerator Conference, 1993., Proceedings of the 1993*, S. 2629–2631 vol.4

[90] B. Hidding, T. Königstein, J. Osterholz, S. Karsch, O. Willi and G. Pretzler: *Monoenergetic Energy Doubling in a Hybrid Laser-Plasma Wakefield Accelerator*, Physical Review Letters **104** (19), S. 195002, 2010, pRL
URL http://link.aps.org/doi/10.1103/PhysRevLett.104.195002

[91] M. Schnell, A. Sävert, I. Uschmann, M. Reuter, M. Nicolai, T. Kämpfer, B. Landgraf, O. Jäckel, O. Jansen, A. Pukhov, M. C. Kaluza and C. Spielmann: *Optical control of hard X-ray polarization by electron injection in a laser wakefield accelerator*, Nature Communications **4**, S. 2421, 2013
URL http://dx.doi.org/10.1038/ncomms3421

[92] S. Kuschel, D. Hollatz, T. Heinemann, O. Karger, M. B. Schwab, D. Ullmann, A. Knetsch, A. Seidel, C. Rödel, M. Yeung, M. Leier, A. Blinne, H. Ding, T. Kurz, D. J. Corvan, A. Sävert, S. Karsch, M. C. Kaluza, B. Hidding and M. Zepf: *Demonstration of passive plasma lensing of a laser wakefield accelerated electron bunch*, Physical Review Accelerators and Beams **19** (7), S. 071301, 2016, pRAB
URL http://link.aps.org/doi/10.1103/PhysRevAccelBeams.19.071301

[93] A. Buck: *Advanced characterization and control of laser wakefield acceleration*, Dissertation, LMU München 2011

[94] A. G. R. Thomas, S. P. D. Mangles, Z. Najmudin, M. C. Kaluza, C. D. Murphy and K. Krushelnick: *Measurements of Wave-Breaking Radiation from a Laser-Wakefield Accelerator*, Physical Review Letters **98** (5), S. 054802, 2007, pRL
URL http://link.aps.org/doi/10.1103/PhysRevLett.98.054802

[95] K. Guenther and J.-E. Contributors: *Approximate method to extract the pure Faraday and Cotton–Mouton effects from polarimetry measurements in a tokamak*, Plasma Physics and Controlled Fusion **46** (9), S. 1423, 2004
URL http://stacks.iop.org/0741-3335/46/i=9/a=006

[96] T. D. Arber, K. Bennett, C. S. Brady, A. Lawrence-Douglas, M. G. Ramsay, N. J. Sircombe, P. Gillies, R. G. Evans, H. Schmitz, A. R. Bell and C. P. Ridgers: *Contemporary particle-in-cell approach to laser-plasma modelling*, Plasma Physics and Controlled Fusion **57** (11), S. 113001, 2015
URL http://stacks.iop.org/0741-3335/57/i=11/a=113001

[97] S. Semushin and V. Malka: *High density gas jet nozzle design for laser target production*, Review of Scientific Instruments **72** (7), S. 2961–2965, 2001

URL http://scitation.aip.org/content/aip/journal/rsi/72/7/10.1063/1.1380393

[98] B. Landgraf: *Charakterisierung von Überschalldüsen zur Elektronenbeschleunigung*, Diploma Thesis, FSU Jena 2010

[99] D. Haenel: *Molekulare Gasdynamik*, Springer-Verlag, Berlin, 1 Aufl., 2004

[100] H. M. Mott-Smith: *The Solution of the Boltzmann Equation for a Shock Wave*, 1951, pR
URL http://link.aps.org/doi/10.1103/PhysRev.82.885

[101] A. Buck, K. Zeil, A. Popp, K. Schmid, A. Jochmann, S. D. Kraft, B. Hidding, T. Kudyakov, C. M. S. Sears, L. Veisz, S. Karsch, J. Pawelke, R. Sauerbrey, T. Cowan, F. Krausz and U. Schramm: *Absolute charge calibration of scintillating screens for relativistic electron detection*, Review of Scientific Instruments **81** (3), S. 033301, 2010
URL http://aip.scitation.org/doi/abs/10.1063/1.3310275

[102] D. Adolph, M. Möller, J. Bierbach, M. Schwab, A. Sävert, M. Yeung, A. M. Sayler, M. Zepf, M. C. Kaluza and G. G. Paulus: *Real-time, single-shot, carrier-envelope-phase measurement of a multi-terawatt laser*, Applied Physics Letters **110** (8), S. 081105, 2017
URL http://aip.scitation.org/doi/abs/10.1063/1.4976695

[103] *Edmund Optics GmbH*
URL http://www.edmundoptics.de/microscopy/infinity-corrected-objectives/mitutoyo-infinity-corrected-long-working-distance-objectives/46144

[104] C. E. Shannon: *Communication In The Presence Of Noise*, Proceedings of the IEEE **86** (2), S. 447–457, 1998

[105] E. Siminos, S. Skupin, A. Sävert, J. M. Cole, S. P. D. Mangles and M. C. Kaluza: *Modeling ultrafast shadowgraphy in laser-plasma interaction experiments*, Plasma Physics and Controlled Fusion **58** (6), S. 065004, 2016
URL http://stacks.iop.org/0741-3335/58/i=6/a=065004

[106] A. Sävert: *Few-cycle microscopy of a laser wakefield accelerator*, Dissertation, FSU, Jena 2016

[107] P. Tomassini, A. Giulietti, L. A. Gizzi, M. Galimberti, D. Giulietti, M. Borghesi and O. Willi: *Analyzing laser plasma interferograms with a continuous wavelet transform*

ridgeextraction technique: the method, Applied Optics **40** (35), S. 6561–6568, 2001
URL http://ao.osa.org/abstract.cfm?URI=ao-40-35-6561

[108] B. Walton: *Optical diagnostics of laser plasma particle acceleration experiments*, Dissertation, Imperial College London 2004

[109] K. Schmid: *Supersonic Micro-Jets And Their Application to Few-Cycle Laser-Driven Electron Acceleration*, Dissertation, LMU München 2009

[110] T. Matsuoka, C. McGuffey, P. G. Cummings, Y. Horovitz, F. Dollar, V. Chvykov, G. Kalintchenko, P. Rousseau, V. Yanovsky, S. S. Bulanov, A. G. R. Thomas, A. Maksimchuk and K. Krushelnick: *Stimulated Raman Side Scattering in Laser Wakefield Acceleration*, Physical Review Letters **105** (3), S. 034801, 2010, pRL
URL http://link.aps.org/doi/10.1103/PhysRevLett.105.034801

[111] S. Chou, J. Xu, K. Khrennikov, D. E. Cardenas, J. Wenz, M. Heigoldt, L. Hofmann, L. Veisz and S. Karsch: *Collective Deceleration of Laser-Driven Electron Bunches*, Physical Review Letters **117** (14), S. 144801, 2016, pRL
URL http://link.aps.org/doi/10.1103/PhysRevLett.117.144801

[112] C. Rechatin, X. Davoine, A. Lifschitz, A. B. Ismail, J. Lim, E. Lefebvre, J. Faure and V. Malka: *Observation of Beam Loading in a Laser-Plasma Accelerator*, Physical Review Letters **103** (19), S. 194804, 2009, pRL
URL https://link.aps.org/doi/10.1103/PhysRevLett.103.194804

[113] Y. Glinec, J. Faure, A. Lifschitz, J. M. Vieira, R. A. Fonseca, L. O. Silva and V. Malka: *Direct observation of betatron oscillations in a laser-plasma electron accelerator*, EPL (Europhysics Letters) **81** (6), S. 64001, 2008
URL http://stacks.iop.org/0295-5075/81/i=6/a=64001

[114] T. Matsuoka, C. McGuffey, P. G. Cummings, S. S. Bulanov, V. Chvykov, F. Dollar, Y. Horovitz, G. Kalintchenko, K. Krushelnick, P. Rousseau, A. G. R. Thomas, V. Yanovsky and A. Maksimchuk: *On electron betatron motion and electron injection in laser wakefield accelerators*, Plasma Physics and Controlled Fusion **56** (8), S. 084009, 2014
URL http://stacks.iop.org/0741-3335/56/i=8/a=084009

[115] M. B. Schwab: *private communication*, 2018

[116] F. Ronneberger: *private communication* 2017

[117] *Mazzler, (2018 May 15)*
URL http://www.fastlite.com/en/ar824673-823529-Mazzler.html?Cookie=set

[118] S. Kuschel, , M. Yeung, , A. Huebl, , D. Hollatz, and G. Wittig: *Postpic: the open-source particle in cell postprocessor.*, 2017
URL http://dx.doi.org/10.5281/zenodo.18270

[119] S. Kuschel: *Generation of dense electron bunches by laser plasma accelerators for QED experiments in high fields*, Dissertation, FSU, Jena 2018

List of Symbols

Fundamental Constants

Symbol	Name	SI value
c	Speed of light	$299792458\,\mathrm{m/s}$
m_e	Electron rest mass	$9.109 \times 10^{-31}\,\mathrm{kg}$
μ_0	Vacuum permeability	$4\pi \times 10^{-7}\,\mathrm{V{\cdot}s/(A{\cdot}m)}$
ϵ_0	Vacuum permittivity	$8.854{\times}10^{-12}\,\mathrm{A{\cdot}s/(V{\cdot}m)}$
$\hbar$	Reduced Planck constant	$1.055 \times 10^{-34}\,\mathrm{J{\cdot}s}$
e	Elementary charge	$1.602{\times}10^{-19}\,\mathrm{C}$
k_B	Boltzmann constant	$1.381\ {\times}10^{-5}\,\mathrm{J/K}$

Equipment Parameters

Symbol	Name
d_{out}	Nozzle aperture
p_N	Nozzle backing pressure
M	Mach number
$f\#$	f-number
f	Focal length
ψ_R, ψ_T	Polarizer angle
β_R, β_T	Extinction coefficients

General Symbols

Symbol	Name
$\vec{\mathcal{E}}$	Electric field vector
$\vec{\mathcal{B}}$	Magnetic field vector
$\vec{\mathcal{A}}$	Vector potential
ϕ	Scalar potential
$\vec{j}$	Current density
ρ	Charge density
q	Charge
t	Time
x, y, z	Spatial coordinates
ξ	Longitudinal coordinate in co-moving frame of reference
$\vec{e}_x$, $\vec{e}_y$, $\vec{e}_z$	Unit vectors in $x-$, $y-$, and $z-$direction
$\vec{r}$	Radial vector
Φ	Phase
P	Power
m	Mass
T	Temperature
ω	Angular frequency
λ	Wavelength
γ	Relativistic γ-factor
β	Normalised velocity
v	Velocity
$\vec{p}$	Momentum vector

Plasma parameters

Symbol	Name
n	Particle density
n_e	Electron density
η	Index of refraction of plasma
ω_p	Plasma frequency
λ_p	Plasma wavelength
R, R_{bo}	Radius
d	Diameter

Laser Parameters

Symbol	Name
A_L	Focal spot size
E_L	Laser energy
q_L	q-factor
I_V	Vacuum peak intensity
a_0	Normalised vector potential
w	1/e beam radius in focus
r_L	FWHM beam radius in focus
λ_0	Central frequency of laser pulse
λ_L	Strongest line of laser spectrum
τ	Pulse duration
$\vec{k}$	Wavevector
$v_{g,L}$	Laser group velocity
$v_{\Phi,L}$	Laser phase velocity
$\vec{F}_{pond}$	Ponderomotive force

Special Symbols: Controlled Injection

Symbol	Name
α	Angle of shockfront
x_{KE}	Position of knife edge
x_{SF}	Position of density transition
x_{WBR}	Position of emission of wavebreaking radiation
x_{inj}	Position of injection
x_{opt}	Optimum position of injection
l_{acc}	Acceleration length
l_{opt}	Optimum acceleration length
E	Maximum electron energy gain of specific shot
E_{opt}	Maximum achievable electron energy gain for given experimental setting
w_{SF}	Width of density transition
n_{SF}	Electron density of shockfront
n_0	Undisturbed electron density behind shockfront
n_{SF}/n_0	Electron density ratio of transition
q_N	Normalised charge
D	Solid angle of divergence

Special Symbols: Polarimetry Measurements

Symbol	Name
ψ	Angle of rotation
$\mathrm{d}\psi$	Incremental angle of rotation
δ	Phase shift
$\mathrm{d}\delta$	Incremental phase shift
$\vartheta_{\psi,\delta}$	Rotation of polarisation ellipse
χ	Ellipticity

Danksagung

Für das Gelingen dieser Doktorarbeit möchte ich mich bei allen beteiligten Kollegen des Instituts für Optik und Quantenelektronik und des Helmholtz-Instituts Jena bedanken.

- An erster Stelle möchte ich Prof. Malte C. Kaluza danken, der mir die Ausführung der zugrundeliegenden Experimente anvertraut und mich während der gesamten Zeit kontinuierlich unterstützt hat. Ganz besonders danke ich für die zahlreichen aufmunternden Worte und Anekdoten aus seiner eigenen Promotionsphase.

- Prof. Matt Zepf danke ich für viele Diskussionen (unter anderem) zum Thema, für das Lesen der Arbeit und für den Finger ganz tief in der Wunde, der dafür gesorgt hat, dass ich den einen oder anderen Punkt dann doch noch einmal überarbeitet habe.

- Den Elektronies danke ich für die Unterstützung und die Zeit im Labor. Dazu gehör(t)en vor allem Maria Leier, Michael Schnell, Matthew Schwab und Alexander Sävert.

- Evangelos Siminos, dessen Zeit ich immer und immer wieder beansprucht habe, danke ich für die Unterstützung mit seinen PIC-Simulationen und den simulierten Polarogrammen. Stephan Kuschel danke ich für das input.deck und seine Unterstützung mit PostPic.

- Für das Lesen der Arbeit im Ganzen oder in Teilen möchte ich Matthew Schwab, Alexander Sävert, Evangleos Siminos und Carola Wirth danken.

- Falk Ronneberger, Burgard Beleites und Wolfgang Ziegler danke ich für Laser- und Experimentsachen, die ohne deren Erfahrung einfach nicht möglich gewesen wären. In diesem Rahmen möchte ich mich auch bei den Mitarbeitern der Werkstätten bedanken, die im Notfall immer ein gaaaanz wichtiges Anliegen einschieben konnten.

- Auch wenn das Elektronenexperiment am POLARIS in dieser Arbeit keinen Platz mehr gefunden hat, möchte ich mich bei dem POLARIS-Team für die viele Zeit bedanken, die mir für das Experiment zur Verfügung gestellt wurde.

- Der gesamten Arbeitsgruppe "Relativistische Laserphysik" danke ich für Kuchen, Gruppenausflüge und Grillen im Garten.

- Ajay Arunachalam, Martin Kahle, Cornelia Kabis, Felix Karbstein und Carola Wirth danke ich für ihr offenes Ohr. Claudi, Kalki, Laura und Kerstin danke ich für viel Spaß und Mädelszeit. Maumi B. Tingu für ihre grenzenlose Weißheit.

- Zu guter Letzt möchte ich mich bei meiner Familie bedanken, weil sie immer für mich da sind.

A. Experimental Setup and Data Analysis

A.1 JETI-Laser System

At a central wavelength of $\lambda_L \approx 800\,$***nm, the*** JETI***-laser system delivers pulses with an energy of*** $E_L \approx 850\,$***mJ, an FWHM pulse duration of*** $\tau_L \approx 30\,$***fs and a*** $1/e^2$ ***beam diameter of*** $d_e \approx 50\,$***mm.***

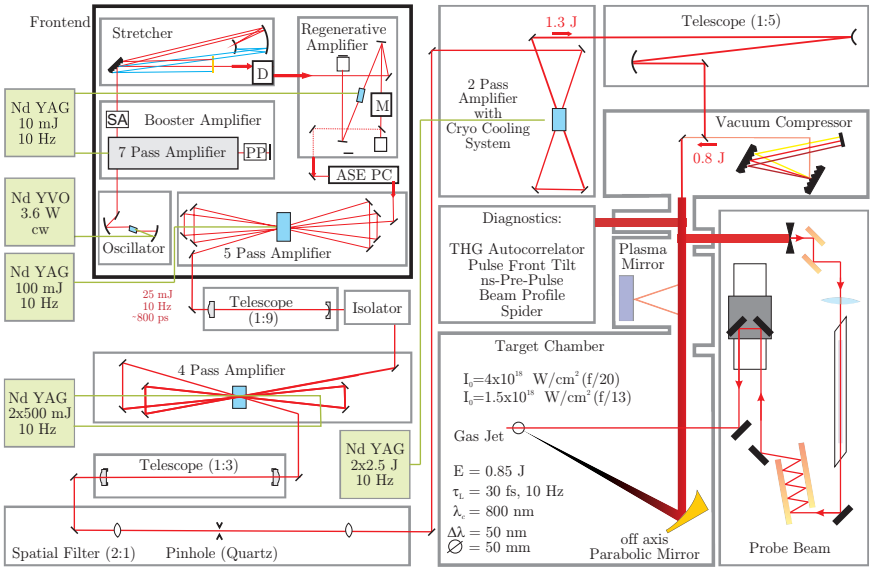

Figure A.1 *Schematic of the* JETI*-laser system.*

Figure A.1 shows the JETI-laser system which is based on titanium doped sapphire as the active medium which – except for the crystal in the oscillator at the beginning of the laser chain – is pumped by frequency doubled Nd:YAG-lasers. The frontend of the laser consists of the oscillator (pumped by a continuous wave Nd:YVO laser), the pulse stretcher and the first amplifiers. It delivers pulses with an energy of 25 mJ at a pulse repetition rate of 10 Hz. After the two final multipass amplifiers and the vacuum pulse compressor, the laser pulses contain an energy of $E_L \approx 850\,$mJ and have an FWHM duration of $\tau_L \approx 30\,$fs. While the central wavelength is $\lambda_L \approx 800\,$nm, the most intensive spectral component can vary (cf. appendix A.1.1). The amplified and compressed pulses are guided towards the target chamber inside an evacuated beamline where the probe beam is separated from the main beam by a beam splitter. At the entrance of the target interaction chamber, the main pulses have an $1/e^2$ beam diameter of $d_e \approx 50\,$mm. Ideally, a laser pulse has a smooth envelope, e.g. with a Gaussian shape as shown in section 2.1. Nevertheless, pre- and post pulses as well as amplified spontaneous emission (ASE) generated in the amplification process modify the temporal envelope of the laser pulse and hence, the temporal intensity contrast of the laser pulse. At the JETI-laser system, the intensity contrast of the laser pulses can be

improved by means of a plasma mirror which has an intensity dependent reflectivity. Therefore, ASE and pre-pulses of sufficiently low intensity can be removed, which reduces the laser pulse's energy.

A.1.1 Strongest Component of the JETI-Spectrum

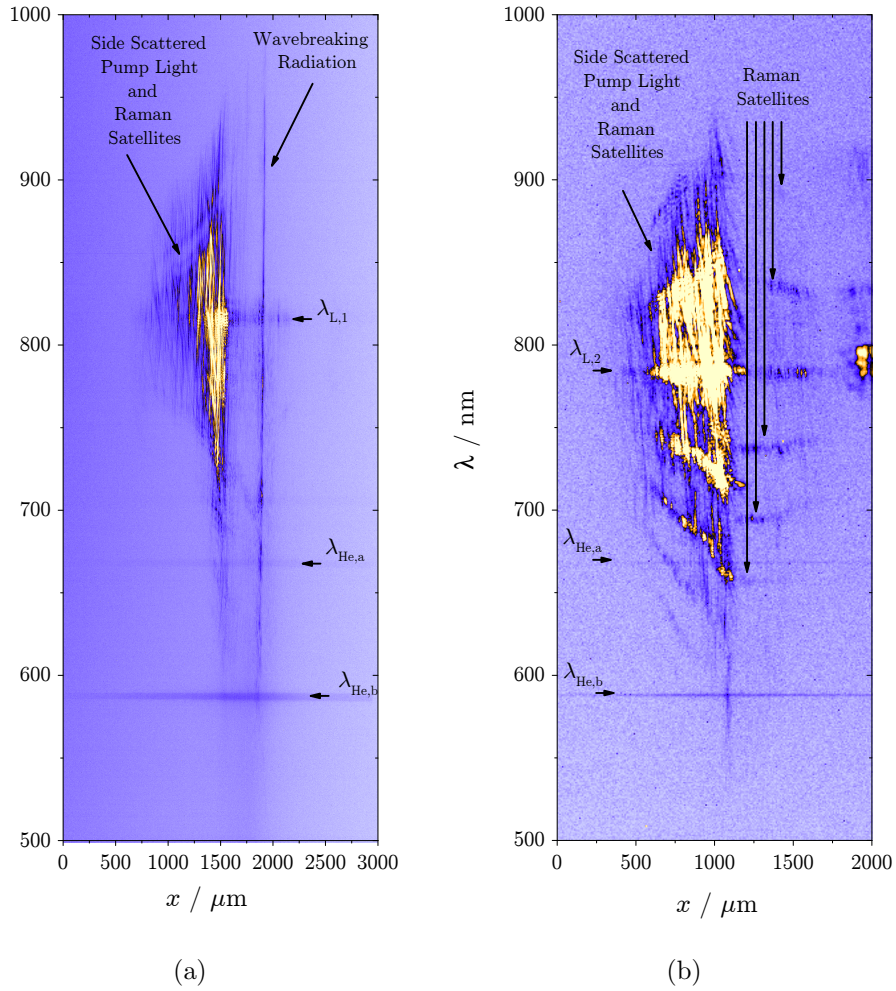

(a) (b)

Figure A.2 *Spatially resolved optical spectra from both campaigns. (a) f/20, (b) f/13.*

The spectral calibration of the imaging spectrometer was performed using a mercury-vapour lamp and a shot to shot verification was possible through some specific lines of helium, here $\lambda_{He,a} = 667.8\,\text{nm}$ and $\lambda_{He,b} = 587.5\,\text{nm}$ [68]. Since the calibration in the above images is comparable, it becomes evident that the strongest component of the JETI-spectrum is different in the two experimental campaigns presented in this thesis. While during Campaign 1, $\lambda_{L,1} \approx 818\,\text{nm}$, in Campaign 2, it was at a lower wavelength $\lambda_{L,2} \approx 783\,\text{nm}$, which is most likely caused by the settings of the Mazzler [116] – an acousto-optic programmable gain filter which controls the spectral gain [117]. A Mazzler optimisation in between the campaigns is documented in the laser protocol.

B. Controlled Injection of Electrons into Plasma Waves

B.1 Spatially Resolved Optical Spectra

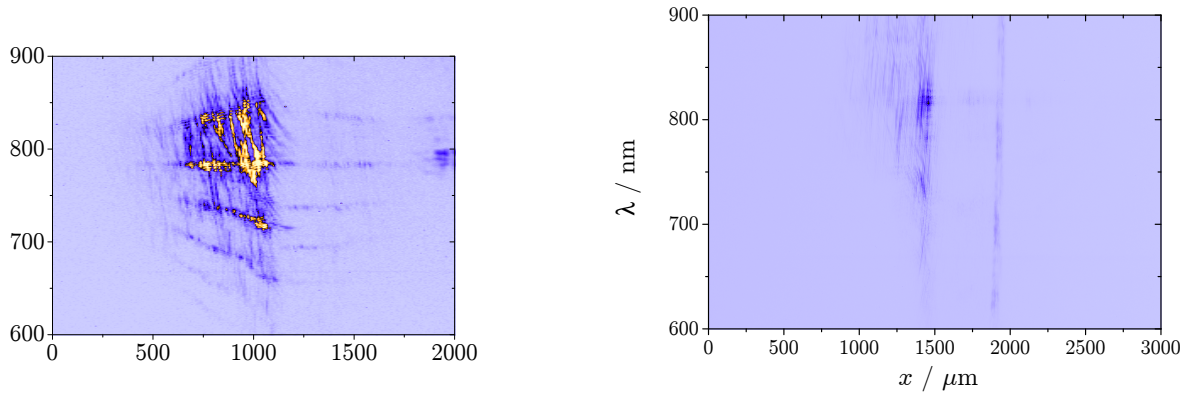

(a) (b)

Figure B.1 *Raw data in false colour.*

B.2 Particle-In-Cell (PIC) Simulations

Three-dimensional PIC simulations were performed to investigate the individual influence of single parameters on the injection and acceleration process. All simulations are comparable to the default simulation with $a_0 = 2$, $\alpha = 22.5°$, $w_{SF} = 5\,\mu$***m and*** $n_{SF}/n_0 = 2$. $n_0 = 7.7\times10^{18}$ ***cm***$^{-}3$ ***is kept constant in all runs.***

For the experiments presented in chapter 4, three-dimensional PIC simulations where performed with Epoch [96] at the Max Planck supercomputer at the Garching Computing Center RZG and post processed using Postpic [118]. Note that the input file for the simulations was provided by Stephan Kuschel from Helmholtz Institute Jena while the author of this thesis carried out the parameter scans.

Each cell of the 3D simulation box contains one macro particle and has a size of $\approx 0.06\,\mu$m in propagation direction $\vec{e}_x$ and $\approx 0.13\,\mu$m in transverse directions $\vec{e}_y$ and $\vec{e}_z$. The computing time was kept low by reducing the propagation time to 850 fs corresponding to a propagation distance of $\approx 280\,\mu$m. Therefore, it is not possible to scan the influence of different shockfront positions x_{SF}. Nevertheless, the influence of individual parameters can be investigated in separate parameter scans. Table B.1 shows the scanned parameters, their range and their default settings. The range

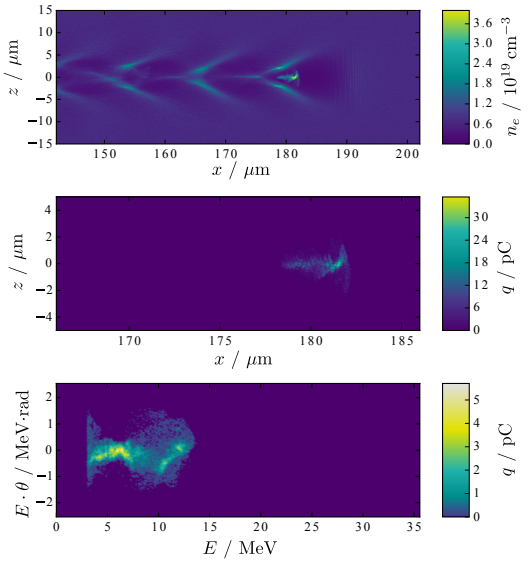

Figure B.2 *Top: Electron density map. Middle: Filtered electron density map for the generation of the electron spectrum at the bottom.*

of the electron density ratio, the angle as well as the width of the shockfront are adopted from section 4.2. Furthermore, the influence of different laser intensities –caused by laser pulse evolution in the real experiment– is investigated by varying the vacuum peak intensity a_0 in the simulation. During the scan of a distinct parameter, other parameters were set to their default values.

Parameter	Values	Default
a_0	1, 2, 3, 4	2
n_{SF}/n_0	1, 1.25, 2, 2.6	2
α / °	0, 10, 22.5, 50	22.5
w_{SF} / μm	1, 5, 10, 16	5

Table B.1 *Parameters of the simulated scans. In all simulations,* $n_0 = 7 \times 10^{18} cm^{-3}$.

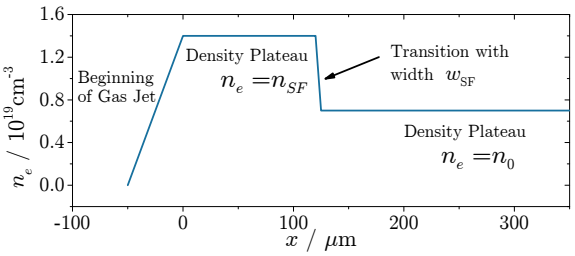

Figure B.3 *Electron density configuration in the simulations exemplarily shown for the default parameters (cf. Table B.1).*

The density profile was configured as exemplarily shown in Fig. B.3 for the default parameters at the laser axis $y = z = 0$. For $y \neq 0$ or $z \neq 0$, the x-positions of the density transition depend on the the angle of the shockfront α. The constant density in front of the density transition was chosen to keep the interaction as simple as possible and to isolate the influence of different parameters from each other.

The top image in Fig. B.2 shows a distribution of the electron density from the default simulation at a simulation time of $\approx 850\,$fs. For the extraction of the electron spectrum in the bottom image, the plasma wave electrons and electrons inside trailing buckets are eliminated from the density map through following restrictions:

- $\gamma > 6$,
- $x > 172\,\mu$m,

- $\frac{p_x}{p_{yx}} < 0.5\,\mathrm{rad}$,

with p_x and p_{yz} being the forward and the transverse momenta of the accelerated electrons, respectively. The filtered electron density map is depicted in the middle image of Fig. B.2. Note the different dimensions in x and z compared to the top image.

B.3 Influence on the Transverse Electron Beam Profile

With the electron beam monitor (cf. section 3.3), the electron beam's charge, divergence as well as pointing were investigated in dependence on the position of the knife edge or shockfront, respectively. Therefore, a gas nozzle with a diameter of $d_N = 3.1\,\mathrm{mm}$ was operated at different nozzle backing pressures corresponding to electron densities ranging from $n_0 \approx 9.2$ to $12.1 \times 10^{18}\,\mathrm{cm}^{-3}$. In the following, the results for $n_0 = 9.2 \times 10^{18}\,\mathrm{cm}^{-3}$ are discussed exemplarily.

Fig. B.4 shows beam monitor images averaged over 20-30 consecutive shots for different positions x_{SF}. The centroid of the reference profile is marked with dotted white lines in all images. While the averaged images give an impression of the effect of the shockfront on the accelerated charge, pointing and divergence effects are not clearly distinguishable. Thus, the quantitative investigation requires the images to be analysed separately and those results to be averaged.

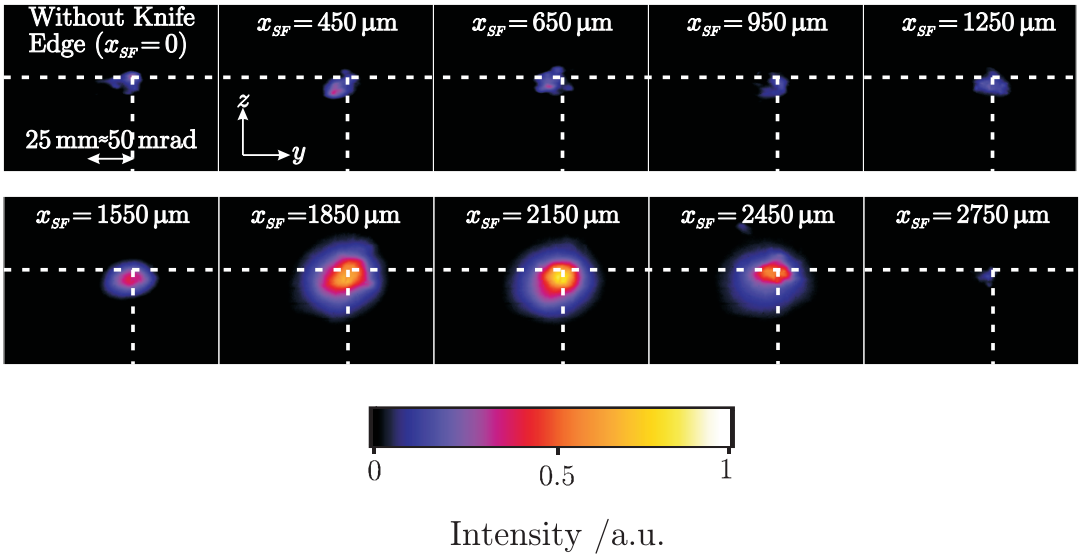

Figure B.4 *Averaged beam monitor images for different positions of the shockfront x_{SF}.*

B.3.1 Accelerated Charge

The increase of the normalised bunch charge q_N with the position of the shockfront is most likely caused by the evolution of a_0 to higher intensities and the increasing density of the shockfront n_0, which can be supported by results obtained from PIC simulations.

For the determination of the normalised bunch charge, the average of the relative charge determined at any position x_{SF} is divided by the average of the relative charge obtained in the reference measurement without shockfront represented by $x_{SF} = 0$. The relative electron beam

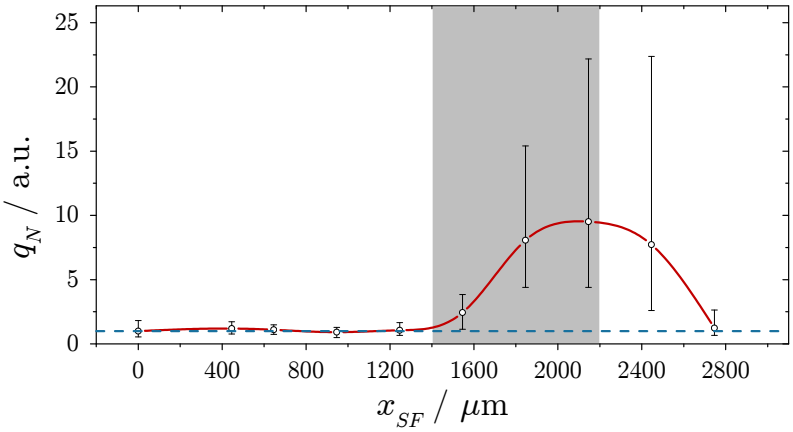

Figure B.5 *Normalised bunch charge q_N incident at the electron beam monitor for varying shockfront positions x_{SF} and a nozzle backing pressure of 8 bar ($n_0 \approx 9.2 \times 10^{18}\ cm^{-3}$). The error bars represent the upper and the lower mean deviation from the averages which are represented by circles.*

charge is given in units of the intensity of the radiation emitted from the electron beam monitor (cf. section 3.3).

The behaviour of the normalised bunch charge q_N in dependence on the position of the shockfront x_{SF} is shown in Fig. B.5 where the grey shaded area marks the range of shockfront positions, which were investigated in section 4.4 where a dependence of the energy spread of the electron spectra was discussed in dependence on the position of the shockfront x_{SF}. The increase of charge in the grey box in Fig. B.5 is consistent with an increasing frequency of occurrence of broadband electron spectra (high charge) while the frequency of occurrence of monoenergetic electron spectra (low charge) decreases.

Dependence of injected charge on the position of the shockfront. Since a portion of the electrons of the plasma wave's electron density peak is injected at the density transition, the number of injected electrons can be increased by increasing the number of electrons contained in the plasma wave's electron density peak. This can be realised by driving the plasma wave more strongly with a more intense laser pulse (increase of a_0) and by increasing the background density in region I, i.e. by increasing n_{SF}. The constant charge below $x_{SF} \approx 1200\,\mu$m is most likely self injected – possibly behind the shockfront – since at those positions x_{SF}, the plasma wave has most likely not sufficiently evolved to inject a significant number of electrons. In contrast, the increase of the charge above $x_{SF} \approx 1200\,\mu$m suggests a continuously harder driven plasma wave. While an increase of n_{SF} with x_{SF} could be observed (cf. section 4.2.4.3), the constant γ-factor does not indicate an increase of laser intensity with x_{SF}. Nevertheless, most results regarding the accelerated electrons (cf. sections 4.4.1.1,4.4.1.3, 4.4.2.1) indicate that the laser pulse evolves to higher intensities. Laser pulse evolution in the plasma is investigated in more detail in chapter 5.

The PIC-simulated parameter scan introduced in Appendix B.2 confirms that the accelerated charge can be increased by a_0 and n_{SF}. The increase of the bunch charge with a_0 and n_{SF}/n_0 where $n_0 = 7.7 \times 10^{18}\,\mathrm{cm}^{-3}$ is shown in Figs. B.6(a) and B.6(b), respectively. In contrast, the angle

and width of the shockfront seem to play a minor role for the accelerated charge (cf. Figs. B.6(c) and B.6(d)).

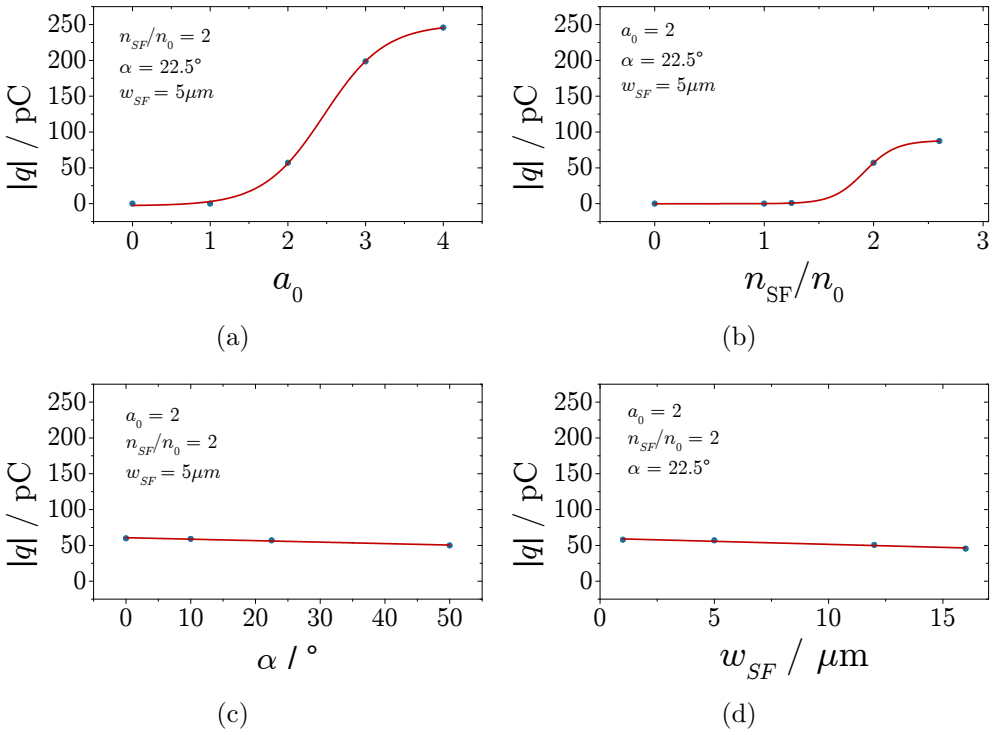

Figure B.6 *Accelerated charge in the simulations in dependence on (a) the normalised vector potential a_0 (b) the density ratio n_{SF}/n_0 with $n_0 = 7.7 \times 10^{18}\ cm^-3$ (c) the angle of the shockfront α and the width of the shockfront w_{SF}.*

The decrease of charge after $x_{SF} \approx 2150\,\mu$m might be due to weaker and weaker driven plasma waves possibly as a consequence of the onset of pump depletion. Note that the exclusion of pump depletion as a reason for the energy dependence in section 4.4.1.2 is not in conflict with this assumption as those measurements were carried out with a smaller nozzle with $d_{out} = 2.1\,$mm while the results presented here were obtained with a nozzle with $d_{out} = 3.1\,$mm.

In an experiment performed with comparable laser parameters [49], the injection of electrons at a wire produced double shockfront was investigated. In this experiment, injection and acceleration of the measured electrons was assumed to take place in a region of the gas jet with an electron density distribution comparable to the shockfront profile presented in Fig. 4.12(c). A similar dependence of the accelerated charge on the position of injection was observed but not further discussed.

B.3.2 Divergence

The increase of divergence with x_{SF} can be explained by a more frequent generation of electron spectra with a low energy tail (reduction of longitudinal momentum) as well as the frequently observed energy dependent pointing variations of the electron beam in the broadband electron spectra, which could be traced back to Betatron oscillations (increase of transverse momentum).

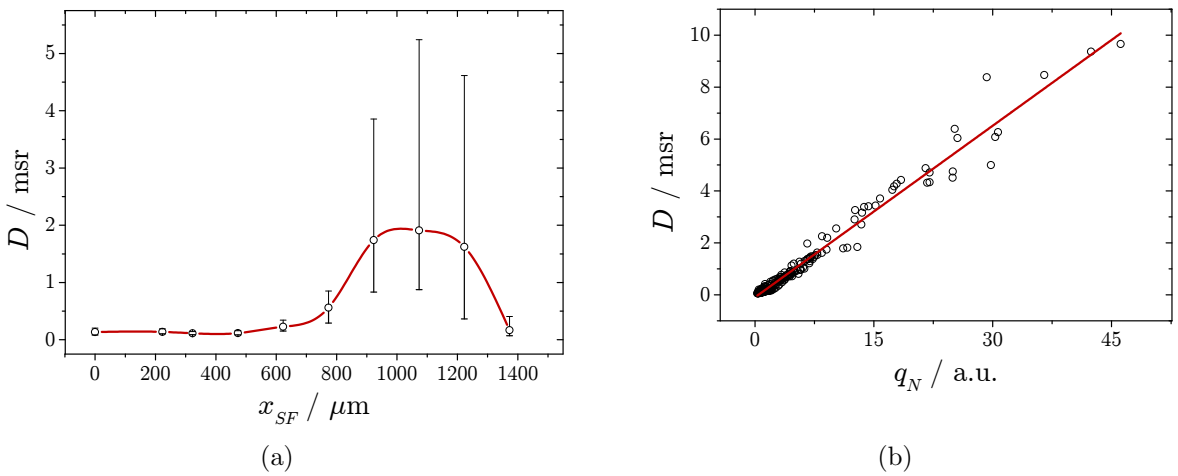

Figure B.7 *(a) Bunch divergence D in dependence on the shock front position x_{SF} and (b) relation of divergence and charge.*

Fig. B.7(a) shows the trend of the averaged FWHM solid angle of divergence D of the electron beam (Fig. B.7(a)), which is comparable to the trend of the average of the accelerated charge (Fig. B.5). Moreover, Fig. B.7(b) reveals a linear relation of divergence and charge, which could be caused by Coulomb repulsion and thus, might be an indicator for beamloading. Nevertheless, beamloading is not indicated by the results discussed in section 4.4.2.1, which were obtained in Campaign 2. The measurements presented in this section are obtained using an off-axis parabolic mirror with larger $f_{\#}$-number in Campaign 1. Due to the lower laser intensity, the injected and thus, accelerated charge can be assumed to be smaller, i.e., beamloading is less likely here.

The divergence of the electron beam is given by the ratio of transverse and longitudinal momentum $p_{y,z}/p_x$ of the electrons. Both, the increase of $p_{y,z}$ combined with a decrease of p_x is given by the low energy tail of the oscillating broadband electron spectra exhibiting an increased charge and generated more frequently with increasing shockfront position (cf. section 4.4.2.1). Hence, the increase of divergence is most likely caused by Betatron oscillations, which were discussed in section 4.4.2.2.

B.3.3 Pointing

While pointing fluctuations are most likely caused by electron density inhomogeneities, the change of pointing might be the result of diffraction of the laser pulse at the shockfront.

Fig. B.8(a) shows the horizontal Δy_p (blue) and (b) vertical Δz_p (red) change of pointing in comparison to the reference measurement without shockfront represented by $x_{SF} = 0$. On average, the fluctuation of pointing amounts to $\approx 4.5\,\mathrm{mrad}$ and cannot be explained by the fluctuation of pointing of laser pulse and plasma wave of $\approx \pm 30\,\mu\mathrm{rad}$. However, in a similar setup with comparable gas nozzles, pointing fluctuations could be traced back to electron density inhomogeneities in the gas jet profile [119].

While the horizontal variation in pointing is dominated by fluctuations, the vertical pointing shows a dependence on the position of the shockfront x_{SF} with a maximum deviation of

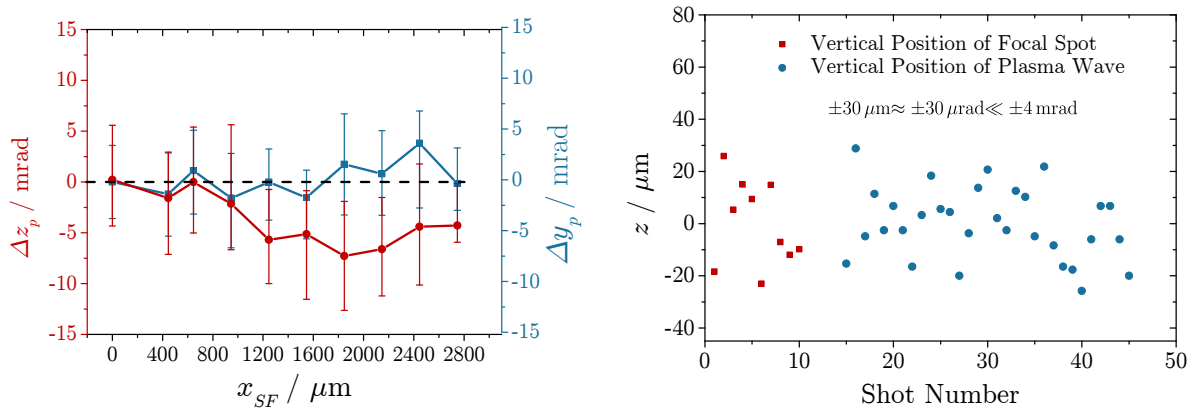

(a) (b)

Figure B.8 *(a) Vertical Δy_p and (red) horizontal Δz_p (blue) centroid of the electron beam with respect to the measurement without knife edge. (b) Pointing fluctuation of laser pulse and plasma wave.*

≈ -7.4 mrad compared to the reference measurement without shockfront (cf. Fig. B.8(a)). A change of vertical pointing of the electron bunch might be induced by refraction of the laser pulse at the density transition which can be described using Snell's law incorporating the changing angle α of the shockfront. Furthermore, the refractive indices η_{SF} and η_0 (Eq. (2.21)) of the plasma before and after the shockfront are assumed to be given by n_{SF} which depends on x_{SF} (cf. section 4.2.4.3) and $n_0 = 9.2 \times 10^{18} cm^{-3}$, respectively (cf. section 4.2.4.2). Fig. B.9 shows the

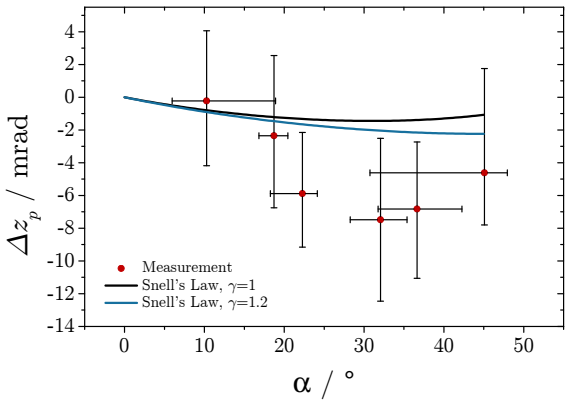

Figure B.9 *Measured and calculated vertical pointing.*

pointing of the electron bunches with respect to the shockfront angle α (red filled circles) and the result of the estimation with Snell's law is shown as a black line where for the calculation of the refractive index $\gamma = 1$ was assumed. In section 4.2.4.1 $\gamma \approx 1.2$ was deduced. The result of Snell's law calculated with $\gamma \approx 1.2$ is shown as a blue line. While the agreement of measurement and calculation is improved, the measured change of pointing is still significantly larger. This is most likely caused by the assumption of a perfect transition from a constant electron density n_{SF} to a constant electron density n_0. Furthermore, the determination of γ might be not sufficiently accurate for various reasons (cf. section 4.2.4.1).

C. Towards the Indirect Observation of the Laser Pulse Evolution in a Plasma

C.1 Jones Calculus

In the Jones formalism, a plane electromagnetic wave propagating in $y-$direction is represented by its electric field component

$$E_{init} = \begin{bmatrix} E_x \\ E_z \end{bmatrix} e^{i(kx-\omega t)}. \tag{C.1}$$

For further calculations, the waves oscillation given by $e^{i(kx-\omega t)}$ is not taken into account and the components of the Jones vector are normalised, i.e., an electromagnetic wave initially polarised in $\vec{e}_x$ can be written as

$$E_{init} = \begin{bmatrix} 1 \\ 0 \end{bmatrix}. \tag{C.2}$$

The rotation matrix

$$ROT = \begin{bmatrix} \cos(\psi) & -\sin(\psi) \\ \sin(\psi) & \cos(\psi) \end{bmatrix}, \tag{C.3}$$

rotates the wave's plane of polarisation by the angle ψ as and the rotated field reads

$$E_{rot} = \begin{bmatrix} \cos(\psi) \\ \sin(\psi) \end{bmatrix}. \tag{C.4}$$

Subsequently applying the retardation element

$$RET = \begin{bmatrix} e^{i\delta} & 0 \\ 0 & 1 \end{bmatrix}, \tag{C.5}$$

which shifts x-component in phase by δ results in

$$E_{rot,ret} = \begin{bmatrix} \cos(\psi)e^{i\delta} \\ \sin(\psi) \end{bmatrix}. \tag{C.6}$$

A polariser rotated by the angle α with respect to horizontal polarisation is given by

$$POL_\alpha = \begin{bmatrix} \cos^2(\alpha) & \cos(\alpha)\sin(\alpha) \\ \cos(\alpha)\sin(\alpha)) & \sin^2(\alpha) \end{bmatrix}. \tag{C.7}$$

The transmitted portion of the electric field $E_{rot,ret}$ after the polariser is

$$E_{rot,ret,pol} = \begin{bmatrix} e^{i\delta}\cos^2(\alpha)\cos(\psi) + \cos(\alpha)\sin(\alpha)\sin(\psi) \\ e^{i\delta}\cos(\alpha)\sin(\alpha)\cos(\psi) + \sin^2(\alpha)\sin(\psi) \end{bmatrix} = \begin{bmatrix} \mathcal{E}_x \\ \mathcal{E}_z \end{bmatrix} \tag{C.8}$$

and can be used to calculate the transmitted intensity $I \propto |\mathcal{E}_x^2| + |\mathcal{E}_z^2|$. In the general case $I_{rot,ret,pol} = |e^{i\delta}\cos(\alpha)\cos(\psi) + \sin(\alpha)\sin(\psi)|^2$, the transmitted intensity depends on the phase shift δ, the polariser angle α and the rotation of the plane of polarisation ψ. If $\delta = 0$, the expression simplifies to $I_{rot,pol} = \cos^2(\alpha - \psi)$.

C.2 Determination of the Extinction Ratio

An extinction ratio can be determined experimentally by measuring the transmission curve of the polarisers with respect to the polariser angle which is shown for both polarisers in Figure C.1. To remove shot to shot fluctuations of the probe beam's brightness, each image taken by CCD-T at varying polariser angles was normalised to the intensity recorded by CCD-R at a fixed setting and vice versa. Using Malus' law

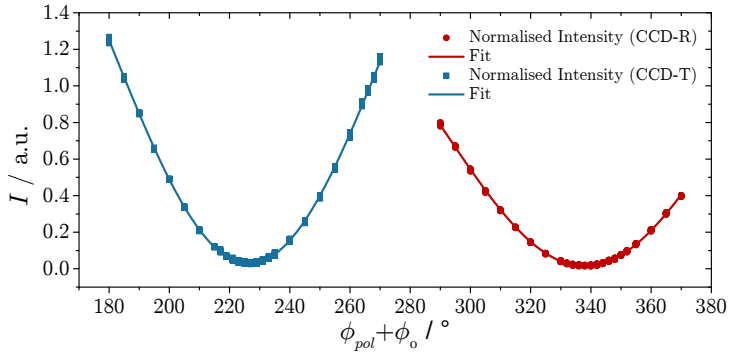

Figure C.1 *Normalised intensity on CCD-T and CCD-R with respect to the corresponding polariser angles. With the normalised intensity with respect to the angle of polarisation incident on the two CCD cameras, the extinction coefficients of the imaging systems can be determined.*

$$I = I_0\Big(1 - \beta\sin^2(90° - (\psi_{pol} - \psi_0))\Big), \tag{C.9}$$

the angles of maximum extinction $\phi_{0,T}$ and $\phi_{0,R}$ as well as the extinction coefficients were determined with a fit.

Ehrenwörtliche Erklärung

Ich erkläre hiermit ehrenwörtlich, dass ich die vorliegende Arbeit selbstständig und ohne unzulässige Hilfe Dritter und ohne Benutzung anderer als der angegebenen Hilfsmittel und Literatur angefertigt habe. Die aus anderen Quellen direkt oder indirekt übernommenen Daten und Konzepte sind unter Angabe der Quelle gekennzeichnet.

Die PIC-Simulationen im Rahmen der Hochauflösungspolarimetriemessungen wurden von Evangelos Siminos von der University of Gothenborg durchgeführt und in weiten Teilen ausgewertet. Weitere Personen waren an der inhaltlichen-materiellen Erstellung der vorliegenden Arbeit nicht beteiligt. Insbesondere habe ich hierfür nicht die entgeltliche Hilfe von Vermittlungs- bzw. Beratungsdiensten (Promotionsberater oder andere Personen) in Anspruch genommen. Niemand hat von mir unmittelbar oder mittelbar geldwerte Leistungen für die Arbeiten erhalten, die im Zusammenhang mit dem Inhalt der vorgelegten Dissertation stehen.

Die Arbeit wurde bisher weder im In- noch im Ausland in gleicher oder ähnlicher Form einer anderen Prüfungsbehörde vorgelegt.

Die geltende Promotionsordnung der Physikalisch- Astronomischen Fakultät ist mir bekannt.

Ich versichere ehrenwörtlich, dass ich nach bestem Wissen die reine Wahrheit gesagt und nichts verschwiegen habe.

Ort, Datum Unterschrift